Chair of Applied Geophysics

Master's Thesis

Applicability of Geophysical methods for the prospection of Paleo-laterite deposits

Tereze Reke

October 2023

MONTANUNIVERSITÄT LEOBEN
www.unileoben.ac.at

AFFIDAVIT

I declare on oath that I wrote this thesis independently, did not use other than the specified sources and aids, and did not otherwise use any unauthorized aids.

I declare that I have read, understood, and complied with the guidelines of the senate of the Montanuniversität Leoben for "Good Scientific Practice".

Furthermore, I declare that the electronic and printed version of the submitted thesis are identical, both, formally and with regard to content.

Date 31.10.2023

Signature Author
Tereze Reke

Abstract

Already in the 19th and 20th centuries, laterite ore was mined at the Kraubath massif – an ophiolitic complex in the Easter Alps, Austria. There the laterite ore bodies are incorporated between layers of Neogene clastic sediments. However, due to the costly transporting and the unsatisfactory quality of the ore, the excavation of the laterite ore deposits was ceased. Now once again it is being investigated for its possible economic utilization. The spatial distribution and dimensions of laterite ore can be resolved with the use of different geophysical methods. However, the applicability of geophysical methods in the lateritic environment has been tested in only a few published cases and with few geophysical methods. In this thesis, the laterite ore bodies were studied by applying four geophysical methods – electrical resistivity tomography, magnetics, self-potential, and electromagnetics – for the evaluation of each of the methods feasibility for delineating discrete anomalies related to the laterite ore. The data for the analysis was acquired during the master's course "Geophysical and Geochemical Field Project", organized from 2016 to 2021. Subsequently, it was processed for further interpretation and representation. The gained end results were achieved by an individually adjusted flow for each applied geophysical method and location. The obtained results assess the suitability of each applied geophysical method. ERT results displayed low resistivity zones which were interpreted as laterite based on direct data from the field and borehole. Few uncertain low resistivity zones, where clear indications of laterite existence were not found, were supplemented by magnetic data which helped to determine laterite ore body location. Magnetic data 3-D models, constrained by susceptibility values measured in the field, were constructed for the investigation areas, covering areas where ERT methods profiles did not reach. Self-potential and electromagnetic methods contributed more like additional methods for conforming ERT and magnetics results by providing approximate locations of the ore bodies.

Keywords: Laterite deposits, electrical resistivity tomography, magnetism, electromagnetic method, self-potential, RES2DINV, Potent v4.17.01, geophysics

Acknowledgements

First and foremost I would like to express my most profound appreciation to my research supervisors, Assoc. Prof. Robert Scholger and Assoc. Prof. Eusebio Stucchi. To Assoc. Prof. Robert Scholger for his guidance and support throughout my research. I appreciated his help in developing the ideas presented in my thesis and for providing me with the geophysical data collected during various field campaigns. To Assoc. Prof. Eusebio Stucchi for his insight and useful comments regarding the thesis. For challenging and making a discussion regarding some unclear stated facts or results in the process improving end result.

Furthermore, I would like to thank to Christiane Pretzenbacher for her assistance with various organizational matters during my studies.

The author wishes to express her gratitude to close friends Jana Budniece, Jolanta Kucinskate, Kristina Kucinskaite and Estere Ponciusa for their emotional support and for giving me academic opinions as well.

Last but not least my appreciation goes to my family for their constant help during my studies years and for encouraging me to pursue a master's degree.

Contents

List of Figures

List of Tables

List of Abbreviations

ERT	**E**lectrical **R**esistivity **T**omography
IP	**I**nduced **P**olarization
EM	**E**lectromagnetic
SP	**S**elf **P**otential
TMI	**T**otal **M**agnetic **I**ntensity
IGRF	**I**nternational **G**eomagnetic **R**eference **F**ield
KUM	**K**raubath **U**ltramafic **M**assif
2-D	**Two D**imensional
3-D	**Three D**imensional

List of Symbols

σ	conductivity
ρ	resistivity
ρ_a	apparent resistivity
R	resistance
G	geometric factor
B	magnetic field induction
H	magnetic field intensity
W	magnetic potential
M	magnetic moment
B_r	magnetic field in the direction of r
B_θ	magnetic field normal to r at the point of observation P
μ_0	permeability of free space
E	electric field
J	electric current density
D	electric flux density
g	forward operator
d	data
M	model parameters
J	Jacobian matrix
J^T	Jacobian matrix and its transpose
f	discrepancy vector
I	identity matrix
λ	damping factor
Δ_q	model parameter change vector
δm	perturbation vector
dU	data measurement error
Δd	data misfit vector

1 INTRODUCTION

1.1 General overview

The laterite that forms under tropical weathering conditions has been investigated as ore deposits for various chemical elements like Al, Fe, Ni, Au, Nb, and P in different locations, all around the world (Sowards et al., 2018). Laterite ore, incorporated between layers of Neogene clastic sediments, from the Kraubath massif, an ophiolitic complex in the Eastern Alps in Steiermark, Austria, has been mined before and is again studied for possible economic utilization. All mining rights belong to MINEX Mineral Explorations GmbH.

The laterite has only a few known outcrops in the study area and is intersected once by a borehole. Nor have any large-scale mineral exploration works been done up until now. Numerous geophysical data were obtained in the frame of our master´s courses "Geophysical and Geochemical Field Project" from 2016 to 2021 for a better understanding of laterite ore bodies' geometry and distribution and furthermore to the understanding of the different geophysical properties of the surrounding bedrock. The thesis author took part in the field works organized in the year 2020.

Based on the geological information from a few available research materials, borehole data, and field observations, the area was considered to have favorable geological conditions and sufficient direct data to apply any of the four used geophysical methods. Along with enough data to link obtained physical properties to constrain inverse problem end results allowing to study numerous kinds of physical responses above the same geological structure. Good contrasts between existing lithologies laid a good foundation for potentially successful results.

In the lateritic environment – as attested by the previously conducted case studies – electrical resistivity tomography and magnetic methods have been used effectively and with great success. Both applied methods were able to capture the laterite ore's body's location, distribution and dimensions. The applicability of the electromagnetic and self-potential methods to this type - such an environment has not been published in the available online publications, book examples, nor conference papers. However, the absence of this information in science literature does not rule out the capability of efficiency of both methods in a given geological environment.

1.2 Research objectives and methodology overview

The aim of this study is to compare various geophysical methods for laterite and surrounding bedrock exploration by the use of datasets from different geophysical methods – magnetics, self-potential, electromagnetics, and electrical resistivity tomography. Each method has its own advantages and disadvantages. Hence, the combining of datasets of all applied methods into one integrated interpretation, could considerably increase the reliability of the end results and furthermore could reduce the "non- uniqueness" problem of geophysics.

The following objectives have been set in order to fulfil this aim:

- Evaluate each method's feasibility of delineating ore bodies or adjacent lithologies;
- Find an optimal framework and systematic methodology for each method that can be applied for the laterite bodies exploration and for the adjacent lithologies border delineation;
- Determine the average volume and dimensions of ore bodies and distribution with respect to bedrock;
- Govern adjacent lithologies physical parameters and possibility of border delineation.

To accomplish set objectives, raw data, obtained from various field campaigns in a frame of the master's course, was processed, sorted and corrected to acquire a set of data for further interpretation and representation. The end results were achieved by an individually adjusted flow for each applied geophysical method and location. All findings were then reviewed, and the ability of each method to detect laterite bodies or lithological borders was assessed.

1.3 Organization of the thesis

The thesis is organized into ten chapters with two appendices attached. Within Chapter 1 the main objective of the thesis is introduced along with a general overview of the methodology. In Chapter 2, a basic theory and principles of applied geophysical methods are explained. Chapter 3 covers inverse and forward problem solution algorithms with respect to the RES2DINV and Potent v4.17.01 software. Within Chapter 4, laterite prospection case studies around the world are discussed. Chapter 5 consists of a review of the study sites' geology and historic mining. In Chapter 6 steps of the applied methodology: geophysical data acquisition, data processing and modeling are thoroughly elaborated. Within Chapter 7 data quality assessment for the ERT data is given. Within Chapter 8 obtained results and interpretation are presented. Discussion in Chapter 9 starts with highlighting the advantages and drawbacks of the obtained results by each geophysical method, followed by the key remarks on the data acquisition and efficient representation. Chapter 10 concludes the completed work, key results, and resulting recommendations. Following

the conclusion, Appendices A and B contain the observed and calculated apparent resistivity pseudosections and observed magnetic field (XYZ) plot provided by Conrad observatory, respectively.

2 A BRIEF OVERVIEW OF APPLIED GEOPHYSICAL METHODS

As part of the master thesis, in total four geophysical methods were applied – electrical resistivity tomography, magnetism, electromagnetic method and self–potential. In this chapter, each geophysical method's fundamental principles, theoretical background and governing equations were discussed.

2.1 Electrical resistivity tomography

The electrical resistivity method is non-invasive, economical, user-friendly, fast and provides a lateral and vertical mapping of the subsurface for large coverage areas (Shao et al., 2021). Geophysicists have long been employing the ERT method for various purposes such as mineral exploration, the search for geothermal reservoirs and groundwater hydrology research. With the ERT method, we look for the electrical conductivity of the earth using measurements of the potentials which are established by an input direct current (Yuval and Oldenburg, 1996). The outcome depends on electrode configuration and the actual subsurface distribution of the electrical properties with respect to the electrode locations (Dentith and Mudge, 2014).

For a point source of current at the surface of a homogeneous medium injecting a current into the ground, the flow of electric current will be radially symmetric in the half-space. As the result, a current density J will be created within the half-space which can be related to both the electric field E and the material conductivity σ through Ohm's law:

$$J = \sigma E \tag{2.1}$$

The potential is measured over homogeneous isotropic earth at a point located a distance X from the current electrode and with respect to zero potential located at infinity (Dentith and Mudge, 2014). The potential at any point at a distance X from the electrode can be found:

$$V = \frac{I\rho}{2\pi X} = \frac{I\rho}{2\pi}\left(\frac{I}{X}\right) \tag{2.2}$$

When describing electrode arrays, the convention has it that the current electrodes are labelled as 'A' and 'B' and the potential electrodes as 'M' and 'N'. The distance between the current and potential electrodes is defined as X_{AB} and X_{MN}. By applying Eq. (2.2) for each electrode the resultant potential difference (ΔV) between the potential electrodes can be obtained:

$$\Delta V = \frac{I\rho}{2\pi}\left(\frac{1}{X_{AM}} - \frac{1}{X_{BM}} - \frac{1}{X_{AN}} + \frac{1}{X_{BN}}\right) = \frac{I\rho}{2\pi}G \tag{2.3}$$

Such an arrangement corresponds to the four-electrode spread which is normally used in resistivity fieldwork.

Solving Eq. (2.3) for resistivity (ρ):

$$\rho = 2\pi\frac{\Delta V}{I}\frac{1}{G} = 2\pi\frac{R}{G} \tag{2.4}$$

where G stands for the geometric factor and R for the measured resistance.

Equation 2.4 gives the true resistivity of an electrically homogenous subsurface (Dentith and Mudge, 2014). A situation in the field which is very rare and unlikely to happen since the earth in most parts is complex and layered. In most cases detection of anomalous conductivity in various forms is the aim (Telford, Geldart, and Sheriff, 1990). In a heterogeneous environment, the resistivity is known as the apparent resistivity (ρ_a) of the surface (Dentith and Mudge, 2014) meaning that the measured value actually represents the average resistivity of the entire subsurface across the survey area and does not equal the true resistivity.

2.1.1 Survey design

Each of the traditional electrode configurations has there own strengths and weaknesses which are summarized by extensive field tests and sensitivity studies, making certain arrangements more or less applicable depending on survey objectives (Everett, 2013). In practice, the electrodes are typically arranged along a 2-D line, otherwise, field works and result interpretation are complicated (Telford, Geldart, and Sheriff, 1990). One of many standard geometries such as the Wenner, Schlumberger, dipole-dipole and pole-dipole are shown in Figure 2.1

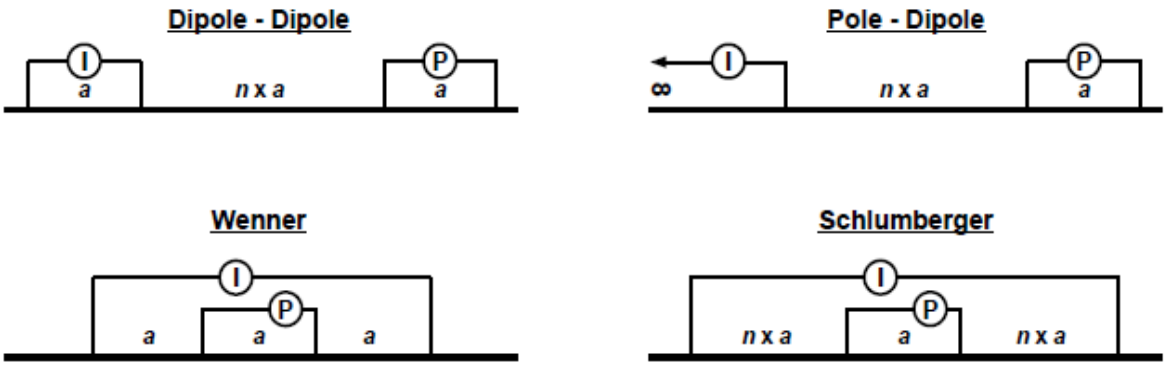

FIGURE 2.1: Common 2-D resistivity survey geometries (Dentith and Mudge, 2014).

The Wenner and Schlumberger arrays are designed and more suited to profile vertical changes in Earth's resistivity. Schlumberger sounding can achieve good depth penetration with sufficiently large AB separations but with limited lateral resolution. The Wenner array has a moderate depth of investigation, but the strongest signal strength compared to other arrays. The Dipole-dipole and pole-dipole layouts have a superior lateral resolution. However, the voltage measurements across the electrodes MN and the signal-to-noise ratio deteriorates at large values of n are susceptible to distortion by small-scale, near-surface heterogeneities (Everett, 2013).

2.2 Magnetism

The magnetic method acquires information related to the direction, gradient, or intensity of the Earth's magnetic field. This geophysical method provides a quick way to map the areal distribution of magnetic anomalies across the surface and is frequently used in applications such as detecting different types of ore bodies, mapping faults, fractures, zones with different mineralization and environmental studies (Othniel, 2014). The magnetic method's measurements are usually cheaper and are made more easily than most geophysical methods and corrections are practically unnecessary but, as all potential methods, lack uniqueness of interpretation (Telford, Geldart, and Sheriff, 1990) due to the dipolar nature of the field and other various polarization effects (Othniel, 2014). Geologic constraints with help of other geophysical methods, however, can considerably reduce the level of ambiguity (Othniel, 2014).

A brief theory of the magnetic method is described according to Prem V. Sharma, 1997.

Maxwell's set of equations describes the relation between an electric and magnetic vector field. The two Maxwell equations relating to the magnetic field:

$$\nabla \times H = J + \frac{\partial D}{\partial t} \tag{2.5}$$

and

$$\nabla \cdot B = 0 \tag{2.6}$$

where H is the magnetic field (A/m), B is the magnetic induction (Wb/m^2 or T), J is the electric current density (A/m^2), and $\partial D/\partial t$ is the electric displacement current density.

The scalar magnetic potential (of a pole) W, at a point due to a pole of strength p located at distance r is given by:

$$W = \frac{\mu_0 p}{4\pi r} \tag{2.7}$$

where μ_0 is the permeability constant of $4\pi \times 10^{-7}$ H/m.

The magnetic field B (T) is defined as the force exerted by a pole of strength p on a unit pole at distance r. It follows from Eq. (2.7) that the B field at point P is:

$$B = -gradW = \frac{\mu_0 p}{4\pi r^2} r_1 \tag{2.8}$$

where r_1 is a unit vector directed from the magnetic pole p towards P. The magnetic field B is expressed as the flux density in Teslas (T), the pole strength p is measured in Ampere-meters (Am) and distance r in meters (m).

The magnetic field H (A/m) is produced by the flow of current in wires. The H field is:

$$H = i/r2 \tag{2.9}$$

where i is current and r radius of the wire.

The relationship between B and H fields is given by:

$$B = \mu H = \mu_r \mu_0 H \tag{2.10}$$

where μ is the absolute permeability of the medium, the ration μ_r/μ_0 is called the relative permeability μ_r of the medium.

The magnetic potential of a dipole, with two equal but opposite poles $+p$ and $-p$ which represents an idealized magnet, and field B expression can be derived from Eqs. (2.7) and (2.8):

$$W = \frac{\mu_0}{4\pi}\frac{Mcos\theta}{r^2} \tag{2.11}$$

$$B_r = -\frac{\partial W}{\partial r} = \frac{\mu_0}{4\pi}\frac{2Mcos\theta}{r^3} \tag{2.12}$$

$$B_\theta = -\frac{1}{r}\frac{\partial W}{\partial \theta} = \frac{\mu_0}{4\pi}\frac{Msin\theta}{r^3} \tag{2.13}$$

where M is the dipole moment, B_r the magnetic field in the direction of r, B_θ the magnetic field normal to r at the point of observation P.

2.3 Electromagnetics

The electromagnetic method is used to determine the distribution of electrical conductivity in the subsurface (Schaa and Fullagar, 2010) by using the phenomenon of electromagnetic induction to create the current flow and measure the magnetic fields associated with it (Dentith and Mudge, 2014). The electromagnetic method best responds to good conductors at shallow depths and mostly is used in mineral exploration (Telford, Geldart, and Sheriff, 1990), in particular metal sulphide and metal oxide mineralisation detection, for regional and prospect scale (Dentith and Mudge, 2014).

The electromagnetic methods concept is based on the Maxwell equations which describe the relation between electric and magnetic vector fields. Four fundamental electromagnetic laws described by James Clerk Maxwell in 1865 are:

$$\nabla \times E = -\frac{\partial B}{\partial t} \tag{2.14}$$

where E is the electric field intensity (V/m) and B is the magnetic induction expressed in Wb/m^2 or T.

$$\nabla \times H = J + \frac{\partial D}{\partial t} \tag{2.15}$$

where H is the magnetic field (A/m), J is the electric current density (A/m^2), and $\partial D/\partial t$ is the electric displacement current density.

$$\nabla \cdot D = q_v \tag{2.16}$$

where D is the electric flux density (C/m^2) and q_v is the electric charge density (C/m^3).

$$\nabla \cdot B = 0 \tag{2.17}$$

where B is the magnetic induction defined in Wb/m^2 or T.

The wave equations follow by first taking the curl of Faraday's law Eq. (2.14) and Ampere's law (2.15), and substituting each into the other. Wave equations for vector fields E and H in time domain:

$$\nabla^2 E = \mu\sigma\partial_t E + \mu\epsilon\partial_t^2 E \tag{2.18}$$

$$\nabla^2 H = \mu\sigma\partial_t H + \mu\epsilon\partial_t^2 H \tag{2.19}$$

2.4 Self – Potential

The self-potential method is a passive geophysical method based on measuring the naturally occurring variations in electrical potential (Dentith and Mudge, 2014). The SP method is non-destructive, low cost, and sensitive to various kinds of signals, for instance, fluid flows, contaminant diffusion and redox processes, and allows real-time monitoring of the subsurface (Revil and Jardani, 2013). The mineral exploration method excels in its ability to detect natural potential variations associated with metal sulphide, metal oxide and carbonaceous mineralization (Dentith and Mudge, 2014).

Fundamental equations used to explain and interpreted SP signals are based on the quasi-static regime of Maxwell equations. The total electric density in a porous material (Revil and Jardani, 2013):

$$J = \sigma_0 E + J_s \tag{2.20}$$

where E is the electric field (Vm^{-1}), σ_0 is the electrical conductivity of the porous material (Sm^{-1}), and J_s is a source current density ($Am^{\check{}2}$) associated with any disturbance that can affect the movement of charge carriers.

In the magnetoquasi-static limit of the Maxwell equations, for which the displacement current is neglected, the continuity equation for the total current density is:

$$\nabla \cdot J = 0 \tag{2.21}$$

which means there is no storage of electric charges inside the control volume.

Combining Eqs. (2.20) and (2.21) the self-potential field ψ is the solution of the following equation:

$$\nabla \cdot (\sigma_0 \nabla \psi) = \nabla \cdot J_S \tag{2.22}$$

This is the fundamental field equation in the interpretation of (quasi-static) self-potential signals.

3 INVERSION

In a heterogeneous environment (see Section 2.1) the resistivity is known as the apparent resistivity that is calculated using the current, potential difference and a geometrical factor. The measured apparent resistivity is the average resistivity affected by all subsurface through which the induced electric current flows. The standard processing tool is to apply the inversion procedure to invert the measured apparent resistivity data into a "true" subsurface resistivity.

Magnetic measurement data indicates local variation in the Earth's magnetic field. This observed variation is caused by different magnetic minerals in the subsurface having certain physical properties, such as magnetic susceptibility and remanent magnetization. Distribution of magnetic minerals defines the magnitude and shape of the measured anomaly (Dentith and Mudge, 2014). By applying magnetic inversion methods, it is possible to calculate from the observed data an accurate structural model of the subsurface.

All inversion methods essentially try to iteratively find a subsurface model whose response agrees with the measured data subject to certain restrictions and within acceptable limits. A measure of the quality of the produced model is the data misfit between the calculated observations and actual data (Loke, 2001).

3.1 Forward problem

Forward modeling is a significant component of any inversion program since it is necessary to calculate the theoretical values for the model produced by the inversion routine to see whether it agrees with the measured values (Loke and Barker, 1996). A set of model parameters may be used to predict the observation, and describe the relationship between the model and the observed outcome (Arkoprovo, 2017). Mathematically, a forward problem can be formulated:

$$M \rightarrow d = g(M) \tag{3.1}$$

where M is the model parameters, d is the data or the observed parameters, and g is the forward operator that describes the relationship between the model parameters and the data.

Forward problems are usually well-posed, have a unique solution that exists in the model space, and behavior changes continuously with the initial conditions (Vauhkonen, Tarvainen, and Lahivaara, 2016).

The relationship between the model parameters and the model response can be calculated using various numerical methods, including finite-difference (Dey and Morrison, 1979) and finite-element methods (Silvester and Ferrari, 1996).

3.2 Inverse problem

The opposite of a forward problem is an inverse problem, meaning that the outcome is used to calculate the cause. Inverse problems do not necessarily have unique (there can be many models that fit the data) and stable solutions (poor initial conditions, arbitrarily small changes or measurement errors can produce large errors in the solutions), that is, they are often non-linear, and inherently ill-posed, meaning that at least one of the three conditions of well-posedness is not met (Vauhkonen, Tarvainen, and Lahivaara, 2016).

For a linear inverse problem, the formula from the forward problem Eq. (3.1) is rewritten as:

$$d = gM \tag{3.2}$$

can be used to invert the operator g to find the model parameters M

$$M = dg^{-1} \tag{3.3}$$

Finding the resistivity or magnetic susceptibility distribution in the subsurface that will reduce the discrepancy between the calculated and measured apparent resistivity and magnetic susceptibility values is the inverse problem of ERT and magnetic methods (Palka et al., 2009).

The data misfit vector can be defined as

$$\Delta d = d_m - d_c \tag{3.4}$$

To find the optimal solution to the inverse problem, iterative minimization of the misfit between the observed data and the calculated data is carried out. For the $L1$ - norm data misfit, the normalized data misfit function (L_{1N}) is given by:

$$L_{1N} = \frac{1}{m} \sum_{j=1}^{m} \left| \frac{d_{cj} - d_{mj}}{\Delta d_{mj} + \varepsilon} \right| \tag{3.5}$$

The L1 norm is the sum of the absolute value of the entries in the vector. The L2 norm is the square root of the sum of the entries of the vector (Loke, 2001). For the $L2$ - norm data misfit function is calculated in a similar way as for $L1$ using the following equation:

$$L_{2N} = \sqrt{\frac{1}{m} \sum_{j=1}^{m} \left(\frac{d_{cj} - d_{mj}}{\Delta d_{mj} + \varepsilon} \right)^2} \tag{3.6}$$

with d_c and d_m are the calculated and measured data and Δd_m is the estimated error. To avoid an infinite value for the normalized misfit a small positive value ε to the denominator is added. Ideally, the normalized misfits should be about 1.0 if the calculated values fall within the range of the noise level(Loke, 2001).

3.3 Optimization

In all optimization methods, an initial model is modified in an iterative manner so that the difference between the model response and the observed data values is reduced. Numerous optimization methods can be applied to address the problem of fitting data with regularization (Ye, Roosta-Khorasani, and Cui, 2019). In this case numerical local, gradient based method was applied - Gauss-Newton least-square optimization with regularization.

Unlike from Full-Newton method Gauss-Newton method neglects the second term of the Hessian matrix because it is insignificant small number and requires additional computational power (Snieder and Trampert, n.d.).

The Gauss-Newton equation is the following:

$$J^T J \Delta q_i = J^T f \tag{3.7}$$

where f is the discrepancy vector, Δq is the model parameter change vector, J and J^T are the Jacobian matrix and its transpose.

A more localized method that is often used for refining already inverted model to decrease misfit is the Marquardt-Levenberg modification to the Gauss-Newton equation that is given by:

$$(J^T J + \lambda I)\Delta q_k = J^T f \tag{3.8}$$

where I is the identity matrix, λ is known as the Marquardt or damping factor. This method is also known as the damped least-squares method. This equation describes only the general optimization method; further modifications in the algorithm may be applied to minimize the spatial variations in the model parameters (Loke, 2001).

3.4 Regularization

Apart from minimization that is being resolved using optimization, the inverse problem is also affected by non-uniqueness - infinite variations of the model can fit the observed data to the same extent. Therefore inverted model requires to abide by certain constrains to reduce the non-uniqueness of the inverse solution, and is undertaken by the regularization (Oldenburg and Li, 2005).

The regularization method with smooth ($L2$) or the robust/ blocky ($L1$) constraint term is often used to solve the inverse problem. The reconstruction method with $L2$ regularization introduces an additional smoothing parameter to preserve a stable solution in the image reconstruction process. However, one of the downsides is that layer boundaries of different conductivities are not well defined as they appear rather smooth (Zhao, Xu, and Dong, 2014). The obtained model with smooth

variation in the resistivity values is most suitable where subsurface resistivity also changes gradually. However, if the subsurface consists of bodies, and structures with sharp boundaries the conventional least-squares smoothness-constrain method tends to smooth out the boundaries (Loke, 2001).

The regularization method with $L1$ norm is more suited for dealing with "outlier" data points and the over-smoothing effect constraints. Resulting layer boundaries are better defined with sharper contrast, however at a risk of having a greater apparent resistivity RMS error (Zhao, Xu, and Dong, 2014).

4 LATERITE PROSPECTION CASE STUDIES

The laterites that form under tropical weathering conditions are weathering-related phenomena of importance (Dentith and Mudge, 2014) and have been investigated as ore deposits for Al, Fe, Ni, Au, Nb, and P (Sowards et al., 2018). Following examples from different publications, books, and conference papers will focus on different geophysical methods which were applied for laterite exploration.

In exploration geophysics, measurements of physical quantities made at or above the ground surface are used to conclude information about existing geology (Moon, Whateley, and Evans, 2006). Geophysics plays a large part in ore exploration, used to assist in regional mapping, for sole exploration targets, prospect evaluations and downhole logging (Kerr et al., 1994). The physical properties of the geological environment most commonly measured in mining geophysics are density, magnetism, radioactivity, and elastic and electrical properties. As for metal formation prospection, the most commonly used are magnetism, radioactivity, electrical properties, and density for geological mapping of prospective terrains, detection/ delineation of the mineralized environment, and downhole logging (Dentith and Mudge, 2014).

In the literature, not many examples were found about applying geophysical methods to the lateritic environment. One of the first publications found in various databases is "Exploration of Burundi Nickeliferous laterites by electrical methods" by M. Peric written in 1981. In this publication, the laterites were investigated by means of resistivity sounding and well-logging. The results obtained have been used in the initial assessment of ore deposits and the further planning of additional exploration. The investigation area is almost entirely covered by laterite, which overlays bedrock - ultrabasic rocks. A laterite profile in Burundi can be generalized by three horizons: canga, ferralite and saprolite. Canga and ferralite are highly resistive, but saprolite is low resistivity. Fresh ultrabasic rocks are highly resistive; however, serpentinized ultrabasics have considerably lower resistivities. Prospecting for laterites by electrical sounding showed that the development of laterite horizons in a nickel deposit correlates with the surface morphology of a weathered ultrabasic massif. Thus, the method can be used in the preliminary exploration of such deposits (Petric, 1981).

The next study "Imaging lateritic bauxite bearing zones in Ekiti, Southwestern Nigeria, using magnetic and electrical resistivity tomography techniques" by J. Amosun et al. in 2020 is aimed at imaging the subsurface geology of lateritic bauxite deposit in Orin Ekiti, Southwestern Nigeria, using aeromagnetic and electrical resistivity tomography methods. The 2-D ERT profiles and 3-D inversion results show a

high resistivity zone which ranges from 154 - 3814 to 371 - 2600 Ωm indicating the presence of weathered material (laterite), hosting a bauxite deposit. The migmatite gneiss and granitic rocks (unaltered parent rocks) are of considerably lower resistivity (from 53.8 - 290 to 124 - 279 Ωm) than the weathered charnockitic rock and by extension bauxitic zones. The depth extent and structural signature interpreted from magnetic data show that a significant deposit in the study area is at shallow depth, which corresponds with the geology of lateritic bauxite. The lithological boundaries were mapped out based on the total horizontal derivative (THDR) map (Figure 4.1).

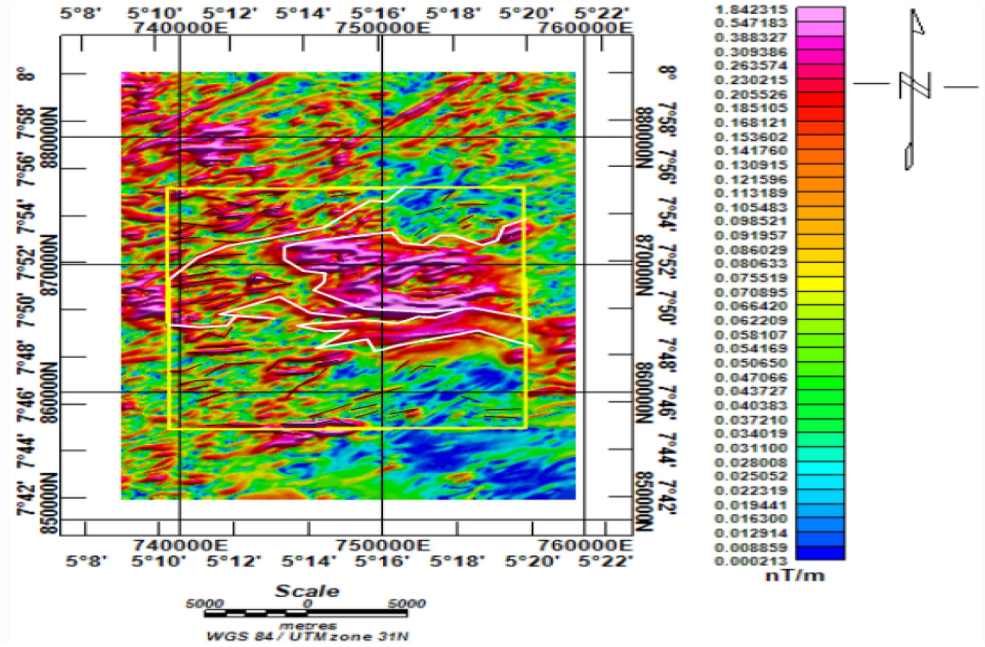

FIGURE 4.1: Total horizontal derivative (THDR) map with highlighted lithological borders (Amosun et al., 2020).

One example is also given in the publication "Evaluation of Lateritic Soil from Field Resistivity Data at Okada, South-South, Nigeria" by Arekumo Thank God and Lawrence O. Oghale. Both authors reviewed the electrical properties of laterites to evaluate the depth and area extent of laterite topsoil in Okada South-South, Nigeria. ERT survey was made along four profiles using Schlumberger – Wenner configuration. A resistivity value stated for laterites was 600 -1000 Ωm, 300 – 600 Ωm for lateritic soil with varying degrees of laterization, while 100 Ωm and below was more clay sediments related. The electrical resistivity tomography method was effective in delineating clay dominant units from lateritic areas (Figure 4.2).

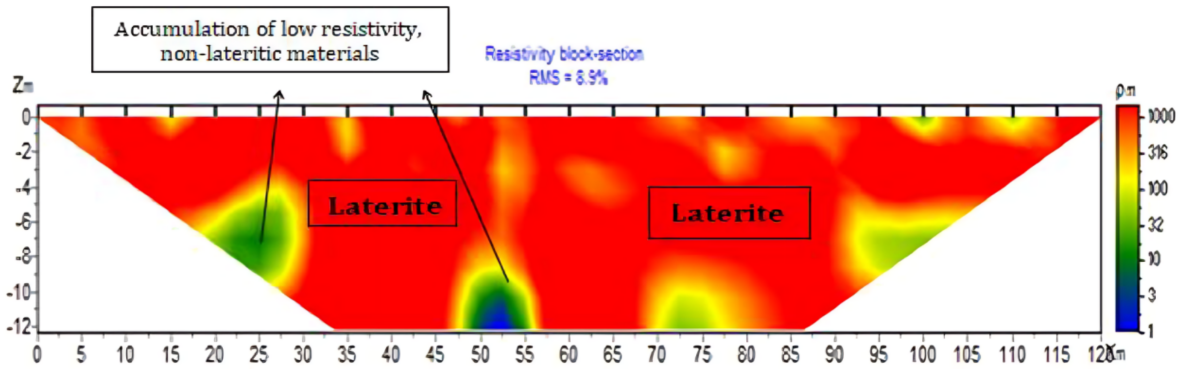

FIGURE 4.2: ERT 2-D tomography profile (Arekumo and Lawrence, 2019).

In all, overviewed examples from different publications show that the ERT and magnetic methods can be applied effectively with success in a lateritic environment. Although the aim for each publication differs in terms of expected results and conclusions. It has to be noted that the geological environment in each location is different and unique, and the method which is working effectively and gives desired results in one location could be failing in another.

The most popular geophysical method for laterite investigation seems to be the ERT, judging by available publications, book examples, and conference papers. Unfortunately, the SP and electromagnetic method case studies for the lateritic environment could not be found on any scientific paper database on the internet. However, that does not limit the possibility of useful application for this kind of geological environment.

5 GEOLOGICAL SETTING

The Kraubath Ultramafic Massif (KUM) is located in SE Austria, 30 km SW of Leoben. The KUM covers an area of 28 km^2, and it is surrounded in the vicinity of the Mur valley. KUM is vertically separated by the Mur valley into two parts – Gulsen (west of the valley) and the Preger Massif (east of the valley).

Morphologically, KUM is a part of the Speik complex, thus, belonging to the Silvretta-Seckau nappe system (Fig. 5.1). The composition and origin of the Speik complex are rather complicated – a variety of scientific interpretations exist related to the magmatic and metamorphic evolution of the complex. Abridging from geochemical characteristics and patterns, KUM is interpreted as a differentiated ultramafic intrusion, and it resembles a part of the ophiolite complex, accordingly, KUM is representing residual mantle (Melcher and Meisel, 2004).

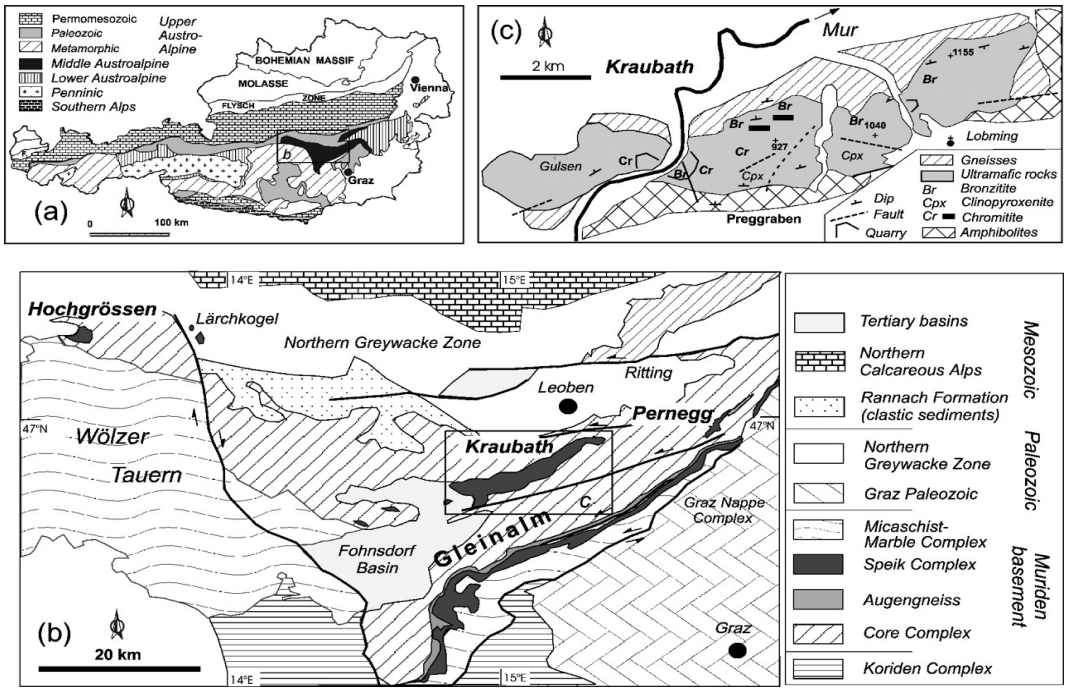

FIGURE 5.1: Geological sketch maps illustrating the position of the Speik Complex in the Middle Austroalpine basement of Austria. (a) Major tectonic units of Austria after Frank, 1987. (b) Generalized map of the Austroalpine units in Styria after Neubauer, 1988. (c) Simplified map of the Kraubath Massif showing locations of orthopyroxenite ('bronzitite'), clinopyroxenite and chromitite (Melcher and Meisel, 2004).

The age of the Speik Complex is possible to define by its overlying Micaschist – Marble Complex, where a Silurian to Devonian age is suggested by Becker, 1981 and Frisch and Neubauer, 1989. Therefore, the age for strongly fragmented ophiolite of the Speik Complex is presumed to be an Early Paleozoic era. Together with underlying amphibolites and plagioclase-gneisses, the Speik Complex represents a late Cambrian (early paleozoic) magmatic belt at the NW rim of Gondwana (Thalhammer and Heinrich, 2015).

KUM area experienced a relatively lower level of serpentinization compared to other ultramafic massifs of the Speik complex, therefore revealing abundant relics of primary minerals (Melcher and Meisel, 2004). The lithology of KUM is composed of harzburgite, dunite, dykes of orthopyroxenite complemented with a negligible amount of schlieren and bands of chromitite (Thalhammer and Heinrich, 2015).

The chromite ore host rock is olivine serpentine rock, which is completely weathered to a mica containing clay in the upper layers. In the middle parts olivine serpentine rock is a greener, silk-glossy mineral. The base is dense, brownish rock with chromites of black, metallic color. The middle and the lower part are attributable to the chromite occurrence at Kraubath itself, while the upper parts lead to yellowish-brown iron hydroxide, the brown-iron stone with bean-ore, and with macroscopically difficult visible, isolated chromite grains. This olivine serpentine rock extends over a larger area; its length extends from the area of Kraubath in the west starting this side of the Mur as far as to Pernegg on the Mur in the east — but with some interruptions (Söhle, 1901).

The chromite ore is formed in secondary processes. The hot springs partially dissolved the chromium iron ore of the actual chrome mass and flowed on the crevices and corridors of the parent rock, penetrated the higher parts and ores (especially the iron ore contained in the chromite) and deposited the chromite bearing in the now formed clay (Söhle, 1901).

In Rablstollen area, where numerous geophysical methods were applied as part of the master thesis, a borehole is located (Figure 5.2). The purpose of the borehole was for mineral exploration thus determining laterite (ore containing chromite) layers' thickness and depths. Laterite forms more than one layer in various thicknesses starting from a few centimetres to more than 2 meters. The upper part of the section consists of the overburden till $\sim$ 2 meters, then laterite layers are located till $\sim$ 11 m. Between laterite layers, unspecified sediment interlayers are embedded. Laterite overlays serpentinite which is weathered in the upper parts of the geological section.

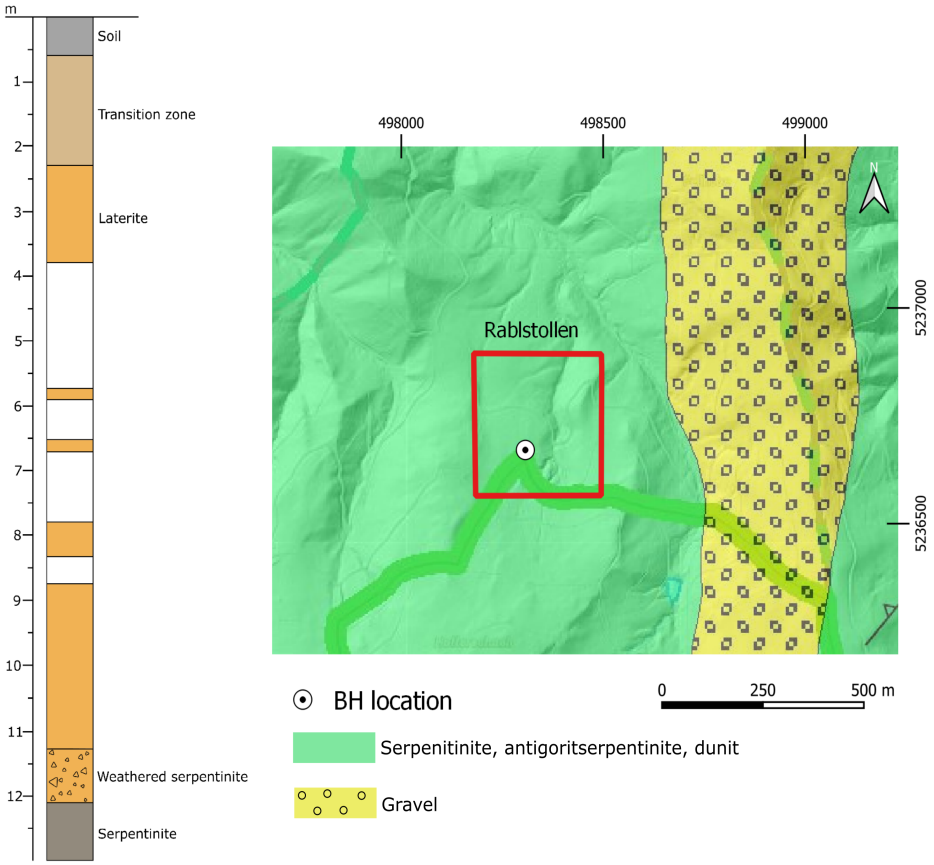

FIGURE 5.2: Borehole section (drilled by MINEX Mineral Explorations GmbH) and location shown on a geological map of the study area. Reproduced from GIS Steiermark. Used coordinate system WGS 84 UTM zone 33N.

5.1 Historic mining

In the 19th and 20th centuries, small deposits of chromite and cryptocrystalline magnesite were mined in dunites and highly serpentinized harzburgites, but the mining process was more cumbersome than productive due to the transporting cost, both mines being located remotely from the production facilities in Kraubath, and chromite quality. Chromite-containing ore, which contains 4% Cr, could not be enriched to 14% Cr for use in steel production (Söhle, 1901).

In Rablstollen and Ederstollen areas, two small, underground mines and one open pit (in the Ederstollen) were located (Fig. 5.3) referring from Matz, 1940. The absolute positioning of the mining sketch maps is only tentative and based on topographic similarities. The actual location could have varied. Nowadays entrances for both mines are not to be found. Most probably entries were sealed off or collapsed. It is not known whether mining shafts are still there or filled in with debris.

From the description of Matz, 1940 the Ederstollen old mine (Fig. 5.3 A) consists of an open pit mine on the west side, an upper tunnel (a few meters deep), and a substructure tunnel which is 10 m deeper than the upper tunnel. The open pit exposes small ore outcrops. The pit is undercut by an upper tunnel which is 30 m long in pure ore and ends at a fault (strike N-S). In the substructural tunnel first 20 m is serpentinite which cuts off at a fault zone characterized by talc and asbestos. After the fault zone, poor-quality ore starts. Both tunnels run almost parallel. The thickness of the ore deposit can be estimated at 15 to 20 m.

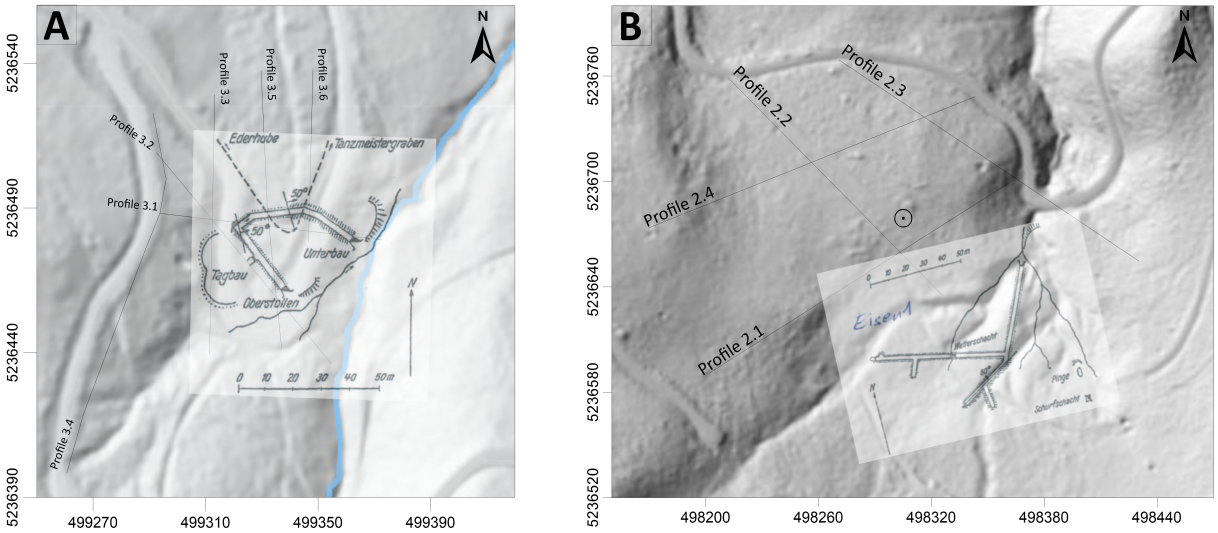

FIGURE 5.3: Old mining tunnels schemes at (A) Ederstollen and (B) Rablstollen. Black lines indicate ERT profile line location. The black dot at (B) shows the borehole location. Used coordinate system WGS 84 UTM zone 33N.

The Rablstollen old mine (Fig. 5.3 B) consists of two fork-like shafts. Ore is revealed beneath 1.5 to 2 m thick overburden which consists of loose material. Ores thickness is 3 m at the shafts entry but towards the south, it may have reached 15 m in the mining shaft. This observation about ore thickness is confirmed by the results of a few boreholes that were drilled in the vicinity of the pit at the time (Table 5.1). Unfortunately, the exact location of the boreholes is unknown.

TABLE 5.1: Overburden and ore thickness from boreholes located near the Rablstollen pit.

	Borehole No.			
	1	2	3	4
overburden (m)	2.00	2.00	-	1.90
ore (m)	1.80	7.00	11.30	1.80

For both mines, rough estimations of laterite ore quantities were made by Matz, 1940. For Rablstollen ore quantity being around 300000 t but for Ederstollen about 180000 t. In the same publication, iron-oxide content is specified to be 66.24%, however, the location of the sample collection and the position within the section is unknown.

6 MATERIAL AND METHODS

This chapter envelops applied methods for the case study - magnetic, electrical resistivity tomography, self-potential and electromagnetics, data acquisition, processing, and inversion. All geophysical data measurements were carried out by the University of Leoben between the years 2016 and 2021 during various field campaigns in the Kraubath area – Manghube, Rablstollen, Ederstollen, Tanzmeistergraben 1 and 2 (Figure 6.1).

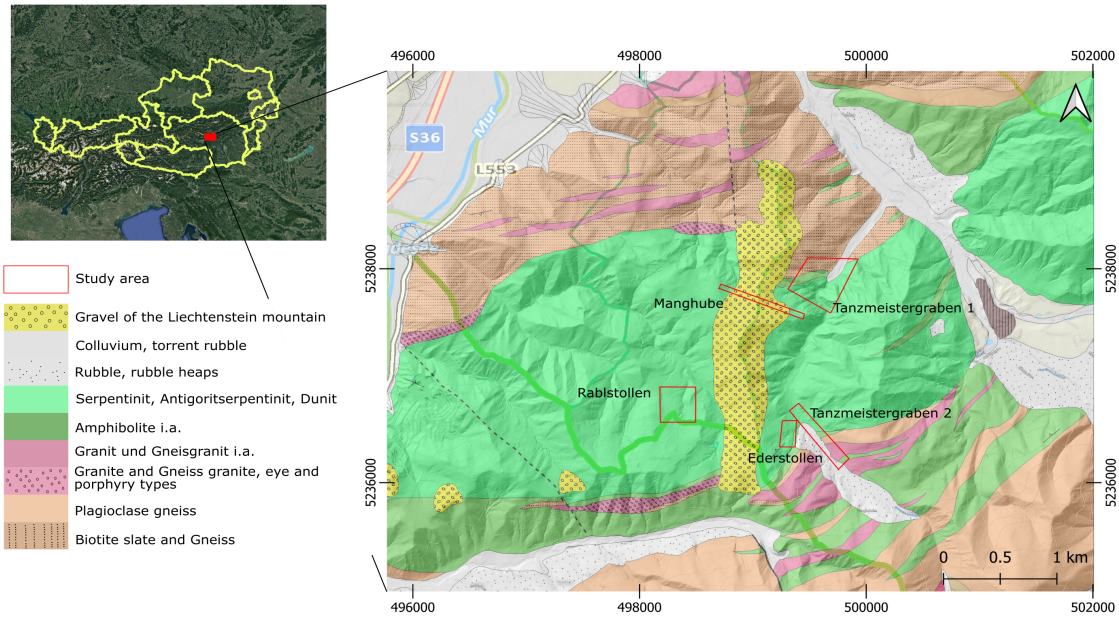

FIGURE 6.1: Geological map of the study area. Reproduced from GIS Steiermark. Used coordinate system WGS 84 UTM zone 33N.

In Ederstollen and Rablstollen, the main target was to identify and approximate the boundaries of laterite bodies. However, in Manghube area, various geophysical methods were used to define a boundary between Neogene sediments, which contain mainly gravel/ sand, and crystalline rocks, containing serpentinite and dunite and possibly locate ore bodies between sedimentary rocks, as well. Acquired resistivity values from sedimentary rocks and bedrock were used as guidelines for Ederstollen and Rablstollen ERT data interpretation.

In Tanzmeistergraben 1 and Tanzmeistergraben 2, measurements were made to see whether it is possible to recognize boundaries between different types of lithologies. In the case of Tanzmeistergraben 1 to identify boundaries between serpentinite/dunite, amphibolite, and gneiss. For Tanzmeistergraben 2, boundaries between amphibolite, granite, plagioclase gneiss and serpentinite/ dunite.

6.1 Electrical Resistivity Tomography

ERT measurements were conducted in the Manghube, Rablstollen, and Ederstollen areas. Due to varying resistivities between rocks in the area, contrasts should be well identifiable. In the Manghube area, thickness, boundaries determination of Neogene sediments, and each geological unit governing resistivity values were the main exploration targets. Lower resistivity is expected from gravel, compared with serpentinite and dunite, which has higher resistivity. Weather conditions while conducting measurements were humid and topsoil was moderately saturated with water, resulting in decreased penetration depth of ERT due to low resistivity values at the surface.

In the Rablstollen and Ederstollen areas, lower resistivities are looked for with an aim to identify laterite above bedrock - serpentinite, and dunite. Weather conditions in Rablstollen and Ederstollen year 2021 were dry and sunny, providing slightly high resistivity values at the surface. The Ederstollen year 2020 was rainy, which could affect measurement penetration depth to the downside.

6.1.1 ERT data acquisition

The 2-D ERT data were acquired along 11 profiles (Figure 6.2) using AGI Sting or Lippmann 4point light 10W imaging system with GeoTest 2.47 version software for controlling geoelectric equipment. The Lippmann 4point light 10W is an AC instrument. The output current switches from positive to negative with selectable frequencies. In our case, 4.16 Hz. The receiver not only records the potential differences but also the phase shift between the output current and voltage, providing the possibility to measure induced polarization (IP). The accuracy of the instrument is 0.1%. The instrument consists of a total of five electrode chains, each containing 20 stainless electrodes, with 5 m being the maximum space between electrodes. Electrode contact resistance test was done before every resistivity data measurement.

AGI Sting is a single-channel instrument that works on the same principles as Lippmann 4point light 10W by injecting a current, reversing polarity, and injecting the current again. Only induced polarization is measured in the time domain. The accuracy of instruments is less than 1%. This instrument was used only for one profile – Manghube, and IP data were not acquired.

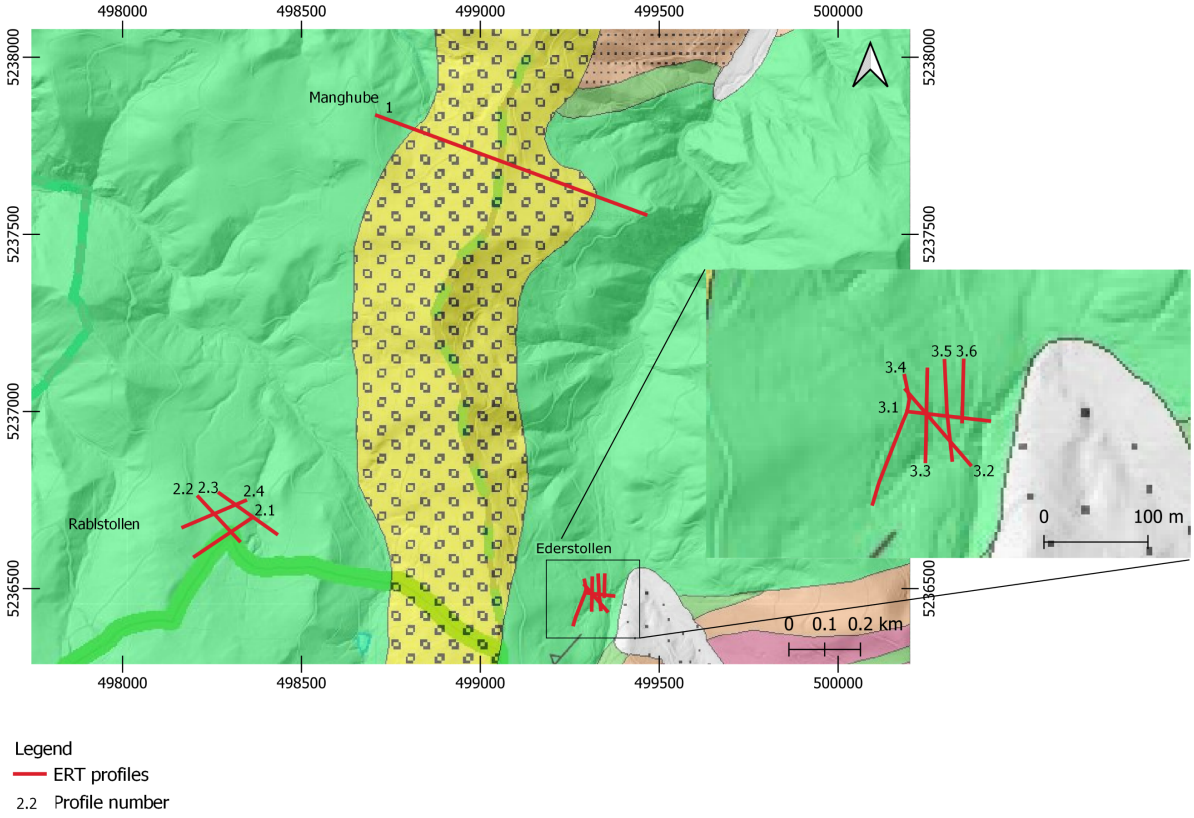

FIGURE 6.2: ERT data acquisition survey profiles. Used coordinate system WGS 84 UTM zone 33N.

The Wenner (Wenner alfa) and dipole-dipole array configurations were used with electrode spacing varying from 1 to 10 m depending on the profile. Profile lengths were between 60 – 790 m. The Wenner array was applied because it provides a good resolution of horizontally layered structures, depth penetration and has obtained successful results in previous studies. The dipole-dipole array produces a good lateral resolution of steeply dipping features, although signal amplitude may be low (Dentith and Mudge, 2014). The data acquisition parameters are summarized in Table 6.1.

TABLE 6.1: Electrical resistivity tomography survey parameters.

Location	Date	Profile number	Survey equipment	Electrode configuration	Used frequency (Hz)	Electrode spacing (m)	Number of electrodes	Measured apparent resistivity data points	Type of measurement (Ω m)($mSec$)	Length of profile (m)	Weathered condition
Manghube	26.04.2016	1	AGI Sting	Wenner alfa	4.16	10	80	684	Resistivity	790	mostly dry to slightly humid topsoil
Rablstollen	24.03.2017	2.1	Lippmann 4point light 10W	Wenner alfa	4.16	2	100	1617	Resistivity Chargeability	198	sunny and dry
	24.03.2017	2.2					80	1027		158	
	27.03.2017	2.3					100	1617		198	
	27.03.2017	2.4					91	1335		180	
Ederstollen	25.06.2020	3.1	Lippmann 4point light 10W	Wenner alfa Dipole-Dipole	4.16	1	91	1335	Resistivity Chargeability	90	rainy, water-saturated topsoil sunny and dry
	26.06.2020	3.2				1	100	1617		99	
	29.06.2020	3.3				1	98	1552		97	
	13.04.2021	3.4				1.3	100	1617		128	
	27.04.2021	3.5				1	80	2069		79	
	15.04.2021	3.6				1	60	1232		60	

6.1.2 ERT data processing and inversion

The apparent resistivity pseudosections were inverted using the RES2DINV inversion program, developed by Loke and Barker, 1996, to build a model of the media resistivity in a 2-D vertical section.

Manghube

In total Manghube profile consisted of 1027 data points from which 176 values were deleted for various reasons (see Chapter 7). From the rest of the 851 data points, 167 points were removed after trimming the data set consisting of a high misfit from the measured and calculated apparent resistivity using a cut-off value of 30 %, to filter out the data points contaminated by noise.

The Robust inversion (or $L1$ - norm) was applied for the inversion of resistivity data because sharp boundaries were expected to be present and to reduce the effect of a few data points that might be noisier on the inversion results. The standard technique of Gauss-Newton optimization was used in the inversion program. The width of the model cells was set to half the electrode spacing of 10 m. This setting is considered to improve the results when there are very large resistivity variations near the ground surface (Loke and Barker, 1996). The iterated resistivity data comprises of 1264 model blocks in 16 resistivity levels.

The ERT model was generated within six iterations by minimizing the absolute error up to 10.4% taking into consideration the damping factor and adjusting it to help reduce the L1 misfit functions. The absolute error value was found to be acceptable given intensive data filtering, a considerably large number of deleted data points and inverted sections' credibility from a geological point of view. The inversion method was performed by picking a damping factor of 0.15 which is considerable regarding absolute errors value and normally applied for data sets with a low to moderate noise level. Side-effect reduction was applied. The topography was incorporated into the inversion model to eliminate any artificial anomalies generated by the effect of the topography. All other model parameters were selected to minimize absolute error and the number of iterations to avoid fitting noise.

Rablstollen

In Rablstollen area in total, four ERT profiles were made. The data quality for all four profiles was satisfactory - measurement error did not reach 2 % in any of the data points (see Chapter 7), and no data trimming was applied. The width of the model cells was set to half the electrode spacing of 2 m. The iterated resistivity data comprises of an average 1522 model blocks in 17 resistivity levels.

The ERT models were generated within six iterations using Robust inversion. The standard technique of Gauss-Newton optimization was used in the inversion program. The absolute errors obtained varied between 0.92 and 1.40 % with an average of 1.40 % taking into consideration the damping factor and adjusting it to help reduce the L1 misfit functions. All the absolute errors obtained in the inversion process were acceptable. The inversion method was performed by picking a damping factor of 0.15 which is considerable regarding absolute errors value and normally

applied for data sets with a low to moderate noise level. Side-effect reduction was applied. The topography was incorporated into the inversion model to eliminate any artificial anomalies generated by the effect of the topography. All other model parameters were selected to minimize absolute error and the number of iterations to avoid fitting noise.

Ederstollen

In total six ERT profiles were made in Ederstollen. The data quality for all profiles was satisfactory – measurement error exceeded 2% only in one case – profile 3.5 (see Chapter 7), and no data trimming was applied. The width of the model cells was set to half the electrode spacing of 1 or 1.3 m. The iterated resistivity data comprises of an average 1198 model blocks in 17 resistivity levels.

The inversion steps followed the same routine as for Rablstollen profiles. The absolute errors obtained varied between 0.79 and 4,0 % with an average of 1,98 % taking into consideration the damping factor and adjusting it to help reduce the L1 misfit functions. All the absolute errors obtained in the inversion process were acceptable. The inversion method was performed by picking a damping factor of 0.15 which is considerable regarding absolute errors value and normally applied for data sets with a low to moderate noise level. Side-effect reduction was applied. The topography was incorporated into the inversion model to eliminate any artificial anomalies generated by the effect of the topography. All other model parameters were selected to minimize absolute error and the number of iterations to avoid fitting noise.

6.2 Magnetism

The magnetic data were measured in the Kraubath area in various locations – Manghube, Rablstollen, Ederstollen, Tanzmeistergraben 1 and 2. The purpose of the applied magnetic method varies for several locations.

In Rablstollen and Ederstollen measurements were carried out for laterite exploration, more specifically for the morphological boundaries of the bodies. By applying the magnetic method, a contrast for identifying laterite was expected versus bedrock - serpentinite and dunite.

Magnetic profiles in Manghube area cut through sedimentary rocks - gravel and sand, crystalline rocks - serpentinite and dunite. The magnetic contrast between these two lithologies was expected to be well visible. Possibly laterite bodies could have been embedded at the boundaries between sediment and underlying rocks, and if so, the magnetic method should be efficient enough to indicate that.

In Tanzmeistergraben 1 contrast between serpentinite/dunite, amphibolite, and gneiss was expected to be detectable in the magnetic data because amphibolite and serpentinite hold stronger magnetic properties.

For Tanzmeistergraben 2 location aim is similar to Tanzmeistergraben 1. In the magnetic data, boundaries between amphibolite, granite, plagioklas gneiss, and serpentinite/ dunite were likely to be detectable.

6.2.1 Magnetic data acquisition

The magnetic data were measured in gradient mode with GSM 19-T proton precession magnetometer in some cases parallel with GSM 19-OH (GEM-Systems), along the survey lines (Figure 6.3) with mainly N-S and NW-SE direction. Magnetometers measured total magnetic field value at 0.5 or 1.0 (T1) and 1.5 or 2.0 (T2) m height but stored only T1 and the gradient value for storage capacity. In total 2302 magnetic data stations were measured. The data acquisition parameters are summarized in Table 6.2.

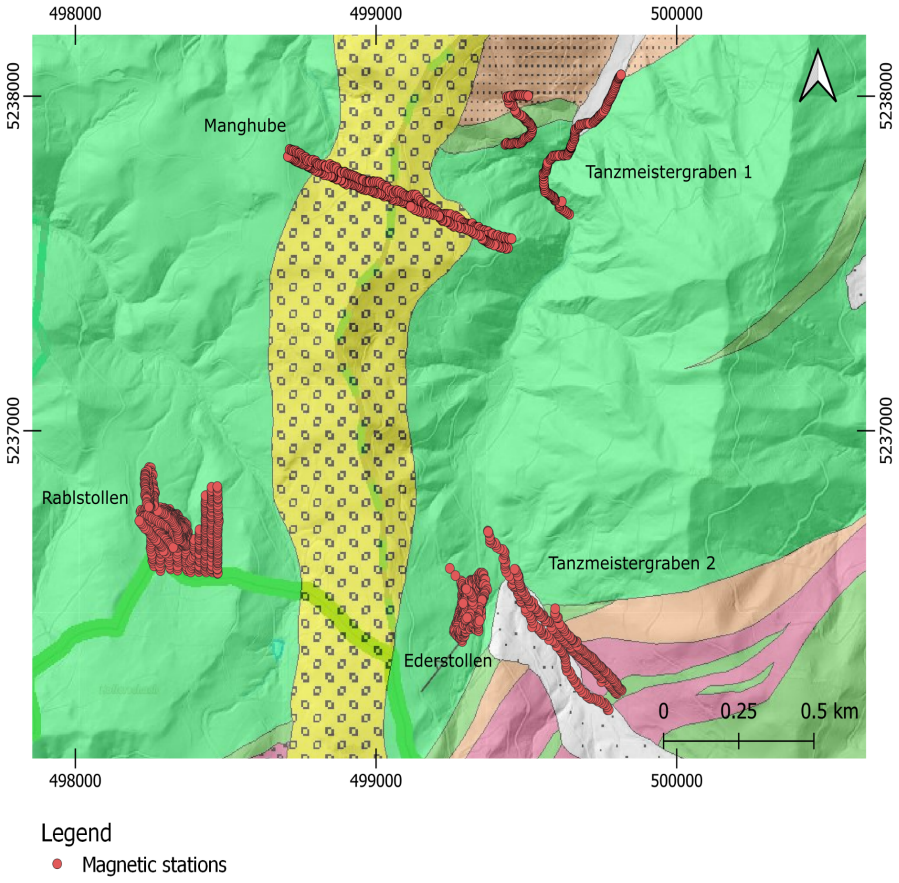

FIGURE 6.3: Magnetic data acquisition survey profiles. Used coordinate system WGS 84 UTM zone 33N.

TABLE 6.2: Magnetic survey parameters.

Location	Date	Survey equipment	Resolution Sensitivity Absolute Accuracy	Sample rates (m)	Navigation	Lowe (T1) and upper (T2) sensor height (m)	Recorded data points	Type of measurement (nT)	Number of survey lines, strike
Manghube	26.04.2016	GSM 19-T	0.01 nT 0.15 nT at 1 Hz 0.2 nT	1	Trimble GPS	0.5, 1.5	268	Total magnetic field	2 (NW-SE)
Rablstollen	15.03.2016 24.03.2017 04.03.2017	GSM 19-T	0.01 nT 0.15 nT at 1 Hz 0.2 nT	5	Trimble GPS	1.0, 2.0	1103	Total magnetic field	10 (N-S) 15 (NW-SE)
Tanzmeistergraben 1	03.05.2018	GSM 19-T GSM 19-OH	0.01 nT 0.15 nT at 1 Hz 0.2 nT	5	Garmin GPSmap 64s Garmin eTrex 10	1.0, 2.0	227	Total magnetic field	2 (N-S)
Tanzmeistergraben 2	08.05.2018	GSM 19-T GSM 19-OH	0.01 nT 0.15 nT at 1 Hz 0.2 nT	5	Garmin GPS	1.0, 2.0	278	Total magnetic field	3 (NW-SE)
Ederstollen	15.04.2021 27.04.2021	GSM 19-T GSM 19-OH	0.01 nT 0.15 nT at 1 Hz 0.2 nT	1	Garmin GPS	1.0, 2.0	426	Total magnetic field	10 (N-S)

In order to constrain magnetic modelling, the magnetic susceptibility (k) measurements were taken using an Exploranium KT9 Kappameter with a penetration depth of 3 to 5 cm. To achieve representative magnetic susceptibility values for each lithology, at least 7 measurements were made for the same lithology (Table 6.3).

TABLE 6.3: Mean value of magnetic susceptibility measurements performed on each lithology in the study area.

Lithologies	Sampling number	Susceptibility k (SI $x10^{-3}$)
Laterite	9	29
Serpentinite	7	55
Sand, gravel	7	0

6.2.2 Magnetic data processing and modelling

The diurnal correction was performed to account for temporal variation in the geomagnetic field due to solar activity. The base station readings were used to correct for temporal variation in Ederstollen, Tanzmeistergraben 1 and Tanzmeistergraben 2 areas. Unfortunately, at the rest of the locations, another magnetometer as a base station was not used due to technical reasons. Consequently, it was decided to acquire data from the nearest magnetic observatory – Conrad (*Central Institution for Meteorology and Geodynamics* n.d.), and carry out diurnal correction based on them. In this research area, it is fairly acceptable because the measured magnetic field varies by hundreds of nT, secondly, by checking each measurement's time, solar activity was low and varied by a few tens of nT. Observatory plots for each magnetic acquisition field work day are given in Appendix B (*Magnetic data observatory plots* n.d.).

The total field strength of the IGRF 12 model was calculated for every data point in five locations, using each point – latitude, longitude, elevation, and date. Calculated IGRF 12 values were subtracted from the magnetic field intensity.

Due to the fact that magnetic data are irregularly spaced and it requires several assumptions, e.g. that the effect of remanent magnetisation is neglected, reduction to the pole was not performed. In addition, further 3-D modeling software requires the "real" anomaly values, and not pole-reduced values, for the inversion.

After magnetic data reductions, 3-D modelling was continued in Potent v4.17.01 software for Rablstollen and Ederstollen locations, where reduced anomaly of the total magnetic intensity together with spatial information was used. In the rest of the locations, where only two to three profiles were made, data are represented in a form of scatter plots.

Rablstollen

Before starting 3-D modelling in Potent v4.17.01 magnetic data and topographic grids were interpolated by increasing data density with help of Golden Software

Surfer 22 program. Kriging interpolation was applied with a search radius of 30 m with 1 m spacing in the x and y directions. This interpolation method is widely used in geophysical surveys, especially in the magnetic survey, and has proven to be successful (Ruiqing and Jin, 2012). Both grids after enhancement were merged and afterward imported into Potent software.

Based on the geological information gathered in the field, ERT results, topographic and susceptibility data, forward and inversion magnetic modelling were performed along with eleven profiles (location in Figure 8.17) simultaneously. Inversion was based on the non-linear least squares method. Four profiles were located in the same location as ERT profiles, and seven profiles were oriented in the N-S direction and were distributed evenly. Using eleven profiles allowed for strengthening the overall geometries and distribution of laterite bodies and bedrock.

The main aim of the 3-D model was to show laterite distribution and underlying bedrock - serpentinite depth and surface topography. The starting model was generated based on the ERT and borehole data, using the idea of laterite being close to the surface between sedimentary rocks and underlying serpentinite. Prism geometry was used in the modelling of the bodies. In the model two types of bodies were incorporated, the first body type was baafterwardse laterite characteristics, and the second one was serpentinite. Sedimentary rocks were not part of the model, since they do not have any or are characterized by small magnetic susceptibility.

By constraining magnetic susceptibility, and remanence magnetization (leaving zero), the rest of the parameters such as the dip, surface location, strike, and size were allowed to vary.

Ederstollen

The same processing steps were applied as for the Rablstollen area. In the Golden Software Surfer 22 program, magnetic and topographic grids were interpolated. Kriging interpolation was applied with a search radius of 15 m with 1 m spacing in x and y directions. Both enhanced grids were imported in the Potent v4.17.01 software, where further magnetic 3-D modelling was conducted.

In the Potent v4.17.01 software across the Ederstollen area, six profiles were constructed, located in the same position as the ERT profiles. Four profiles were oriented N-S direction, one profile in W-E, and the last profile NW-SE direction. Only the length of all six profiles was extended to cover a larger area. Based on information from those six profiles, a 3-D model was created.

6.3 Electromagnetic method

Ground electric conductivity measurements were conducted in Rablstollen and Ederstollen areas. By conducting EM measurements, the main target was to identify laterite body geometry and distribution. Delineation of boundaries between laterite and the host rocks – serpentinite and dunite, due to their different electrical conductivities, should be possible, and borders well identifiable.

6.3.1 EM data acquisition

In Rablstollen area, measurements were conducted in the years 2016 and 2017 (Figure 6.4). In 2016, a Geonics EM38 measurement device was used with a theoretical penetration depth of 0.75 m with horizontal dipole mode and 1.50 m with vertical dipole mode. Survey lines were oriented N-S and were approximately 200 m long, in one case 300 m. Distance between stations was 5 m, and span between survey profiles $\sim$ 20 m.

In 2017, the EM31 device was used, reaching greater theoretical penetration depth with horizontal dipole mode - 3.0 m, and 6.0 m depth with vertical dipole mode. Two profiles were acquired, one oriented NW-SE direction and 160 m long, and the other oriented NE-SW and 190 m in length. The distance between stations was 5 m.

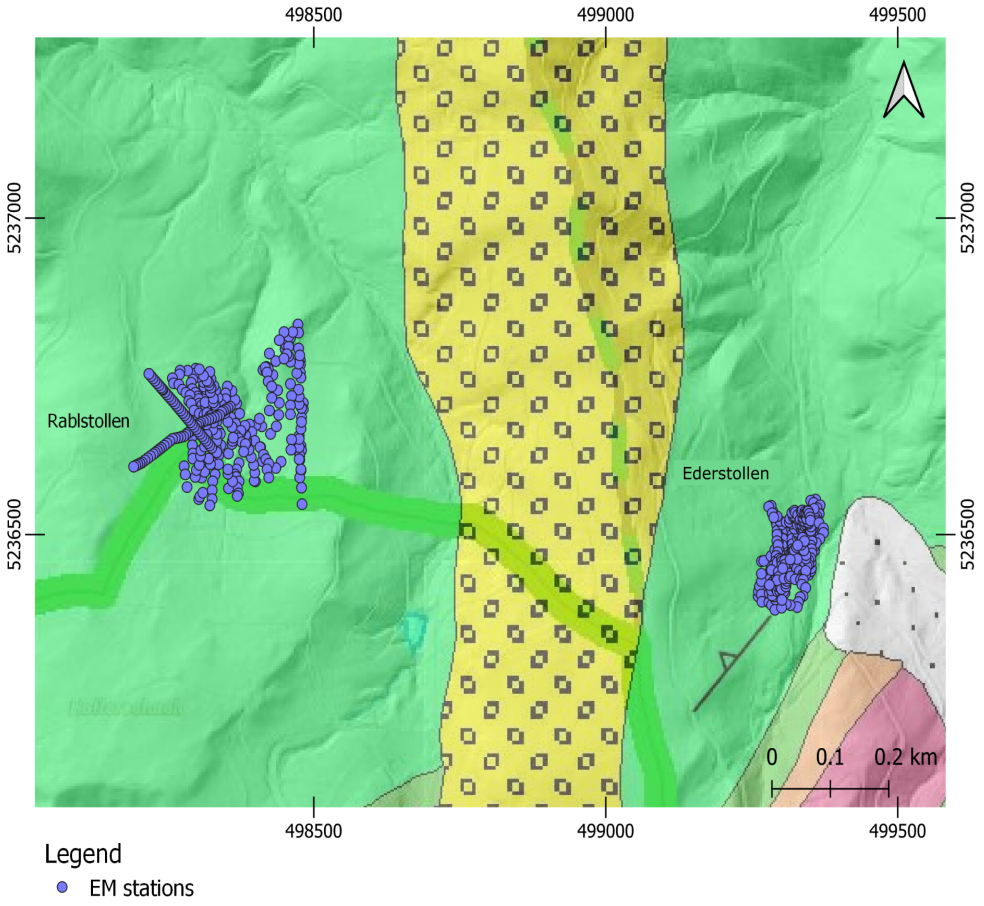

FIGURE 6.4: EM data acquisition survey profiles. Used coordinate system WGS 84 UTM zone 33N.

In Ederstollen measurements were made in the year 2021 with a Geonics EM38 measurement device with a penetrations depth of 1.5 m with vertical dipole mode. Survey lines were oriented N-S and were approximately 200 m long. The distance between stations was 5 m, and the span between survey profiles $\sim$ 15 m. The data acquisition parameters are summarized in Table 6.4.

TABLE 6.4: Electromagnetic survey parameters.

Location	Date	Survey equipment	Operating frequency (KHz)	Effective penetration depth (m)	Spacing between T(x) and R(x) (m)	Sample rates (m)	Navigation	Recorded data points	Type of measurement (mS/m)	Number of survey lines
Rablstollen	15.03.2016	Geonics EM38	14.5	0.75/ 1.5	3.66	5	Trimble GPS	150/398	Apparent conductivity	10
	24.03.2017	EM31	9.8	3.0/ 6.0				148/148		1
	13.04.2021									1
Ederstollen	15.04.2021	Geonics EM38	14.5	1.5	1.0	5	Trimble GPS	308	Apparent conductivity	10
	27.04.2021									

6.3.2 Electromagnetic data processing

For better data display, kriging interpolation in Golden Software Surfer 22 program was performed with a search radius of 20 m with 1 m spacing in the x and y directions. This sort of display was used only for data at 1.5 m depth due to a reasonably large quantity of data points in both investigation areas. For data points at 0.75, 3.0, and 6.0 m depth, simple colour coding was applied.

6.4 Self – Potential

The self-potential (SP) measurements were conducted in Rablstollen area for laterite detection. It is a high probability that with an SP method it would be possible to detect electronic conductors - laterite, in the form of a strong SP anomaly.

6.4.1 SP data acquisition

To measure self-potential, one pair of non-polarizing electrodes was used. Non-polarizing electrodes consist of a copper wire inside a CuSO4 fluid, and wood at the end of the electrode which is put in contact with the ground. A reference electrode is used as a fixed base and the second electrode is used to measure the electric potential at the ground surface. The difference in electrical potential between the base electrode and the moving electrode is measured with a voltmeter.

In the year 2016, survey lines were oriented N-S and were approximately 230 m long. Distance between stations was $\sim$ 10 m, and the span between survey profiles $\sim$ 10 m. In 2017, survey lines were oriented NW-SE, NE-SW, and the distance between the station $\sim$ 5 m (Figure 6.5). The data acquisition parameters are summarized in Table 6.5.

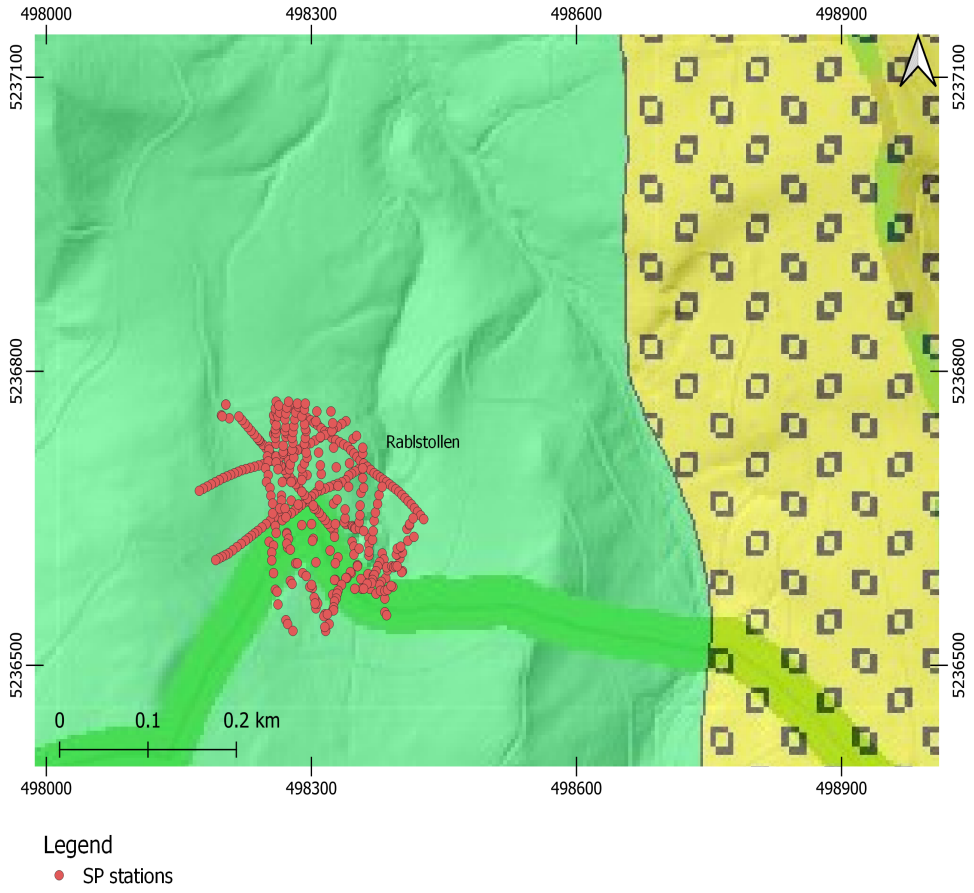

FIGURE 6.5: SP data acquisition survey profiles. Used coordinate system WGS 84 UTM zone 33N.

6.4.2 SP data processing

In this fieldwork, closed-loop profiling was performed where both the beginning and the end measurements were made at the same base station. Because of environmental noise (e.g. soil moisture, soil temperature, instrumental error, etc.), the measurement conditions can change, and drift may be observed. With drift correction, the raw data were corrected for this drift.

For better data display, kriging interpolation in the Golden Software Surfer 22 program was performed with a search radius of 25 m with 1 m spacing in the x and y directions.

TABLE 6.5: Self – potential survey parameters.

Location	Date	Survey equipment	Resolution (mV)	Sample rates (m)	Navigation	Recorded data points	Type of measurement (mV)	Number of survey lines, length (m)
Rablstollen	15.03.2016	Voltmeter	0.1	10	Trimble GPS	258	Potential difference	7, ∼ 230
	31.03.2017	Two non-polarizing electrodes		5		154		4, ∼180

7 ELECTRICAL RESISTIVITY TOMOGRAPHY DATA QUALITY ASSESSMENT

Data quality assessment is part of the ERT data processing, and a relevant step to determine the reliability of the acquired data. It is common practice to eliminate data outliers prior to inversion. Outliers could result from high geometric factor, which affects the signal-to-noise ratio, high contact resistivity, and insufficient current injection (Day-Lewis et al., 2007).

Data measurement error ($dU\%$) is the standard deviation of successive measurements during the data acquisition. The minimum and the maximum number of successive measurements and accuracy limits are set prior to the investigation. In the cases of Manghube, Rablstollen, and Ederstollen, the accuracy limit was set to 2%, minimum successive measurements to 2, and maximum to 5, after which measurement at the defined point will stop, even if the accuracy limit is not respected.

Measurement error, $dU\%$, is represented in the form of a Box-Whisker plot (Figure 7.1) for each ERT profile. The data quality is very good for all profiles and in most cases, error values are not crossing $dU\%$ threshold value of 2%, except for the Manghube profile and Ederstollen profile 6. However, before plotting Manghube profile $dU\%$ values, the data was despiked from negative and zero resistivity values since the used instrument (AGI Sting, used only for this profile) was saving blank resistivity values with abnormal dU values 100 – 200%. In Manghuben total of 1027 measurement points were recorded, 176 values were deleted (92 due to negative resistivity, 84 because of zero resistivity values/abnormal dU value). The mean error value for all profiles is in the range of 0.05 – 0.40%. The standard deviation is between 0.08 and 1.05%, which confirms the high quality of the data. The median is between 0.03 and 0.1%.

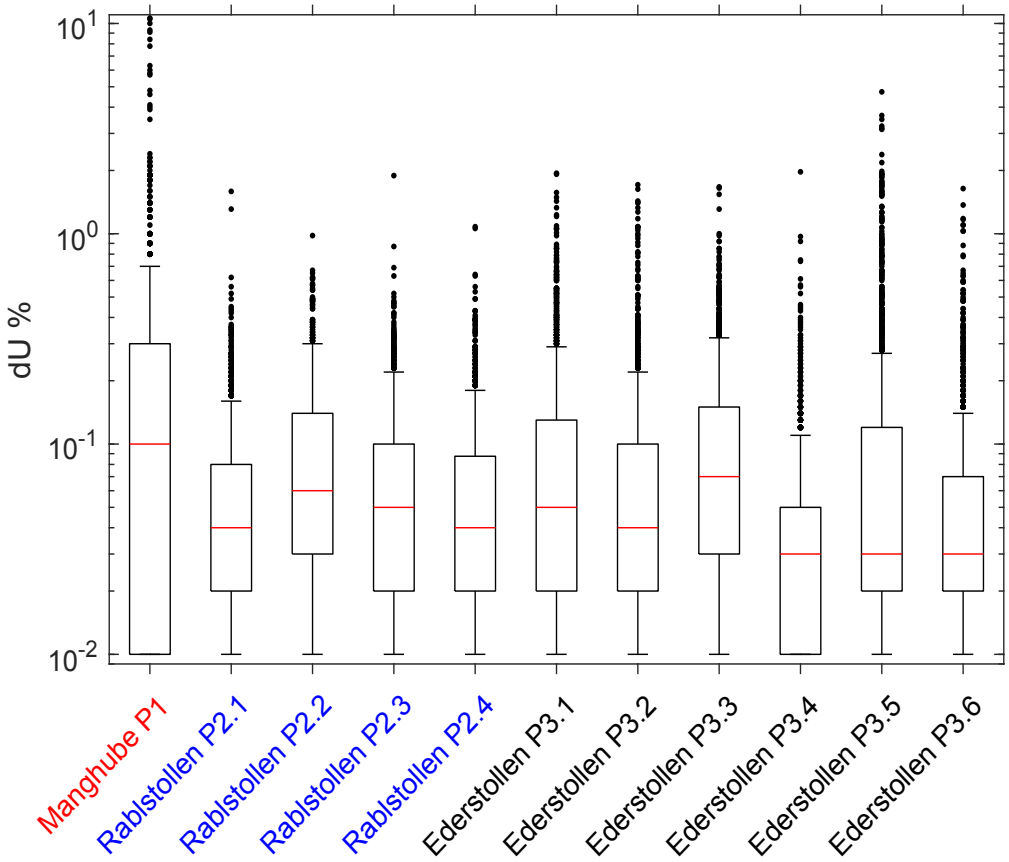

FIGURE 7.1: Box-Whisker plot of the measurement error *dU*% for each profile located at Manghube, Rablstollen, and Ederstollen. The red solid lines in the box plots represent the median value. Error bars correspond to the 95% confidence interval, the top and the bottom of the boxes are the 25th and 75th percentiles. Any outliers are shown as black dots.

All profiles resistivity values were also statistically assessed and represented in the form of a Box-Whisker plot (Figure 7.2). The mean resistivity values for Rablstollen and Ederstollen profiles are in the range between 47.49 and 86.24 Ωm, but for Manghube profile the value is 5541.47 Ωm. The standard deviation is between 18.07 and 50.75 Ωm, for Manghube the value is 81972.89. The median is between 39.25 and 79.25 Ωm, but for Manghube the value is 121.06 Ωm.

No negative resistivity values were encountered in the data sets for Rablstollen and Ederstollen profiles, but for Manghube 92 negative resistivity values were deleted, as mentioned previously. Manghube profile stands out with 42 outliers, but for the rest of the profiles, outliers are around the upper whisker fence limit.

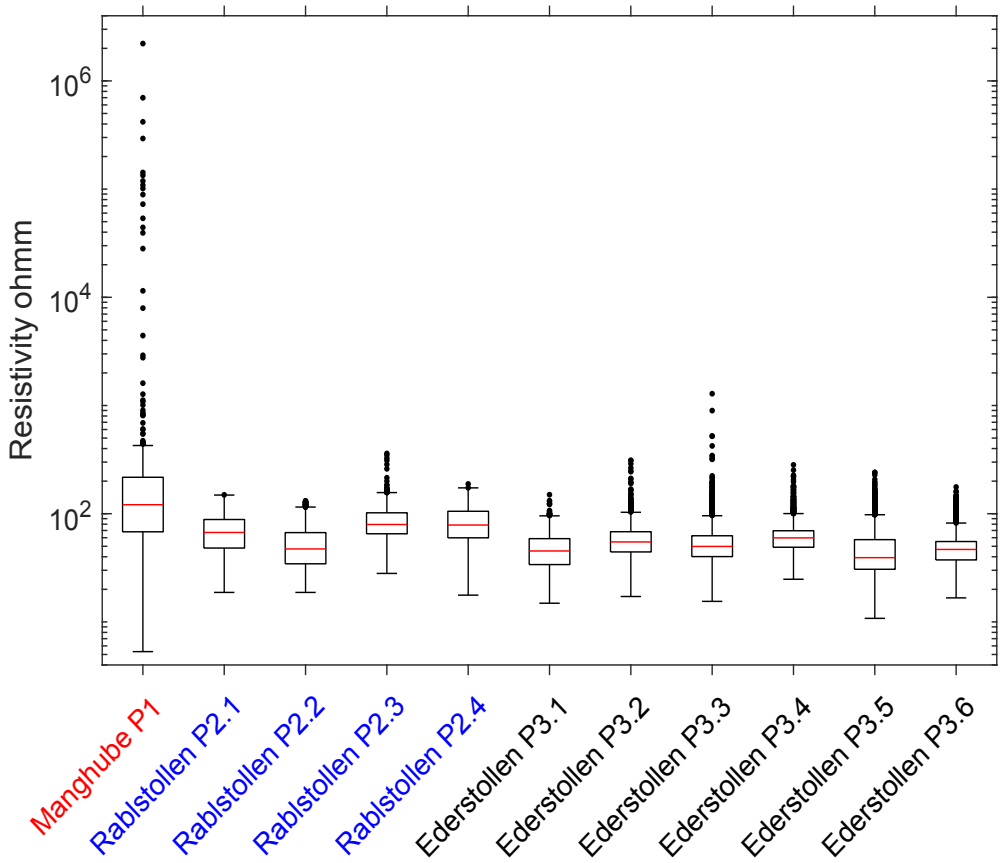

FIGURE 7.2: Box-Whisker plot of the resistivity for each profile located at Manghube, Rablstollen, and Ederstollen. The red solid lines in the box plots represent the median value. Error bars are the 95% confidence interval, and the bottom and top of the box are the 25th and 75th percentiles. Any outliers are shown as a black dot.

The Wenner alpha array was used in all profiles except for Ederstollen profiles 3.4, 3.5, and 3.6 where the dipole-dipole array was applied. In theory, the Wenner alpha array compared with the dipole-dipole array has a better depth resolution, higher signal strength, and is less sensitive to acquisition noise, and it requires fewer measurement points for the same line coverage than the dipole-dipole array. The dipole-dipole array has better lateral resolution and depth coverage at the ends of the lines (Neyamadpour et al., 2010). A possible disadvantage of the dipole-dipole array is the very small signal strength for large values of the "n" factor (Loke, 2001).

In the ERT data quality assessment regarding $dU\%$ and resistivity values, both arrays performed well except for Manghube profile where instrument complication caused some inconsistent data and spiked values.

8 RESULTS AND INTERPRETATION

8.1 Electrical Resistivity Tomography

In the results chapter, only inverted resistivity sections obtained by the inversion process using RES2DINV program are shown. The observed and calculated apparent resistivity profiles are given in Appendix A. The Wenner alpha array was used in all profiles except for the Ederstollen profiles 3.4, 3.5, and 3.6 where the dipole-dipole array was applied.

8.1.1 Manghube

In Manghube profile (Figure 8.1) it is possible to differentiate between sedimentary rocks and bedrock - serpentinite or dunite. Side boundaries on the right and left are clearly visible since sedimentary rocks yield low resistivity starting from 10 Ωm to 160 Ωm, but serpentinite and dunite have higher resistivity, starting from 160 Ωm. Exploration depth was approximately 140 m and, unfortunately, not enough to see how deep the sedimentary rocks stretch into bedrock.

Sediments which fill up this negative relief form, possibly, a fault zone, in the bedrock are heterogenic. There are two larger low resistivity zones (∼15 Ωm), one in the middle between 320 and 500 m, and a second one on the right side of the profile between 580 and 640 m. Between sediments there are at least two high resistivity zones (∼160 Ωm to 250 Ωm) above the low resistivity area, one between 400 and 520 m with a small break in the middle, and another one between 580 and 660 m.

These low and high resistivity areas could have arisen from the water saturation degree in the sediments or different sediment types. Most probably, both factors work together in this case.

Further interpretations than sedimentary and bedrock boundary identification and distinguishing different resistivity zones in sedimentary rocks should not be made due to the low quality of the data set and a large amount of data point reduction.

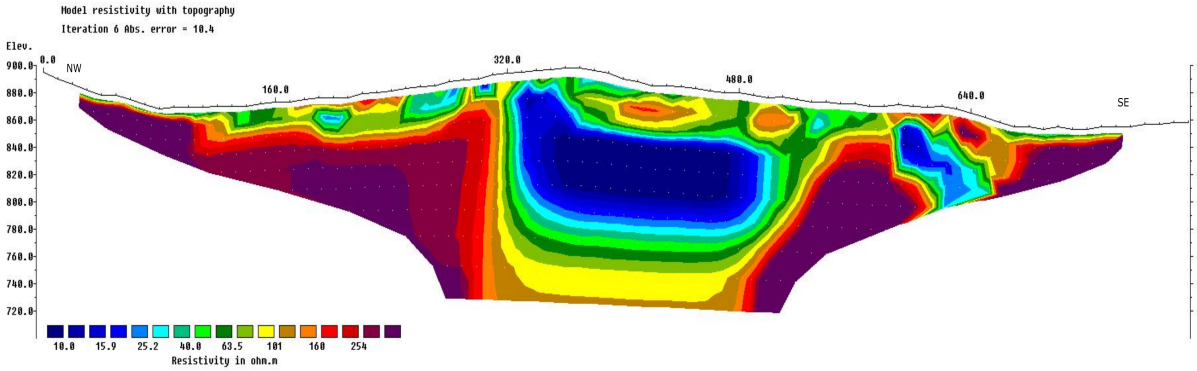

FIGURE 8.1: ERT inverted resistivity section of Manghube profile 1. Used electrode spacing 10 m.

8.1.2 Rablstollen

In the 2017 fieldwork at Rablstollen, the investigation was focused on laterite identification and distribution recognition. 2-D inversion model sections show the presence of different resistivity zones and geological layering. In all four profiles, it is possible to identify low resistivity bodies (10 to 20 Ωm) which are enclosed by sedimentary rocks (till 160 Ωm) and located above a high resistivity zone (160 Ωm to 320 Ωm)(Figure 8.6). Most probably these bodies are irregular, lense shaped, and do not spread throughout the investigation area. Based on the borehole data and observations during the field courses, low resistivity zones correspond to laterite.

In the Profile 2.1 (Figure 8.2) one low resistivity body - laterite, was observed. The body is located in the middle of the profile between 52 and 115 m and is found in the upper section of the profile near the surface, between 4 and 18 m in-depth, and is enclosed by sedimentary rocks (20 to 160 Ωm). Laterite and sedimentary rocks' lower boundary is sheared with a high resistivity bedrock - serpentinite or dunite, which is visible on the profile's bottom left and bottom right sides.

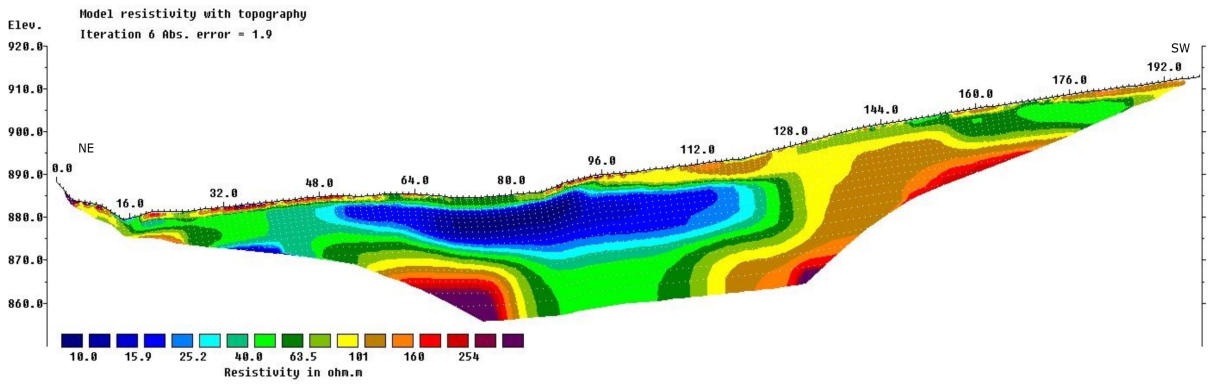

FIGURE 8.2: ERT inverted resistivity section of Rablstollen profile 2.1. Used electrode spacing 2 m.

Profiles 2.2 (Figure 8.3) S-E part cuts through a laterite body which is located in the middle of profile 2.1. At both profile intersection points, profile 2.2 also shows a low resistivity zone, between 130 and 153 m. The second laterite body from profile 2.2 is located between 26 and 72 m. Both laterite bodies are linked by slightly higher resistivity material, who could be interpreted as sedimentary rock. Bellow laterite high resistivity zone starts - serpentinite or dunite, about 15 m in depth.

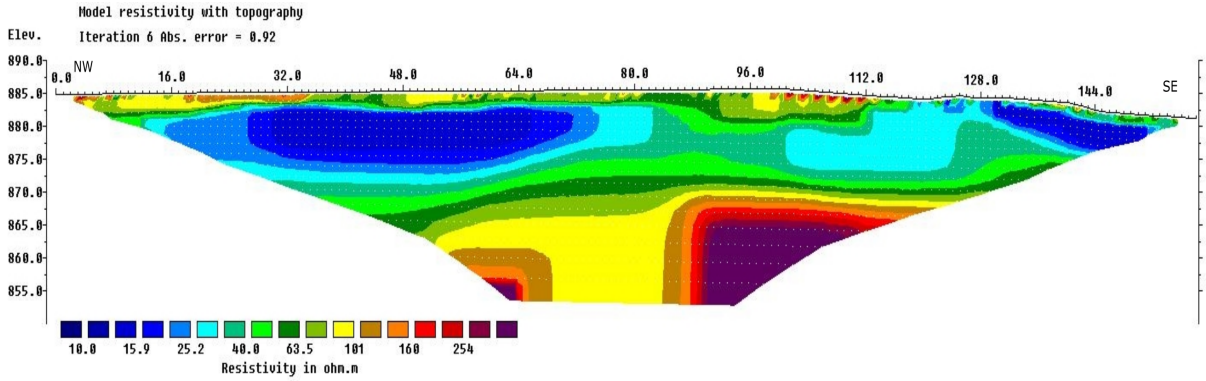

FIGURE 8.3: ERT inverted resistivity section of Rablstollen profile 2.2. Used electrode spacing 2 m.

Profile 2.3 (Figure 8.4) oriented NW-SE slightly touches profiles 2.1 and 2.4 north-east sides. In the middle of the profile, there is a low resistivity zone, possibly laterite. The resistivity for this zone is slightly higher (around 20 to 25 Ωm) than the typical laterite resistivity value observed in other ERT profiles. This low resistivity area is located close to the surface (a few dozen centimetres) and starts from 64 and stretches till 119 m with a slight break in the middle. Below the potential laterite body about 7 m in depth, an approximately 4 m wide transition zone between sedimentary rocks and bedrock starts.

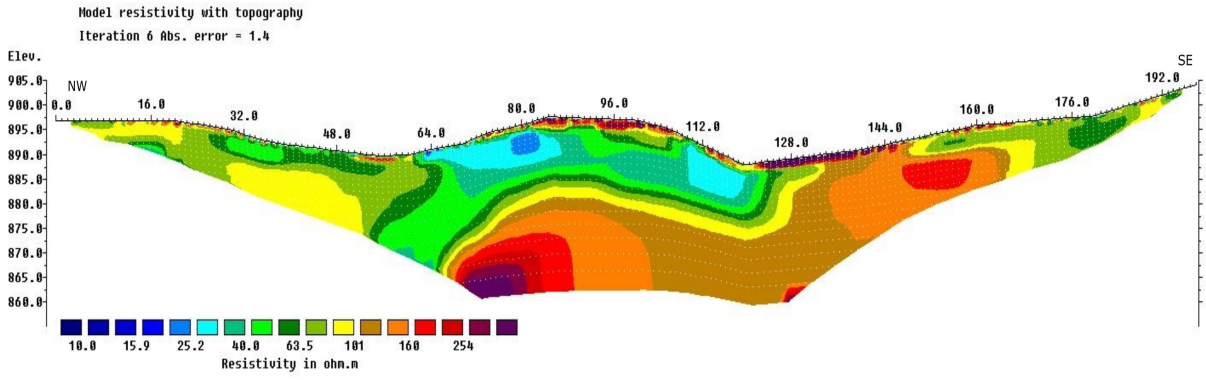

FIGURE 8.4: ERT inverted resistivity section of Rablstollen profile 2.3. Used electrode spacing 2 m.

Profile 2.4 (Figure 8.5) oriented NE-SW, striking parallelly with profile 2.1, cuts through profile 2.2 and slightly goes through profile 2.3. A low resistivity area near

the surface about 5 m thick is located between 97 and 117 m and corresponds to the laterite body found in profile 2.2 between 26 and 72 m. At the beginning of the NE side profile, a small conductive area is located between 4 and 20 m.

At the NE side, weathered bedrock starts approximately at 10 m depth with resistivity of approximately 100 Ωm. It is possible to follow it from 20 to 72 m where it ends abruptly, and lower resistivity area starts (till 80 Ωm) until 112 m. From 112 m till the end of the profile, a high resistivity area is located and stretches till surface. On the SW side of the profile, between 150 and 160 m, a high resistivity area is positioned at the surface and could be correlated with a forest road made of dry, sandy sediments.

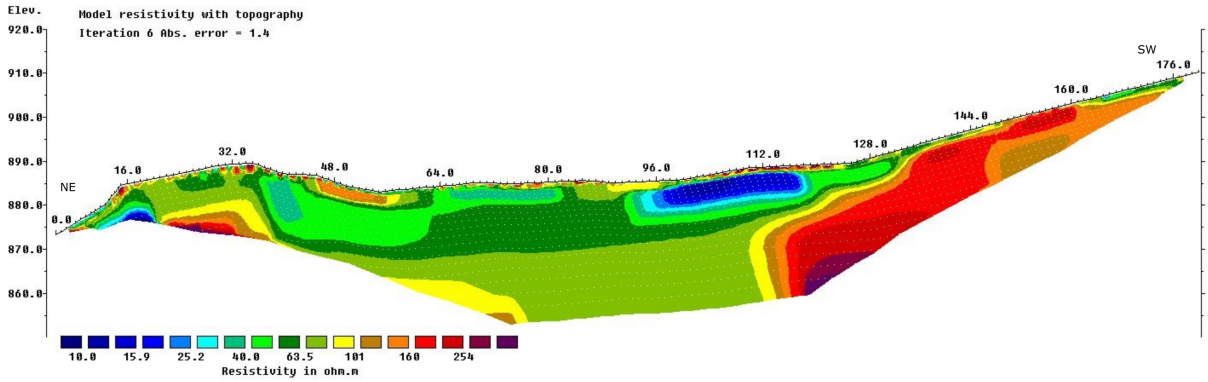

FIGURE 8.5: ERT inverted resistivity section of Rablstollen profile 2.4. Used electrode spacing 2 m.

To obtain a spatial impression of the ERT data, all four 2-D resistivity sections were imported into Paraview software (version 5.10.0, open source) where it is possible to view profiles together and see more accurately low resistivity zones distribution between all profiles (Figure 8.6). Two larger laterite bodies stand out, the first one on the intersection point between profiles 2.1 and 2.2, and the second one between profiles 2.4 and 2.2. Low resistivity distribution in 3-D remains and proves that there could be not one but many distinctive laterite bodies close to each other separated by sediments such as sand or gravel.

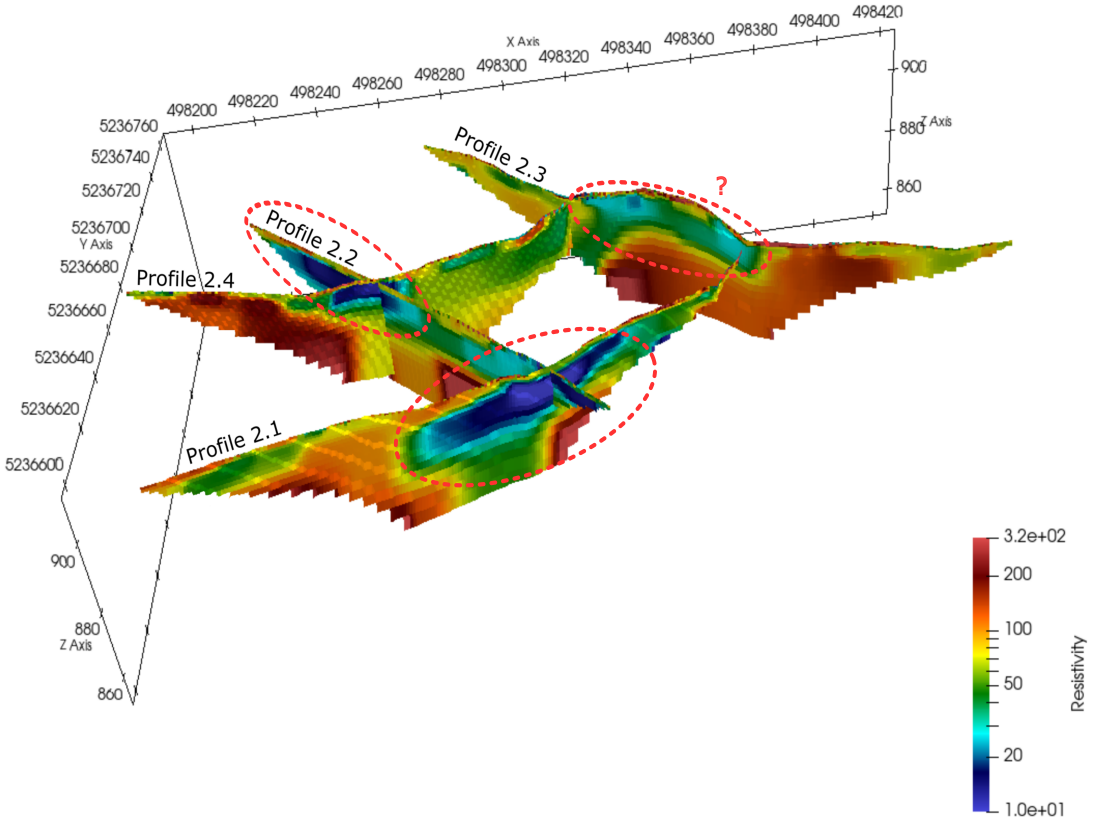

FIGURE 8.6: 2-D profiles of inverted ERT resistivity sections from Rablstollen viewed in 3-D space. Red dotted lines indicating possible laterite ore body location.

8.1.3 Ederstollen

In the years 2020 and 2021, field works in Ederstollen were carried out. Each year, three ERT profiles were made. In 2020 3.1, 3.2, 3.3, and in 2021 3.4, 3.5, 3.6. In the chosen grid, four profiles were made parallel to each other and two profiles crossed or slightly touched all four profiles going perpendicular or diagonally across. 2021 year profile geometry was based and customized on findings in the year 2020.

The aim for conducting ERT in this area was the same as for Rablstollen - to distinguish and map out low resistivity zones (10 to 20 Ωm) which correspond to laterite. In all profiles, low resistivity areas are visible as lense shaped, irregular, and located above bedrock between sedimentary rocks.

Profile 3.1 (Figure 8.7) oriented in the W-E direction was located perpendicular to profiles 3.3, 3.4, 3.5, 3.6. Starting at 8 till 53 m along the profile, a low resistivity zone is located. On the left side, this zone is embedded to 4 m depth and starts near the surface, but going closer to the middle of the profile low resistivity zone becomes thicker and is embedded deeper. The low resistivity zone appears irregular, and three separate laterite bodies (till 20 Ωm) enclosed by slightly higher resistivity (till 25 Ωm) sediments could be made out.

Along the profile between 20 and 22 m and 39 to 41 profile meters, laterite outcrops were observed in the field, which could correspond to a low resistivity zone at the surface.

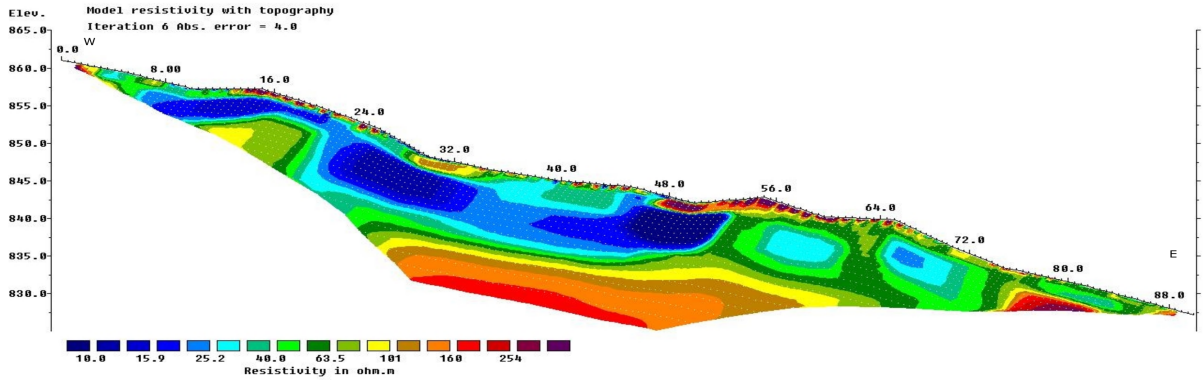

FIGURE 8.7: ERT inverted resistivity section of Ederstollen profile 3.1. Used electrode spacing 1 m.

Profile 3.2 (Figure 8.8) oriented NW-SE crosses profiles 3.1, 3.3, 3.4, 3.5. Closer to the SE profile side, a high resistivity zone (starting from 160 Ωm) at the surface is visible between 72 and 86 meters. This zone could be correlated with large boulders. As well, between 48 and 60 m high resistivity zone, 3 m thick, is visible at the surface. Just below the high resistivity zone, a low resistivity body (till 20 Ωm) is embedded with dimensions approximately 7 m in thickness and 24 m in length. More to the NW side, another low resistivity zone appears, less thicker than the first body, approximately 3 m and goes from 16 to 33 m. This zone is underlayn by a higher resistivity zone of bedrock. Both bodies are separated by slightly higher resistivity (40 - 50 Ωm) yielding sediments.

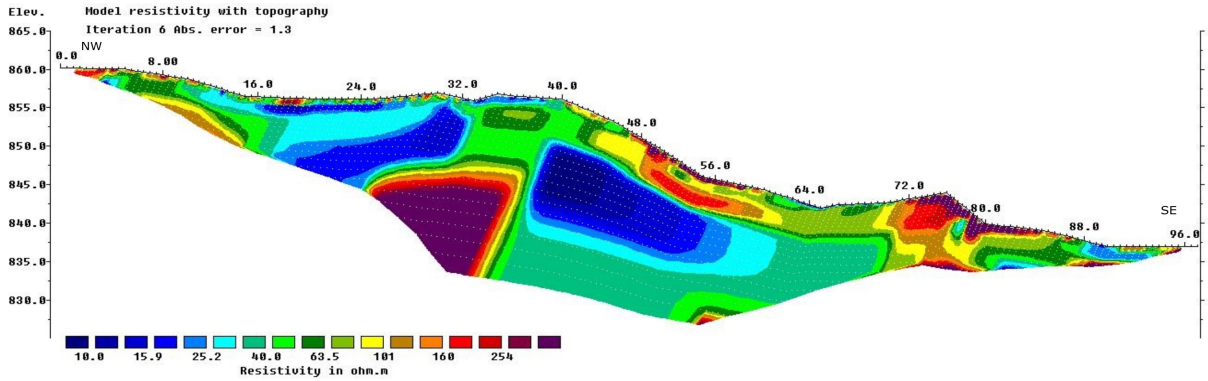

FIGURE 8.8: ERT inverted resistivity section of Ederstollen profile 3.2. Used electrode spacing 1 m.

Profile 3.3 (Figure 8.9) is oriented in the N-S and crossed by profiles 3.1 and 3.2. Three separate low resistivity zones (till 25 Ωm) are identifiable. One starts from 35 to 51 m, the second one from 54 to 58 m and the third one from 80 to 97 m. In

all three zones, smaller lower resistivity zones (10 to 20 Ωm) are visible. Above the second and the third low resistivity zone a high resistivity layer is visible which is approximately 3 m thick and could be resulting from the upper part of the profile consisting of dry sediment.

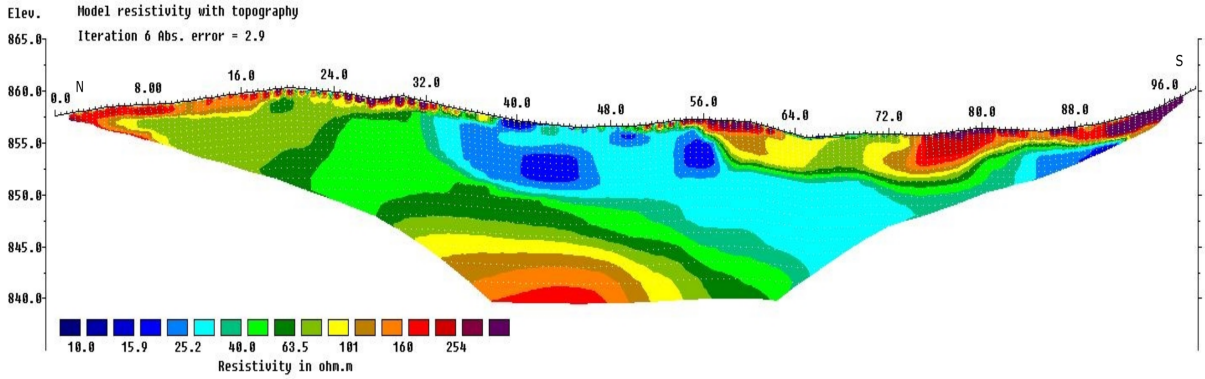

FIGURE 8.9: ERT inverted resistivity section of Ederstollen profile 3.3. Used electrode spacing 1 m.

Profile 3.4 (Figure 8.10) is oriented in the N-S direction and slightly touches profiles 3.1 and 3.2 beginnings. High surface resistivity is evident, which could be correlated with dry weather conditions. A low resistivity zone (till 20 Ωm) is visible in the middle of the profile between 60 and 72 m, embedded between higher resistivity sediments.

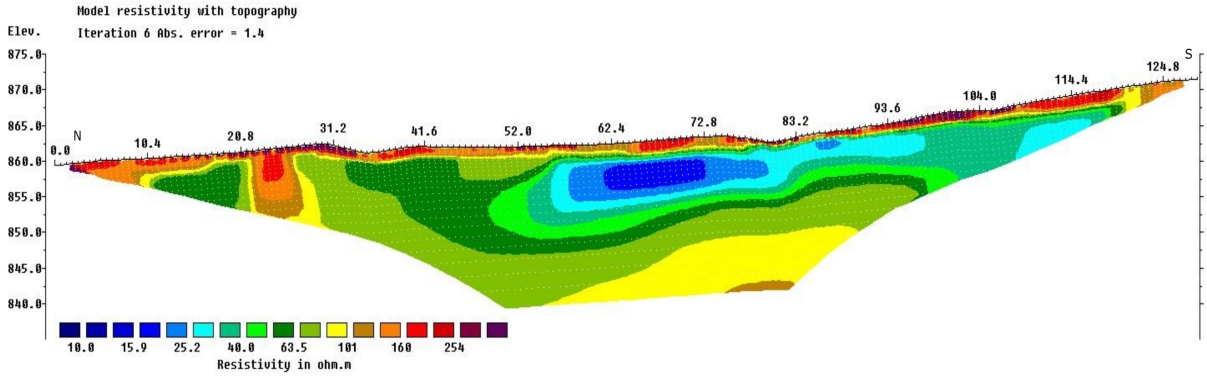

FIGURE 8.10: ERT inverted resistivity section of Ederstollen profile 3.4. Used electrode spacing 1.3 m.

Profile 3.5 (Figure 8.11) is oriented N-S direction and goes through 3.1 and 3.2 profiles. Quite large but irregular low resistivity zone stretches from 17 till 75 m overlaying higher resistivity zone - serpentinite or dunite. In the low resistivity zone, three potential laterite bodies (20 Ωm) are possible to identify - one between 18 till 54 m, the second one starting from 59 to 67 m, and the third one between 69 and 75 m. All three potential laterite bodies are located 5 m deep and stretch to 10 m

depth. The same as for profile 3.4 high surface resistivity is visible in the profile which could be explained also by weathered conditions on that day.

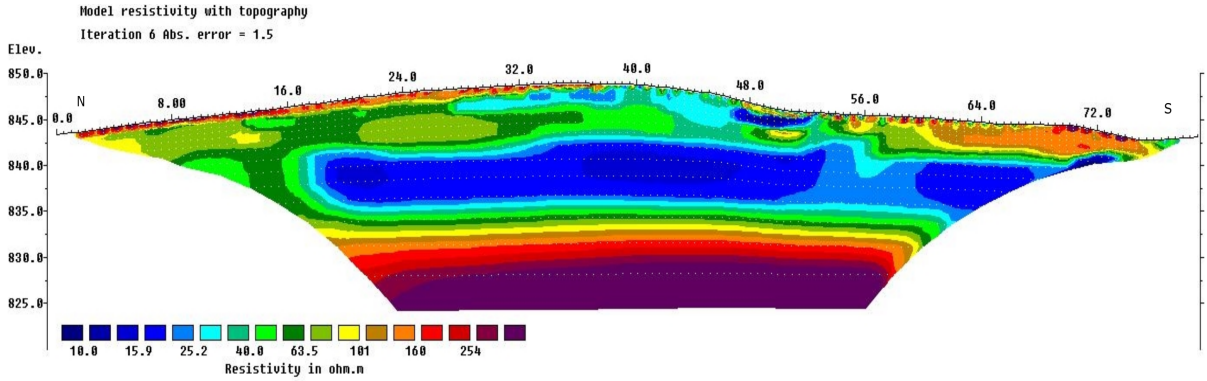

FIGURE 8.11: ERT inverted resistivity section of Ederstollen profile 3.5. Used electrode spacing 1 m.

Profile 3.6 (Figure 8.12) is oriented in the N-S direction and crossed by profile 3.1. A low resistivity zone (20 Ωm) is visible on the right side of the profile between 42 and 54 m. The second low resistivity zone is located between 30 and 37 m, but resistivity for this zone is slightly higher - 25 Ωm. Both zones are enclosed by sedimentary rocks that are overlaying the bedrock.

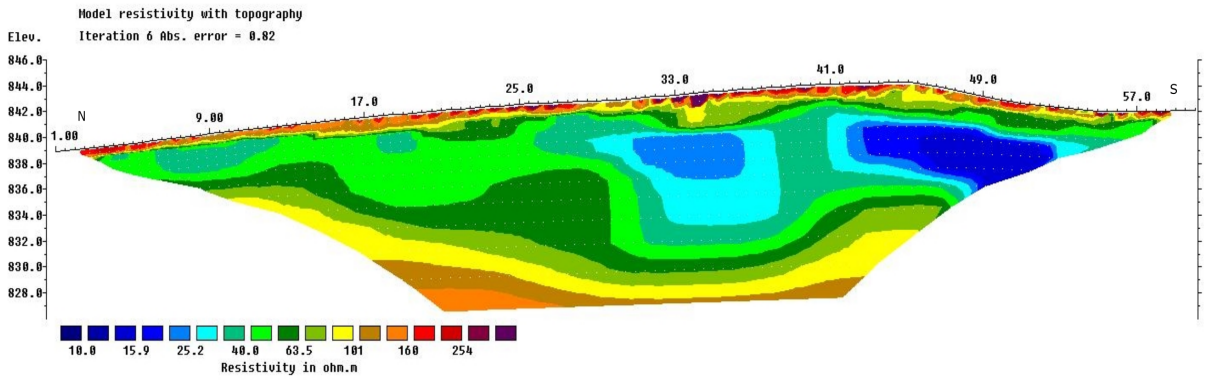

FIGURE 8.12: ERT inverted resistivity section of Ederstollen profile 3.6. Used electrode spacing 1 m.

The same as for Rablstollen, Ederstollen profiles were also viewed together in Paraview software (version 5.10.0, open source) for better spatial impression. The low resistivity zone (till 20 Ωm) in profile 3.1 correlates with profiles 3.2, 3.3, 3.4, 3.5, 3.6, and a potential laterite body is possible to trace between these profiles but most probably this body is irregular and consists of interruption and breaks filled by sedimentary rocks.

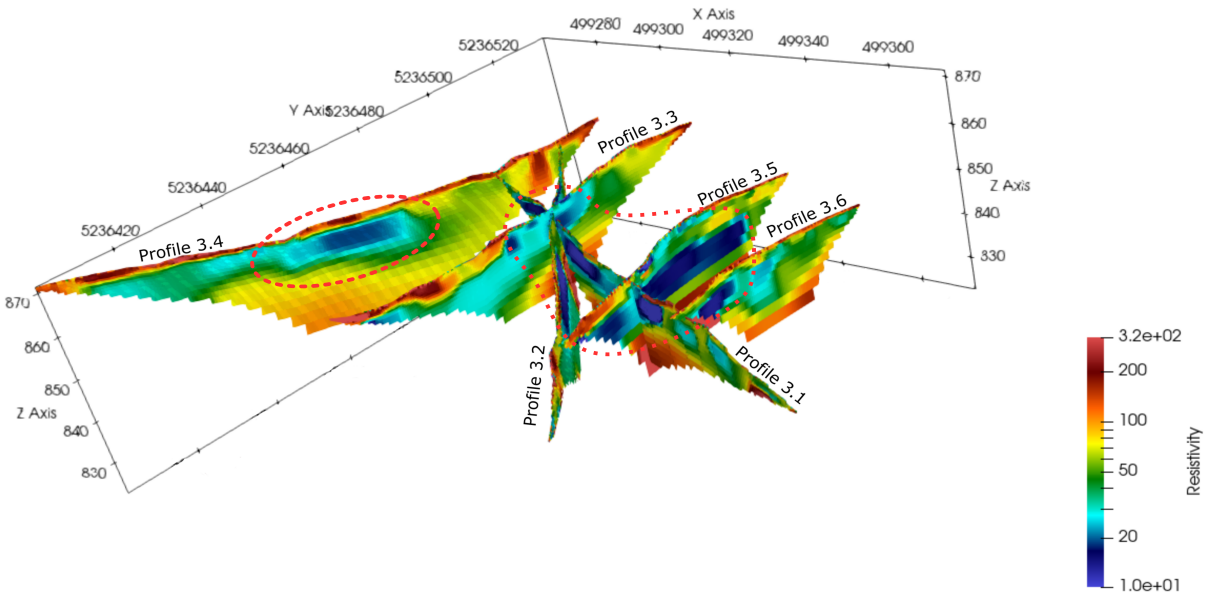

FIGURE 8.13: 2-D profiles of inverted ERT resistivity sections from Ederstollen viewed in 3-D space. Red dotted lines indicating possible laterite ore body location.

8.2 Magnetism

In Manghube, Tanzmeistergraben 1 and 2 the focus of the magnetic measurements was on the lithological boundaries identification and defining the typical range of physical parameters over different lithologies. As well for the Manghube, possible laterite bodies identification at the boundaries between sediment and underlying rocks. As for Rablstollen and Ederstollen, the depth and morphological boundaries of the laterite bodies were expected to be possible to delineate.

8.2.1 Manghube

The reduced anomaly of the total magnetic intensity for two profile lines from Manghube area is expressed in the form of a scatter plot (Figure 8.14). In the first 400 m, a steady trend of total field magnetic anomaly is observed (approximately -80 nT). Further along, the profile lines (SE direction) anomaly trend goes down to - 250 nT. This negative trend could be explained by a deep laying source in which the negative part of a dipole anomaly (with a long wavelength) is identifiable in both profiles - Lines 1 and 2. There are also several short wavelength dipoles near the surface and monopolar negative anomalies of a small extent (lightning strikes or remanent magnetisation).

Both profiles cut through bedrock and sedimentary rocks. A clear transition zone, which was expected between the two lithologies at the beginning and at the end of the profiles, is not identifiable. That could indicate that bedrock is composed of "non-magnetic" dunite on both sides in this location. In the data, there are no indications that laterite bodies could have been located in this area.

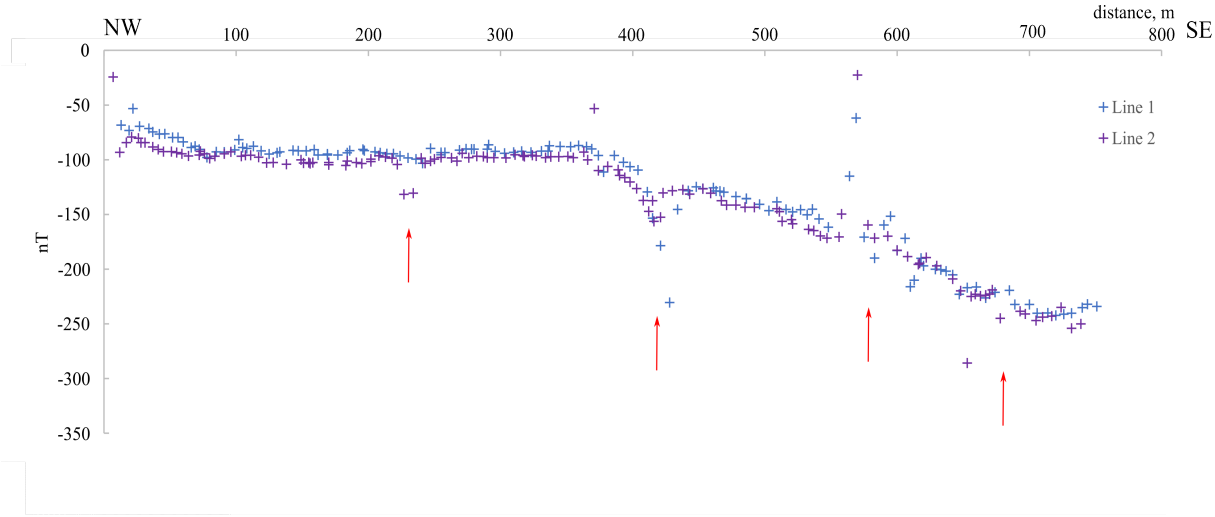

FIGURE 8.14: The reduced anomaly of the total magnetic intensity for Lines 1 and 2 from Manghube area. Red arrows are indicating the most distinguishable short wavelength dipoles near the surface and monopolar negative anomalies. The distance between both lines is approximately 20 m .

8.2.2 Tanzmeistergraben 1

The reduced anomaly of the total magnetic intensity for two profile lines from Tanzmeistergraben 1 area is expressed in the form of a scatter plot (Figure 8.15). Both lines cross three different geological units (from the south to the north) - serpentinite/dunite, amphibolite, and gneiss. At the beginning of both profile lines, a steady magnetic field is observed. In line 1 about 100 nT, but in line 2 - 200 nT. Close to the 100 profile meters, an increasing trend is visible at both lines with maximums of about 400 to 700 nT. A positive trend most probably marks the border between strongly magnetic serpentinite and paramagnetic amphibolite.

In both lines, a clear transition, in a form of a large wavelength anomaly, is visible between amphibolite and gneiss between the 230 m or 350 m mark, depending on the profile. For line 1 only part of the dipole is visible with a maximum of around 1000 nT, but for line 2, the dipole maximum is 500 nT, but the negative anomaly reaches -1570 nT.

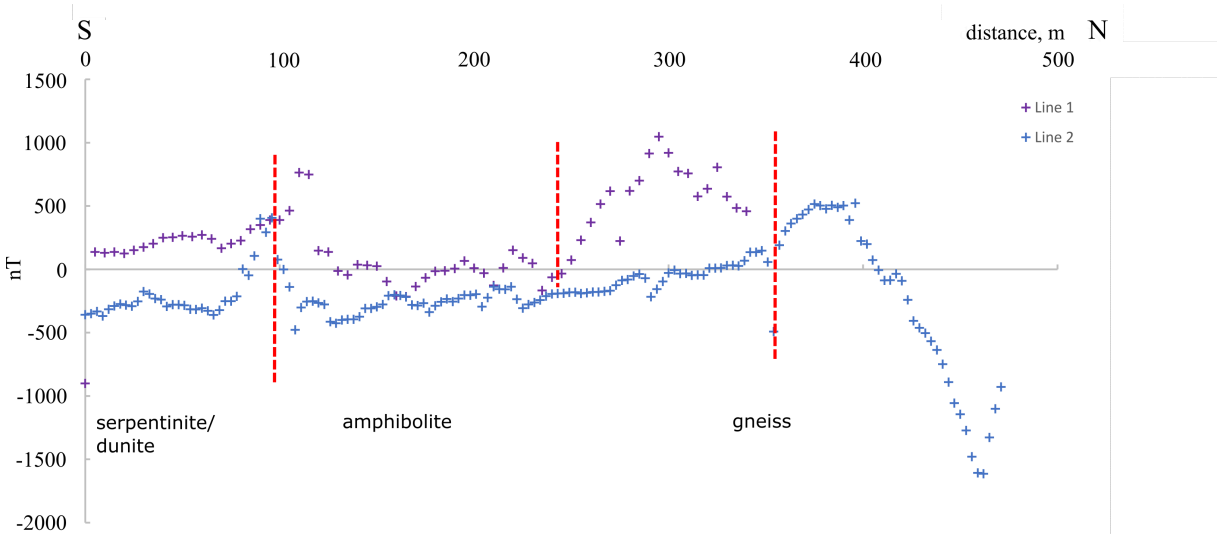

FIGURE 8.15: The reduced anomaly of the total magnetic intensity for Line 1 and 2 from Tanzmeistergraben 1 area. Red vertical lines indicate possible lithological borders.

8.2.3 Tanzmeistergraben 2

Three parallelly located profile lines reduced anomaly of the total magnetic intensity are expressed in the form of a scatter plot (Figure 8.16). All three profile lines cross five geological units (from the south to the north) - amphibolite, granite, gneiss, amphibolite and serpentinite/ dunite.

The boundary of each geological unit is well visible in the magnetic data. Amphibolite rock stretches to 70 profile meters with a reduced anomaly of around 0 nT. The border between amphibolite and granite is marked by a short wavelength, high amplitude dipole. Granite rock with a steady trend anomaly of about -180 nT goes to 190 m and the transition zone between granite and gneiss is highlighted by an upgoing positive trend. Gneiss and amphibolite lithological border shifts slightly in each of the profiles but approximately at 250 profile meters is the transition zone between both lithologies. Both lithologies have similar magnetic properties from around zero to a little bit less than 200 nT, depending on the profile. The most distinguishable lithological border is between amphibolite and serpentinite/ dunite which starts approximately at 330 profile meters and is marked by a long wavelength dipole whose maximum reaches a little over 500 nT while the negative anomaly reaches -400 nT.

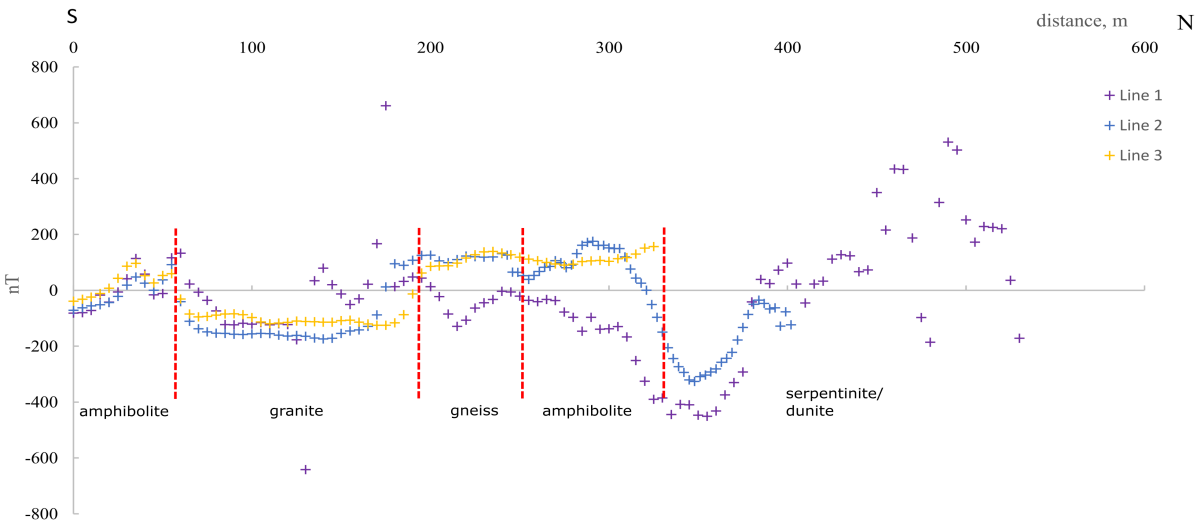

FIGURE 8.16: The reduced anomaly of the total magnetic intensity for Line 1, 2 and 3 from Tanzmeistergraben 2 area.

8.2.4 Rablstollen

The reduced anomaly of the total magnetic intensity for Rablstollen area is given in Figure 8.17. The Kriging interpolation method was used to obtain a contour map. The scale of magnetic field intensity values ranges from -500 to 1000 nT. The highest negative values (-500 to -100 nT) stretch from south to northwest, forming a belt-like form. The NW features are oriented along the NW- SE direction, while the negative anomalous structures in the south and the middle of the mapped area are mainly oriented in the NS direction. The location of these negative values matches with a small forest road that goes through the investigation area.

The highest values of the total magnetic intensity (700 to 1000 nT) cover a small amount of the area. The largest positive anomaly maxima are located in the SW part oriented in the NE-SW direction and could be correlated with an adjacent negative anomaly with the same orientation.

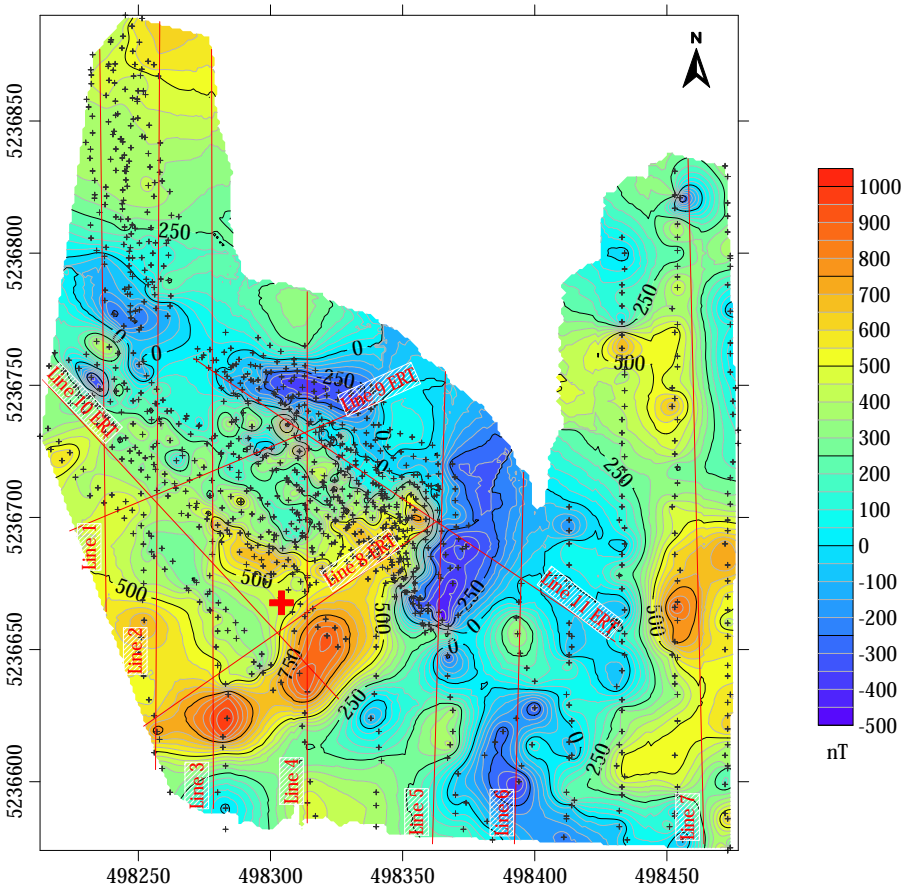

FIGURE 8.17: The reduced anomaly of the total magnetic intensity for Rablstollen area together with 3-D magnetic modeling lines. The borehole location is shown as a red cross. Black crosses represent measured data points.

In total, eleven profiles (Figure 8.18) were designed in Potent v4.17.01 software across the area where magnetic measurements were taken. Seven oriented N-S directions and four profiles following along SW-NE and NW-SE directions. Short wavelength anomalies were tried to describe with laterite bodies which are relatively small and close to the surface but longer wavelength anomalies with larger and deeper embedded bodies of serpentinite. Prism geometry was applied in the modelling of the bodies. The first body type was based on the laterite and the second one was on serpentinite characteristics. The susceptibility value for laterite ore bodies was set at 0.029 SI and for serpentinite bodies 0.055 SI.

For modeling the first seven profiles, nearby ERT data were taken into the account, but because ERT does not cover entirely the investigation region, some parts of the area are fully modeled based on magnetic data alone. From profile 1 to profile 7 laterite bodies are present and deeper below serpentinite is located. Serpentinite depth varies for each profile between 20 to 40 m, the surface of the serpentinite is

irregular and variable in each location. Laterite bodies on average are 20 m in length and 10 m thick, located near the surface from 0 to 5 m in depth.

Profile 8 is in the same location as ERT profile 2.1, profile 9 corresponds to ERT profile 2.4., profile 10 to ERT profile 2.2, and profile 11 to ERT profile 2.3. Comparing profile 8 and ERT profile 2.1. (Figure 8.2) location of laterite and serpentinite matches in both profiles where laterite appears in the middle of the profile and further stretches to the NE direction and below it, serpentinite is embedded. Laterite body thickness in both profiles is around 10 m.

Comparing results between Profile 9 and ERT profile 2.4. (Figure 8.5) locations of laterite bodies in both profiles are similar, one on the NE side (body No. 7) and the other one more to the SW side (body No. 24) of the profile. Laterite body No. 27 according to ERT data is closer to the surface than the magnetic profile shows. Serpentinite (body No. 27) in magnetic data appears to come close to the surface at one point in the profile - in the middle, but ERT data shows that the high resistivity zone is more to the SW side.

According to magnetic profile 10, laterite is occurring almost constantly in the upper part of the section, two large (length about 40 m) and one smaller body were modeled. Body No. 24 and No. 11 match in location and length with ERT profile 2.2. (Figure 8.3) existing low resistivity zones. Body No. 10 in the ERT profile is represented as a transition zone between both low resistivity areas. Serpentinite is well visible in the ERT profile below laterite and the same situation is in the magnetic data.

Profile 11 shows one laterite body No. 7 starting in the middle of the profile and stretching to the NW side. In the ERT profile 2.3. (Figure 8.4) this zone is low resistivity but not fully convincing that laterite ore could be there, but magnetic data shows a possible ore body. In the SE part of the magnetic profile another ore body No. 4 is located which is not visible in the ERT data.

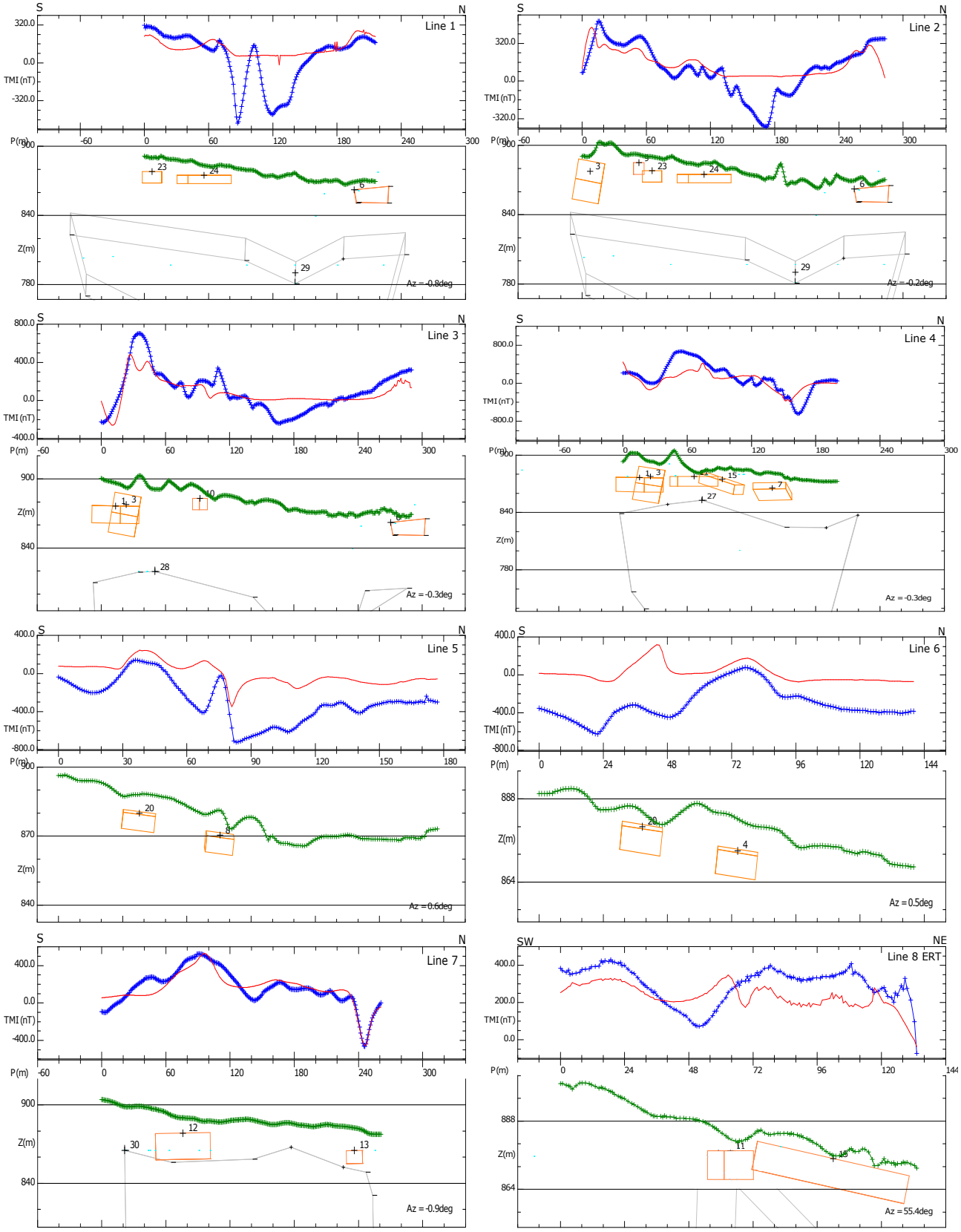
Line 1
Line 2
Line 3
Line 4
Line 5
Line 6
Line 7
Line 8 ERT
TMI (nT)
P(m)
Z(m)
Az = -0.8deg
Az = -0.2deg
Az = -0.3deg
Az = -0.3deg
Az = 0.6deg
Az = 0.5deg
Az = -0.9deg
Az = 55.4deg

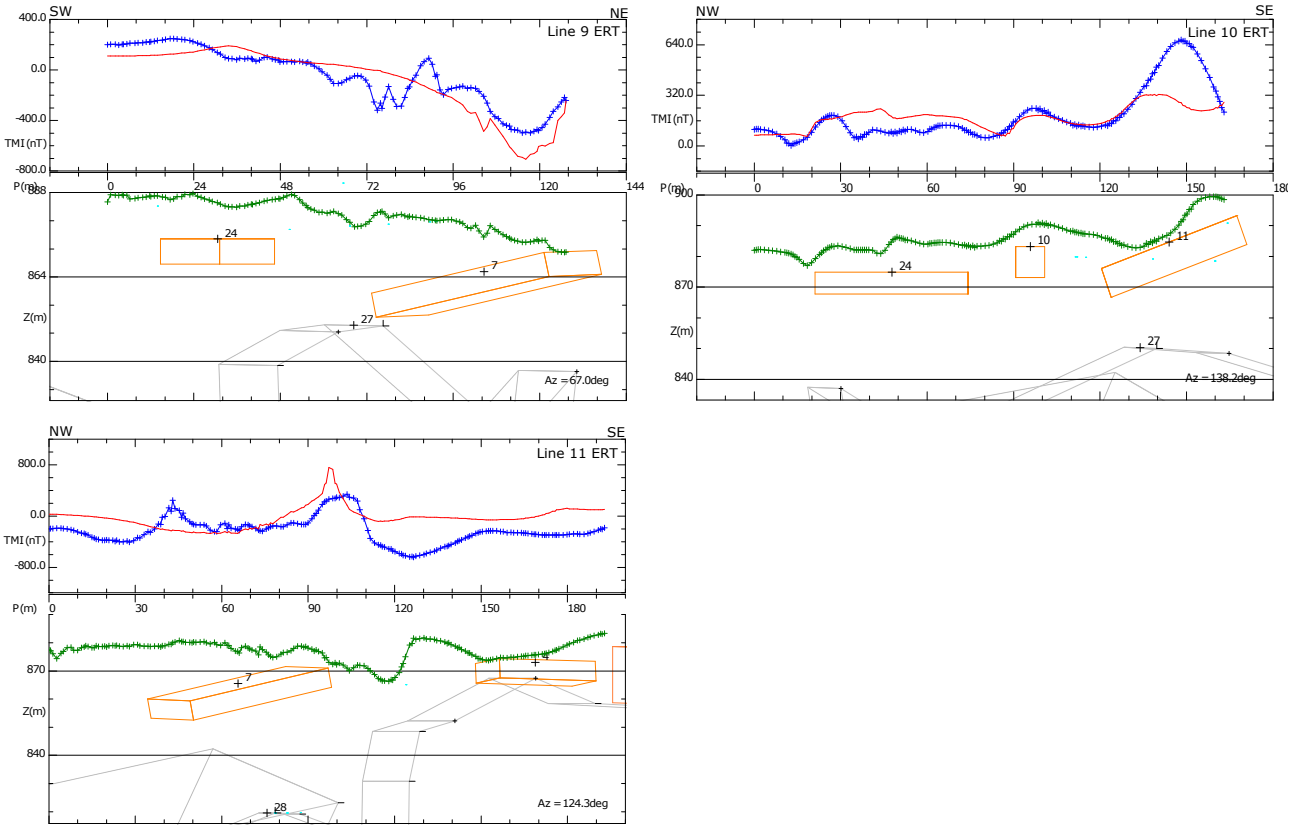

FIGURE 8.18: Comparison between measured and modelled anomalies along eleven profile lines (location 8.19) in the Rablstollen area. Blue line: measured reduced anomaly of the total magnetic intensity (nT), red line: calculated reduced anomaly of the total magnetic intensity (nT), green line: topography. Each of the modeled bodies has a unique number for clear identification. Used susceptibility values for orange (laterite) bodies 0.029 SI, for grey colour (serpentinite) bodies 0.055 SI.

Based on eleven profiles (Figure 8.18) 3-D model for Rablstollen area was created. The model (Figure 8.19) shows irregularly distributed laterite bodies throughout the investigation area located in the upper part of the geological section near the surface, closely followed by the serpentinite layer below. As ERT and borehole data indicated laterite ores are incorporated between sedimentary rocks, however, this type of lithology was not taken into account in the model-making due to low to zero susceptibility values.

The bedrock surface which mainly consists of serpentinite is uneven and reflects topography. On the west side of the model, bedrock is closer to the surface, and going more to the east tends to dip deeper. At the location where profiles 5 and 6 are placed, bedrock goes deeper than 50 m and comes closer to the surface approximately 30 m on the east side where profile 7 is located.

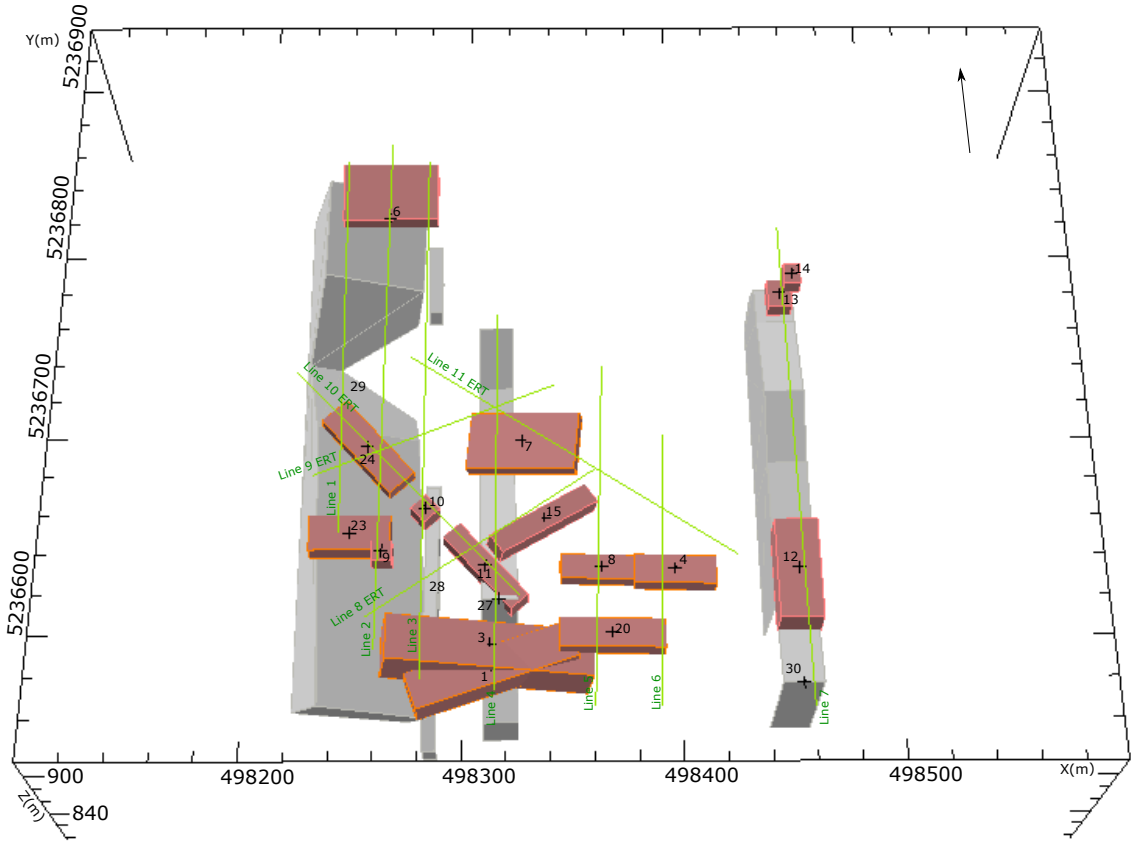

FIGURE 8.19: Magnetic data 3-D model for Rablstollen area. Used susceptibility values for orange (laterite) bodies 0.029 SI, for grey colour (serpentinite) bodies 0.055 SI. Each profile number and location is displayed in green colour.

8.2.5 Ederstollen

The reduced anomaly of the total magnetic intensity for Ederstollen area is given in Figure 8.20. The Kriging interpolation method was used to obtain a contour map. The scale of magnetic field intensity ranges from -900 to 1100 nT and is roughly divided into two separate areas. The first area is located in the map's west and south, consisting of magnetic values above 300 nT. The second area covers a larger part of the survey and is associated with magnetic values below 300 nT.

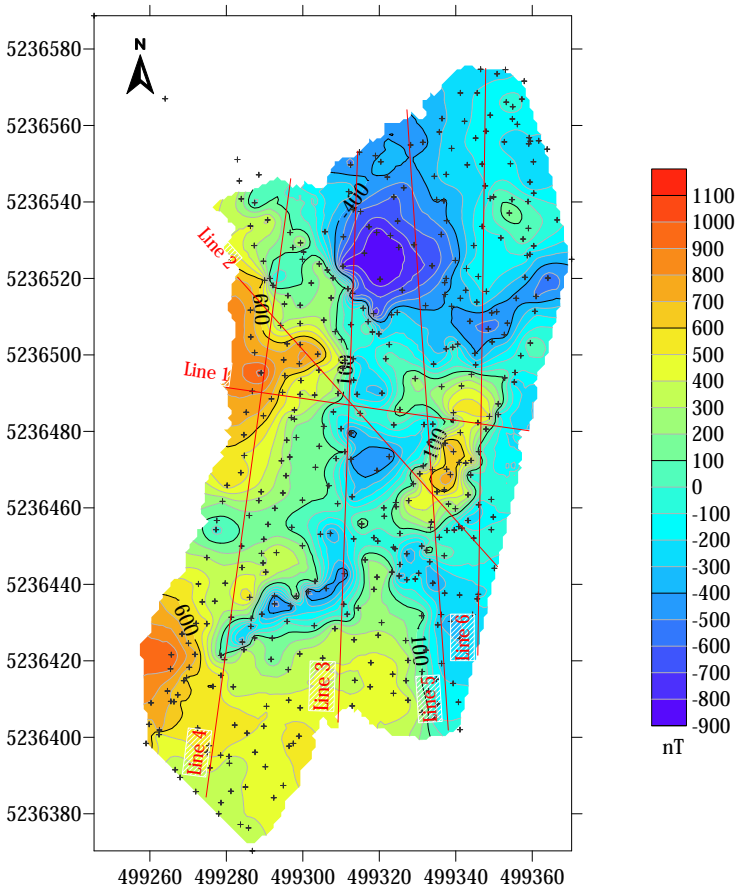

FIGURE 8.20: The reduced anomaly of the total magnetic intensity for Ederstollen area together with 3-D magnetic modeling lines. Black crosses represent measured data points.

3-D modeling was based on six profiles (Figure 8.21) constructed in Potent v4.17.01 software. Four profiles were oriented N-S, one W-E, and the last one along the NW-SE direction. All six profile locations are the same as for the ERT profiles, the only difference is that magnetic profile lines were made longer to cover a larger investigation area.

Profile 1 is in the same location as ERT profile 3.1, profile 2 corresponds to ERT profile 3.2, profile 3 to ERT profile 3.3, profile 4 to ERT profile 3.4, profile 5 to ERT profile 3.5, and profile 6 to ERT profile 3.6.

In magnetic profile 1 on the west side, three laterite bodies are located, 0 to 8 m from the surface and 3 to 10 m thick. In the ERT data (Figure 8.7) the low resistivity zone is also visible in the same position, but its depth from the surface is not larger than 3 m and the thickness in the widest part is a little over 5 m. Serpentinite is embedded right below the laterite.

In profile 2 laterite is located starting from the NW and stretching to the SE side. Laterite bodies No. 7 and 10 could be related to the low resistivity zone at the beginning of the ERT profile 3.2 (Figure 8.8) and body No. 1 to the low resistivity zone in the middle of the ERT profile. The depth of the laterite varies between 0 and 3 m. Serpentinite is embedded right below the ore bodies 10 to 20 m in depth.

For profile 3 ERT shows (Figure 8.9) a noticeable 24 m long, irregular with few interruptions low resistivity body in the middle of the profile but in the magnetic data, it does not appear. Only at the begging and the end of the magnetic profile, two laterite bodies are revealed, about 15 to 20 m long. ERT data partly covers the location of body No. 9 but nothing indicates in the ERT profile existence of the ore body due to the low penetration depth at the side of the profile. Only at the south part small low resistivity area is visible which could be part of the laterite body No. 1 which is close to the profile line. Ore body No. 8 is not covered by ERT data.

Profile 4 shows three different sizes of ore bodies. The largest of the bodies, No. 7 is well visible in the ERT data, but it is much larger in the magnetic data than the ERT shows (Figure 8.10). In the magnetic model body No. 7 is 60 m long and 20 m wide but in the ERT data only approximately 12 m long and 5 m wide. The rest of the two bodies (No. 6 and 5) are not visible in the ERT data. Bodies No. 6 and 7 are embedded close to the surface within 1 m depth, but body No. 5 goes much deeper, approximately 15 m.

Profile 5 consists of two modeled ore bodies that are located above serpentinite. Both bodies are 20 m long and located 1 to 10 m from the surface close to each other. In the ERT profile 3.5 (Figure 8.11) one large, irregular, 56 m long, 5 m deep low resistivity zone is possible to identify. Ore body No. 11 and 1 are part of this irregular low resistivity zone and reaches its length. Magnetic data confirms that the existing low resistivity zone is made of more than one ore body.

In profile 6 one ore body is modeled from the magnetic data and below it, serpentinite starts. This ore body is 15 m long, 10 m wide, and close to the surface. ERT profile 3.6 (Figure 8.12) also indicated a low resistivity zone in almost the same position, but a little more to the north. The dimensions of the ore body in the magnetic and ERT data are almost the same.

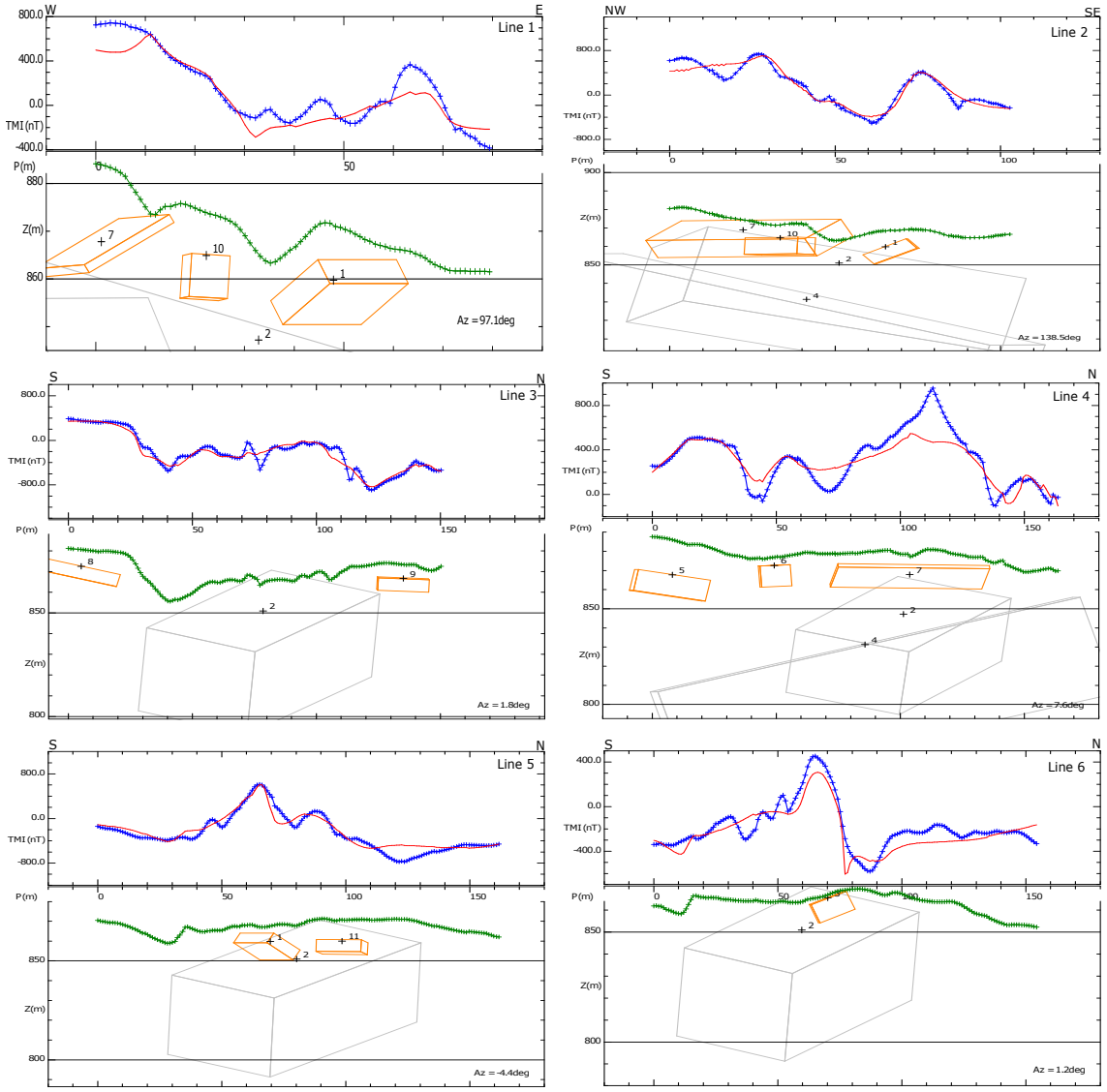

FIGURE 8.21: Comparison between measured and modeled anomalies along six profile lines (location 8.20) in the Ederstollen area. Blue line: measured reduced anomaly of the total magnetic intensity (nT), red line: calculated reduced anomaly of the total magnetic intensity (nT), green line: topography. Each of the modeled bodies has a unique number for clear identification. Used susceptibility values for orange (laterite) bodies 0.029 SI, for grey colour (serpentinite) bodies 0.055 SI.

Based on six profiles (Figure 8.21) a 3-D model for Ederstollen area was created. The 3-D model (Figure 8.22) same as for the Rablstollen area shows irregularly distributed laterite bodies throughout the area located in the upper part of the geological section near the surface, closely followed by the serpentinite layer. Laterite bodies are in different sizes. The largest one (body No. 7) is located on the west side and in dimensions reaches 60 m in length and 20 m in width, the smallest body (No. 6) lies near the body No. 7 but more to the south side and is 10 m long and 10 m wide. In this case, as ERT data indicates laterite ores are interbedded between

sedimentary rocks, however, sediment lithology was not taken into account during modeling process.

The bedrock surface which mainly consists of serpentinite is uneven and reflects topography. On the west side of the model, bedrock is closer to the surface, and going more to the east tends to dip deeper. In the north, the bedrock surface goes deeper than 50 m and is not visible in the model.

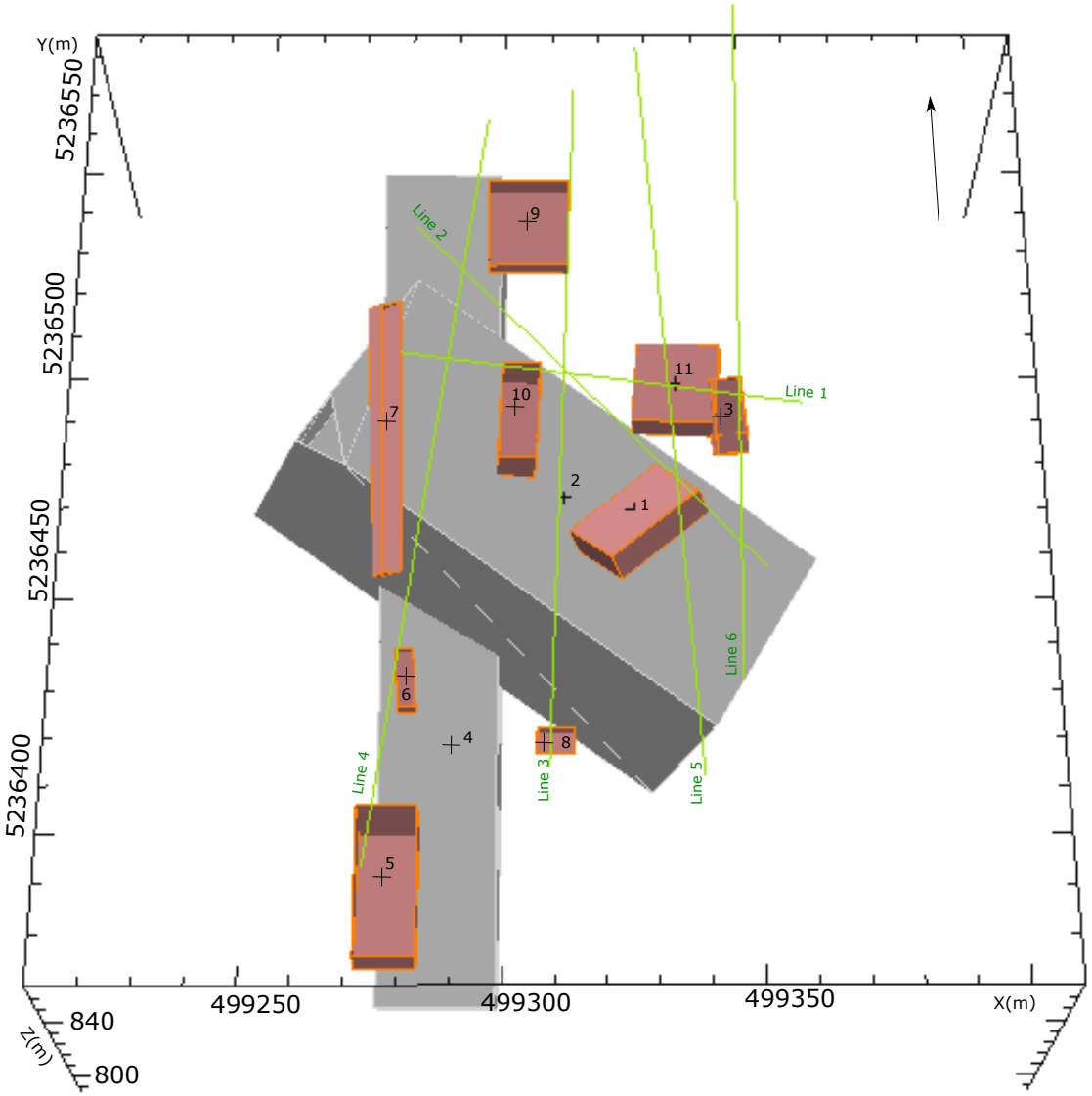

FIGURE 8.22: Magnetic data 3-D model for Ederstollen area. Used susceptibility values for orange (laterite) bodies 0.029 SI, for grey colour (serpentinite) bodies 0.055 SI. Each profile number and location is displayed in green colour.

8.3 Electromagnetic method

8.3.1 Rablstollen

The conductivity map of Rablstollen area at a depth of 1.5 m is shown in figure 8.23. Additionally, ERT profile lines were added to the map for better positional understanding. Overall, the map looks uniform without large conductivity variations at depth of 1.5 m. Conductivity values vary between -4 and 56 mS/m. Negative readings are produced if the instrument is directly above a conductor. Larger conductivity values than 26 ms/m are concentrated at the NW - part of profile line 2.2 and the NE - part along profile line 2.1. All negative readings are scattered and do not form any pronounced conductor. An overall large percentage of the acquired data is just above the noise level and larger conductivity anomaly zones are made of one to few data points which is not enough.

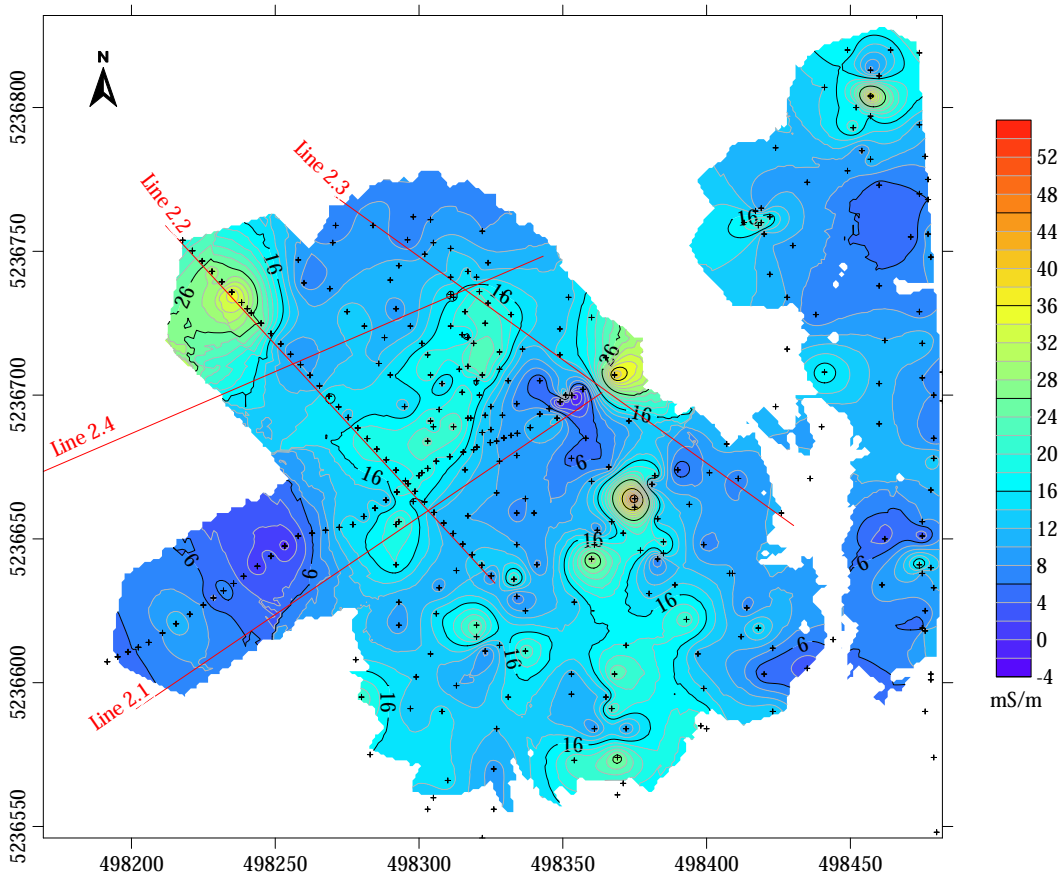

FIGURE 8.23: Conductivity map of Rablstollen area at depth of 1.5 m. Red lines indicate ERT profile line location.

In the figure 8.24 conductivity values at different depths along two profiles are shown. One profile goes along ERT line 2.2 and magnetic line 10, the second along

ERT line 2.1 and magnetic line 8. The first conductivity values from 0.75 m depth does not show large value variations. Values are ranging from 0.0 to 30.0 mS/m. Higher conductivity values are concentrated on the NW side along line 2.2. and as well on the SW side in profile 2.1. At the profile intersection point also higher values than 20 mS/m are located. At a depth of 3.0 m, more prominent conductivity anomalies are visible. At the intersection between two lines, values till 50 mS/m are observed, the same goes for the NW side of line 2.2. At the SW side of line 2.1 susceptibility values remained the same, around 15 mS/m. At the largest investigation depth — 6 m, the same anomaly zones have become more distinguishable, values go up to 60 mS/m. At the same positions (the NW side of line 2.2 and the intersection between both lines) ERT and magnetic data indicated possible ore bodies.

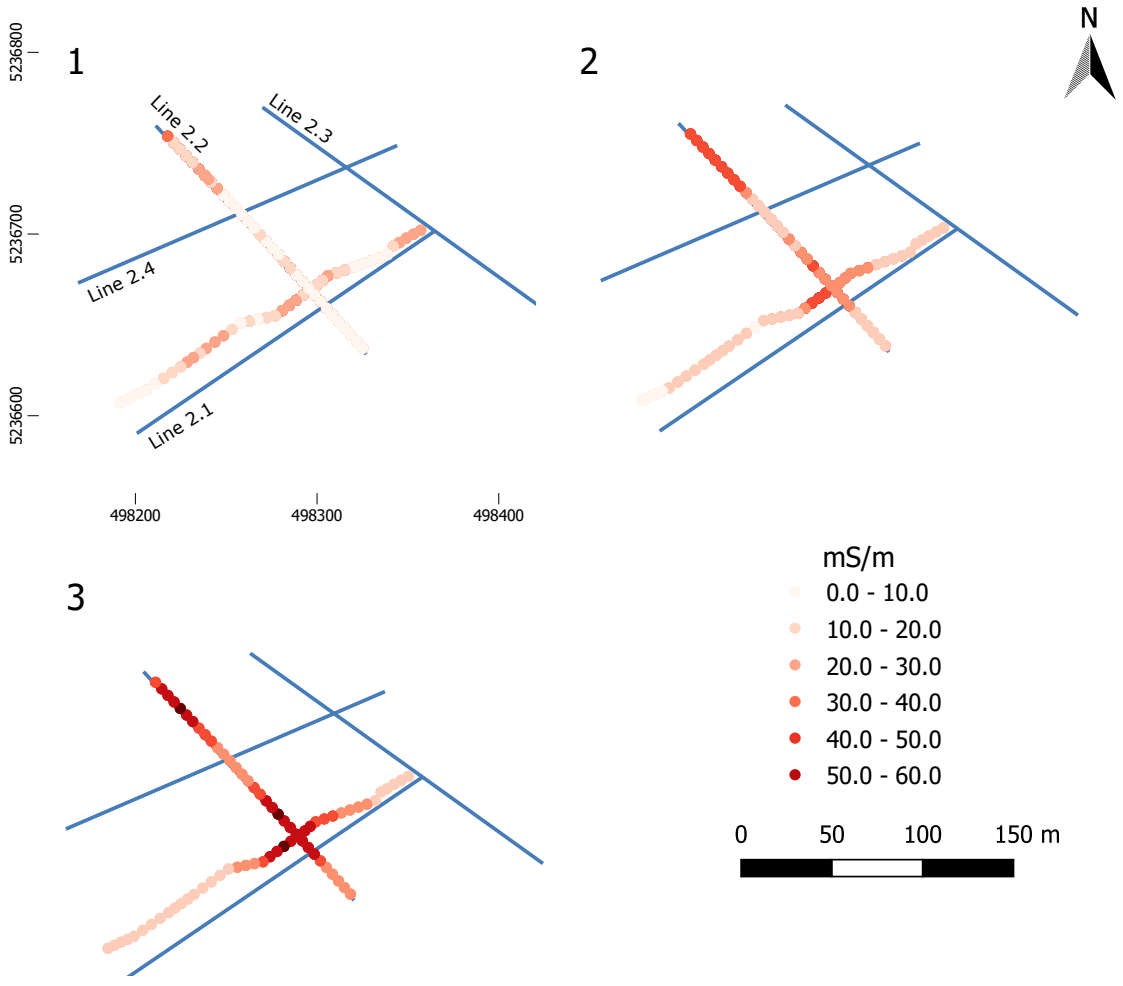

FIGURE 8.24: Conductivity values of Rablstollen area at different depths. (1) 0.75 m, (2) 3.0 m, (3) 6.0 m. Blue lines indicate ERT profile line locations.

8.3.2 Ederstollen

The conductivity map of Ederstollen area at a depth of 1.5 m is shown in figure 8.25. Additionally, ERT profile lines were added to the map for better positional

understanding. Conductivity values vary between 6 and 62 mS/m. Two well-distinguishable anomalies above 36 mS/m are detectable. The anomaly which is near the middle of the investigation area and crossed by profiles 1, 4, and 5 is in the same sector as ore body No. 11 (Figure 8.22) and as well as the low resistivity zone visible in ERT profiles 3.1 and 3.5 (Figures 8.7, 8.11). Magnetic data indicates that ore body No. 11 is embedded approximately 10 m deep, but in the ERT appears shallower at only 5 m. From the EM data, it can be concluded that already at 1.5 m some indications of the ore body are shown.

The second anomaly is more to the south, crossed by profile 3. This anomaly is partially visible in the ERT data (Figure 8.9) and also in the magnetic model as ore body No. 1 (Figure 8.22). Magnetic data shows that ore body No.1 is close to the surface, 1 or 2 m deep, but in the ERT data 5 m deep. However, the EM map shows, that at 1.5 m depth an ore body occurs.

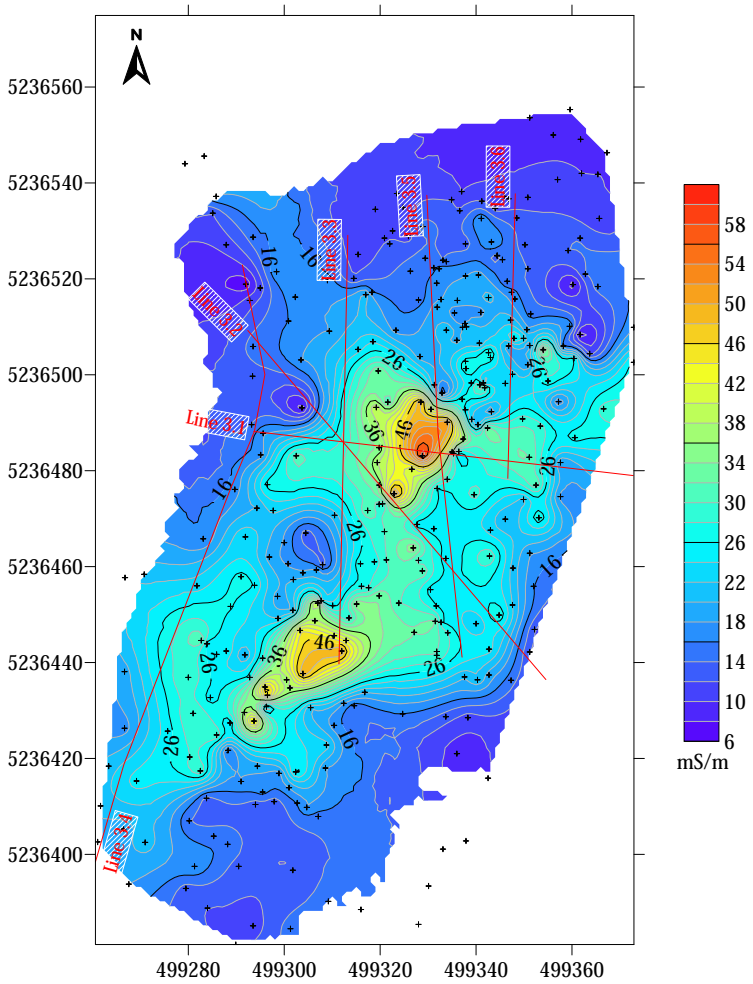

FIGURE 8.25: Conductivity map of Ederstollen area at depth of 1.5 m. Red lines indicate ERT profile line locations.

8.4 Self – Potential

8.4.1 Rablstollen

The self-potential map of Rablstollen is given in Figure 8.26. Additionally, ERT profile lines were added to the map for better positional understanding. Overall, the map looks uniform without significant self-potential variations. The south and the southwest part of the map consist mostly of negative values between -2 to -20 mV, but the north part and the northeast section for the most part are made up of positive SP values starting from 0 mV.

The negative anomaly zone between and next to lines 2.4 and 2.1 could indicate ore bodies' existence in the subsurface whose approximate location also agrees with magnetic data results. Ore bodies No. 23, 9, 1 and 3 from the 3-D magnetic model can be visible in the SP map as values below zero mV. Despite some comparability between applied geophysical methods, a large part of the ore bodies detected by other methods is not visible in the SP data.

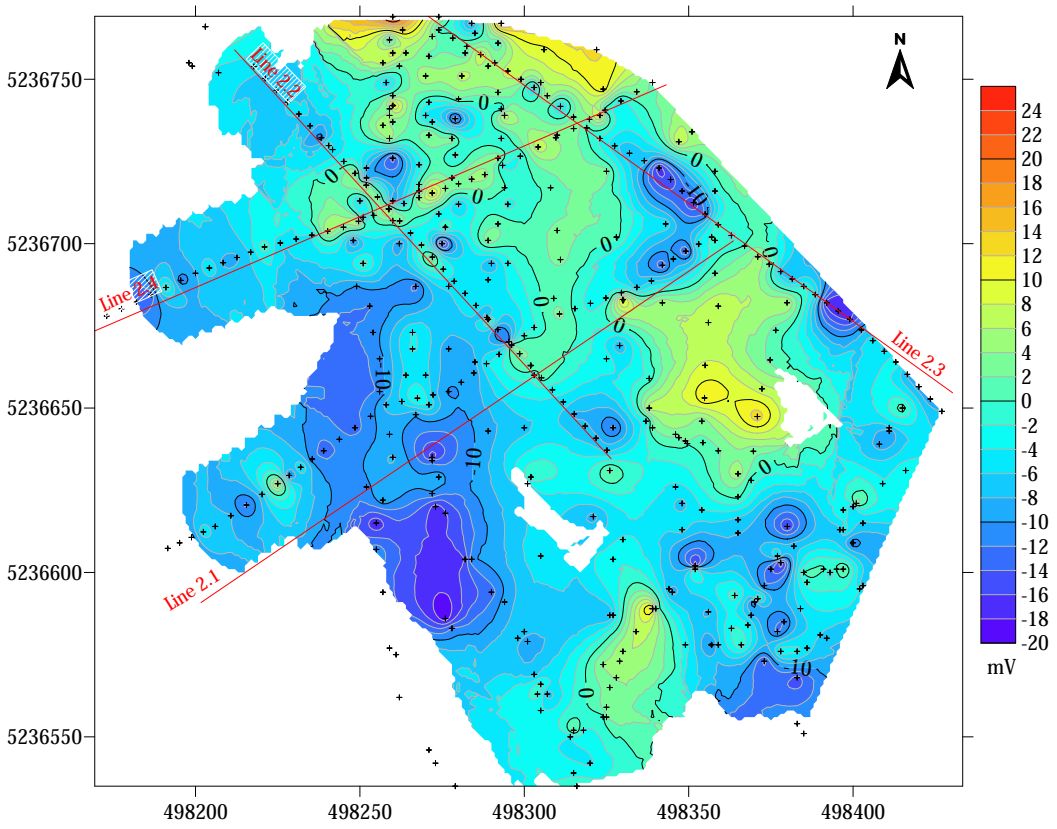

FIGURE 8.26: Self-potential map of Rablstollen area. Red lines indicate ERT profile line location.

9 DISCUSSION

Research presented in this thesis provides a preliminary investigation into the ability of resistivity, magnetism, self-potential, and electromagnetic methods for the detection of laterite ore bodies within sedimentary rocks. For those survey parameters employed during acquisition, all employed methods proved more or less effective in the detection of laterite ore at various depths, as well as in lithological border delineation.

9.1 Comparison between applied geophysical methods

For better analyzing of the capability of each method and comparing methods' strengths and weaknesses in the given environment, one representative profile from Rablstollen was selected where the geological section ideally shows laterite, sedimentary rocks, and bedrock, judging from the nearby located borehole.

Line 2.1 (in the magnetic data set line 8 ERT)(Fig. 9.1) visibly shows at least one laterite ore body embedded between sedimentary rocks, which yield non-magnetic properties and higher resistivity than laterite. The bedrock on the other hand has the highest resistivity and magnetic susceptibility of all occurring rock types. Electrical conductivity values are directly tied to the resistivity of the rock. In this case, negative SP values could indicate a potential ore body.

By comparing all four methods' performed on the same profile, one can interpret that ERT provides the most informative information about the subsurface in regard to the geology and geometry of the layers. ERT methods results can be used as a base for building up and supplementing the data with further information and interpretation from other applied geophysical methods. Magnetic data in this case shows the anomaly of the laterite body edges and specifies laterite dimensions more accurately than ERT data. Notably, the NE side of the magnetic profile should be longer to fully imagine the left side border of the ore body.

EM methods for all four measurement modes at depths of 0.75, 1.5, 3.0, and 6.0 m are represented in the plot. The strongest response from the laterite body is from EM31 instrument at 3 and 6 m depth. In the area where magnetic and ERT data indicate ore body EM methods conductivity values are the highest and with vertical dipole mode goes till 55 mS/m. By applying EM38 instrument with depths of 0.75 and 1.5 m data is more contaminated by noise and response from the ore body is harder to identify. However, vertical dipole mode measured conductivity values above laterite body are slightly higher than in the rest of the profile. At depth of 0.75, no clear laterite body response is visible in the acquired data.

Self-potential data scatter plot for the profile line appears noisy, but some slight indications of the ore body are visible where SP values are negative, closer to the SW profile side. This negative anomaly is a bit shifted to the right side compared to other applied methods' response to the laterite ore body, but that could be due to locations some degree difference, more to the southwest.

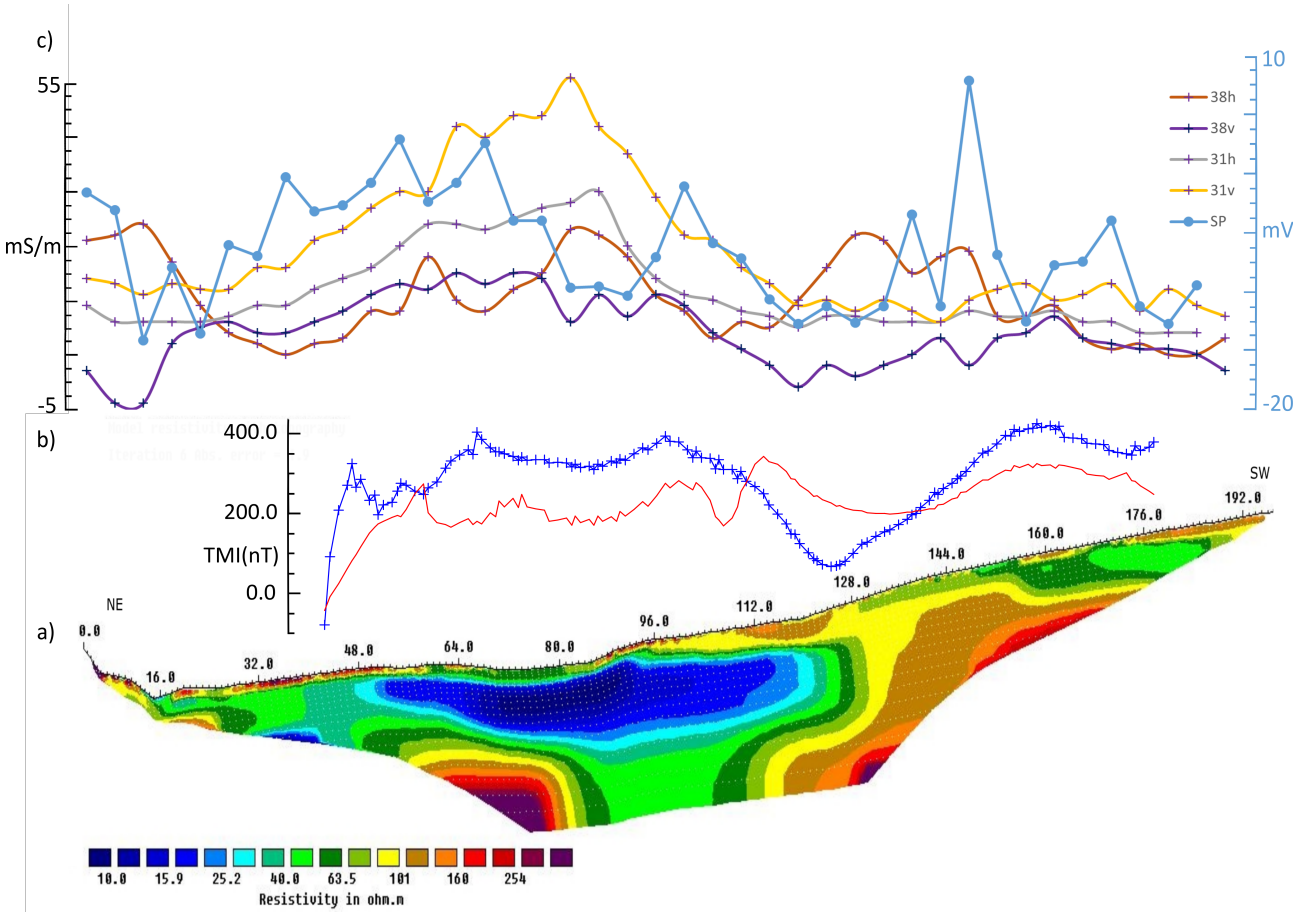

FIGURE 9.1: Rablstollen investigation areas representative profile lines (a) ERT, (b) magnetics and (c) EM and SP results.

9.2 Remarks on the data acquisition

The ERT method showed reasonably good acquired data with an overall small measurement error and noise level, except for the Manghuben profile where the instrument complications cause further problems within the acquired data set. Applied electrode arrays – mostly Wenner alpha array and in a few cases a dipole-dipole array – showed satisfactory results, but for the determination of the most efficient array for this environment an experiment with different electrode configurations of the same profile should be conducted. However, for the thesis proposes, Wenner alpha and dipole-dipole arrays provided the needed subsurface resolution.

Magnetic data sets from all locations provided acceptable data for processing and visualisation. For locations where 3-D modeling was performed – Rablstollen and

Ederstollen – a denser and more even grid would reduce the error margin and the non-uniqueness problem, but for the preliminary investigations, the fieldwork set-up and data grid were sufficient enough. In some cases, it would be more beneficial if, prior to the ERT or magnetic acquisition, geophysical data sets acquired previously would be studied and areas of interest would be marked for further fieldwork planning. Subsequently, problems, for example, not enough data coverage in some parts of the investigation area or profile length, should not arise. Difficult terrains and weather conditions also influenced field work extent and data coverage.

The electromagnetic and self-potential methods should be planned in the same locations as the ERT or magnetic methods, as mostly in this environment both methods were more supplementary than primarily for laterite identification.

9.3 Remarks on the data processing and representation

For all applied geophysical methods standard data processing was applied. For the ERT data a few different inversion methods were tested. In the author's opinion, the best one with the most promising results was picked, in this case, Robust inversion (or $L1$ - norm). Other parameters were selected to minimize absolute error and the number of iterations to avoid fitting noise. The ERT inverted resistivity sections represent reasonable results from the geological point of view, and they correlated quite well with other applied methods' results. Parameters, such as ore body's locations, dimensions, and border delineation, for the most part, match.

In the making of a 3-D magnetic model, ERT acquired and interpreted data was considered and used as a base from which further model constructions followed. The typical range of the reduced anomaly of the total magnetic intensity for laterite and serpentinite was acquired where the ERT data also covers the investigation area. According to those values, interpretation was made in areas where solely magnetic data exists.

Laterite ore bodies' magnetic anomalies were easily distinguishable in the magnetic data due to their clear characteristics and consistent features throughout the data sets. The straightforward geological environment also eased the interpretation process. Overall, magnetic method proved to be effective in the given environment.

For future research, it would be promising to combine different geophysical methods' results via a joint inversion approach to limit over-analysis and misinterpretation of the data.

9.4 Induced polarization (IP) methods applicability

During the field works together with ERT data also IP data were parallelly acquired for Rablstollen and Ederstollen profiles. Unfortunately, IP method with chosen parameter proved to be unsuccessful. As an example in Figure 9.2 the observed, calculated IP pseudosection of Rablstollen profile line 2.1. together with an inverted section is given. The observed IP data seems to be scattered and randomly distributed, without providing any understandable, concrete lithological information.

The IP effect can only be accurately measured at lower frequencies, but due to time constraints, it was not possible. Applied 4.16 Hz frequency, in this case, was too high to acquire reasonable results.

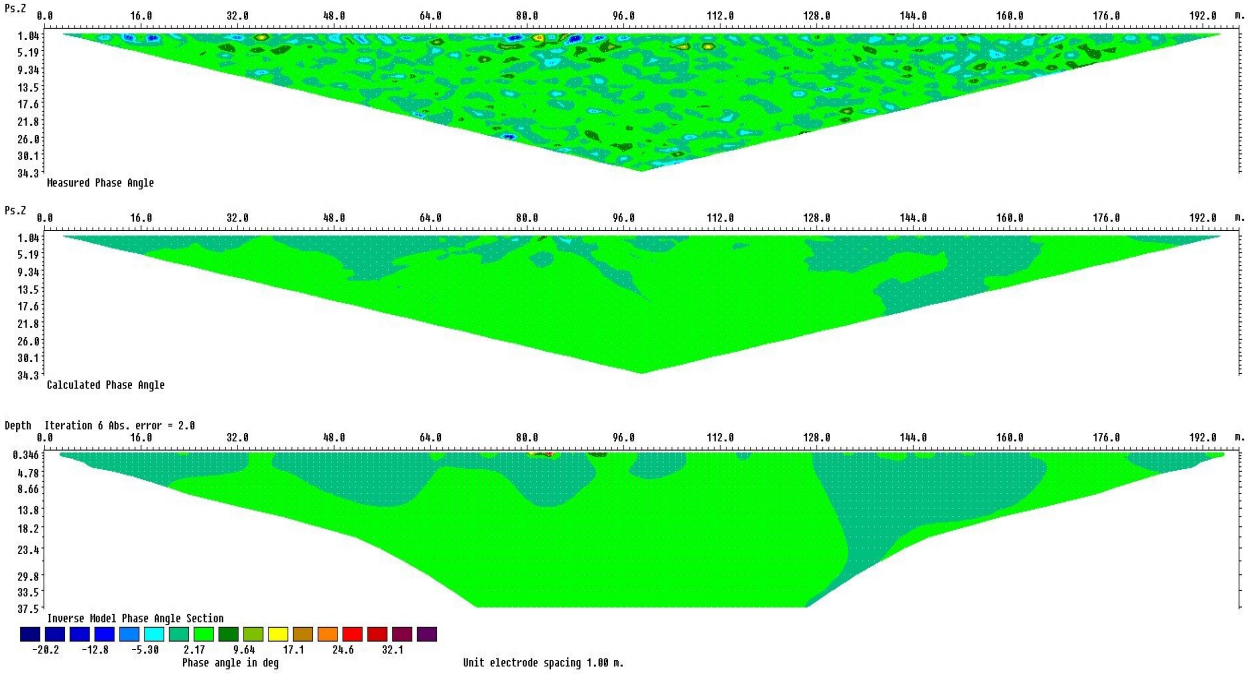

FIGURE 9.2: The observed, calculated IP pseudosection of Rablstollen profile line 2.1. together with inverted section.

9.5 Other geophysical methods alternatives

Due to its high resolution and ease of acquisition, GPR appears to be one geophysical technique with the potential to delineate the targets of interest in laterite deposits cost-effectively (Francke and Parkinson, 2000). GPR applicability in the lateritic environment was studied by Francke and Parkinson, 2000 and the main conclusion derived was that GPR is highly effective in imaging the complex subsurface structures of humid nickel and other laterite deposits. Although borehole grids remain necessary for data correlation, a wider borehole spacing based on geophysical information results in dramatic cost savings.

There are some cases where reflection and refraction seismic methods were applied in the lateritic environment for providing more detailed and accurate field predictions of weathering profiles. A variation of seismic reflection profiling, spectral analysis of surface waves (SASW) may be of use in lateritic weathering profiles due to the homogeneity of the upper layers. There are advantages to using shear wave refraction profiling in lateritic environments. Since the water table arrival is not significant, the absence of this arrival allows discrimination of other more subtle interfaces (Francke and Parkinson, 2000).

10 CONCLUSIONS

Using the analysis and results presented in the previous sections, the feasibility of the resistivity, magnetics, electromagnetics and self-potential methods for the detection of laterite ore bodies between layers of Neogene clastic sediments, from the Kraubath massif, can be assessed. Similarly, the magnetic method was also applied to the surrounding bedrock in the study area to obtain information about the possibility of lithological boundary identification and define the typical range of physical parameters over different lithologies. The survey parameters employed during the acquisition proved effective in the detection of laterite ore bodies at various depths, as well as in the delineation of lithological boundaries.

At **Manghube**, the ERT and magnetics were applied for possible laterite ore bodies detection, embedded at the boundaries between sediment and underlying rocks, and for boundaries determination of Neogene sediment - sand and gravel. Due to instrument complications and high geometry factor, data quality was below the required for the ERT method, and therefore the consequent results and interpretation were limited. But the general idea of the subsurface geological structure ERT method was able to capture, despite instrument problems.

As for the magnetics, no expected boundaries between sedimentary rocks and bedrock were recorded and any indications of laterite ore bodies' magnetic data do not reflect. The two datasets suggest that the NW and SE borders are composed of a non-magnetic bedrock, and in the middle part of the profiles - sedimentary rocks are located, which fills a negative relief form, possibly, a fault zone.

At **Rablstollen** various geophysical methods were applied - ERT, magnetics, self - potential and electromagnetic method. The ERT method was able to detect two large laterite ore bodies and a few uncertain low resistivity zones where clear indications of laterite existence were not found. The magnetic method was efficient enough to provide information about those unclear zones and supplement resistivity methods results with more detailed ore bodies distributions, dimensions and better investigation area coverage.

Electromagnetic methods data at depth of 1.5 m covered a quite large area but with some interruptions. An overall large percentage of the acquired data is just above the noise level and larger conductivity anomaly zones are made of one to few data points which is not enough. Two profile lines at depths of 0.75, 3.0 and 6.0 m show indications of the laterite body which is consistent with the rest of the results of the applied methods.

Self-potential method data in some parts of the area was efficient enough to indicate possible ore bodies whose locations would agree with other geophysical methods

but in some locations where a clear ore body was visible in the ERT and magnetic data, no indication was shown in the SP data.

The EM and self-potential methods in the given environment only confirmed laterite ore existence and marked possible locations but more detailed information with applied processing flow is not possible to acquire.

Ederstollen investigation area much like Rablstollen had the same geological setting, where laterite ore bodies are embedded between sedimentary rocks and below, deeper embedded bedrock starts - serpentinite and dunite. Good contrast between different lithologies laid a good foundation for the potentially successful applicability of geophysical methods. The ERT, magnetics and electromagnetic methods were applied in this location.

The same as in Rablstollen each method complemented one another or confirmed already concluded information, making each observation more concrete. Based on magnetic data, low resistivity zones measured by ERT coincided with modeled laterite ore bodies. The EM methods given information is not as detailed as for the first two applied methods. Smaller ore bodies anomalies are not strong enough to be visible in EM data but the approximate distribution zone for larger ore bodies is possible to identify.

Some inconsistencies arise between applied methods, regarding the exact depth and dimensions of the ore bodies. From the magnetic and ERT data, the bodies' depths and dimensions could vary from a few tens of centimetres to a few meters. EM data, which were measured at 1.5 m depth, display two large anomalies corresponding to ore bodies (No. 11 and 1), also visible in the magnetic and ERT data. It was assumed that at 1.5 m depth some part of the laterite ore shows. Comparing both cases between all three methods, in one case magnetic method overestimated the depth of the ore body, but in the second case, the ERT method overestimates. It can be concluded that both ERT and magnetic methods can surpass each other regarding the accuracy of the ore bodies' depth, depending on the case, but clear dominance does not show any of the methods.

Regarding the borders and dimensions of the bodies, more direct data are acquired such as boreholes or trial pits to compare and constrain applied geophysical methods. Results between ERT and magnetics in some cases differ, e.g. exact depth determination. In one case one method can be more precise than the other and vice versa. From EM data more detailed information, besides the approximate location and depth of the ore bodies, is not possible to gain by applying the processing flow used in this thesis.

Tanzmeistergraben 1 and 2 are the only two locations where the main target was to test the applicability of the magnetic method for different bedrock-type border delineations. As the reference point, a geological map of the area was used. Tanzmeistergraben 1 profiles crossed three different geological units and each of the borders are well visible in the magnetic data in a form of short and long wavelength dipoles. The reduced anomaly of the total magnetic intensity varies between -200 to 100 nT and is quite steady except at the border zones where dipole maximum can go till

1000 nT and minimum -1570 nT. Tanzmeistergraben 2 profiles crossed five different geological units and similarly to Tanzmeistergraben 1 each lithological border is well visible.

In summary, the electromagnetic method could be used for first-stage exploration works to delineate possible areas of interest due to the overall easy processing flow and capability of detection of larger-size laterite ores. To gain a more detailed understanding of subsurface geology and geometry, ERT and magnetic methods should be employed.

The self-potential method in this environment showed little promise of the consistent capability to detect laterite ore bodies to needed resolution. Further methods application to a given environment is not efficient enough and methods given results can be fully replaced by other geophysical methods which provide wider and more detailed information about the subsurface.

More work is required following this research, and future recommendations for each method are summarized below to make the work more efficient:

Electrical resistivity tomography:

- While a Wenner alpha and dipole-dipole configurations provided high-quality data, different survey geometries should be applied during data acquisition for comparing obtained results and bringing out each configuration's strengths and advantages.
- For more detailed subsurface mapping, three-dimensional imaging should also be explored for resistivity data in modeling and acquisition workflows.
- Several boreholes along the spread array should be acquired to obtain higher confidence in determining lithologies based on resistivities.

Magnetics:

- More magnetic susceptibility and, possibly, remanent magnetisation measurements made on different lithologies for better constraining magnetic data for 3-D modeling.
- For more precise border delineation between different lithologies in Manghube, Tanzmeistergraben 1 and 2, the profile lines' length should be longer to fully record long wavelength anomalies.

Electromagnetics:

- Acquire a denser and wider grid at depths of 3.0 and 6.0 meters for better comparison with other geophysical methods' results.

Self-potential:

- A denser grid for the SP method could help to increase the signal to noise ratio of the data set.

Bibliography

Amosun, J. et al. (2020). Imaging lateritic bauxite bearing zones in Ekiti, Southwestern Nigeria, using magnetic and electrical resistivity tomography techniques. In: *SN Applied Sciences* 2. DOI: 10.1007/s42452-020-03785-w.

Arekumo, T. and O. O. Lawrence (2019). Evaluation of Lateritic Soil from Field Resistivity Data at Okada, South-South, Nigeria. In: *International Journal of Science and Research (IJSR)* 8. DOI: 10.21275/ART20198933.

Arkoprovo, B. (2017). A review on modeling, inversion and interpretation of self-potential in mineral exploration and tracing paleo-shear zones. In: *Ore Geology Reviews* 91, pp. 21–56. DOI: https://doi.org/10.1016/j.oregeorev.2017.10.024.

Becker, L. P. (1981). Zur Gliederung des Obersteirischen Altkristallins (Muriden). Mit Bemerkungen zu den Erzvorkommen in den einzelnen Kristallinkomplexen. In: *Verh. Geol.B.-A.*, pp. 3–17.

Central Institution for Meteorology and Geodynamics (n.d.). https://www.zamg.ac.at/cms/de/aktuell. Accessed: 2022-07-30.

Day-Lewis, F. D. et al. (2007). Best practices in electrical resistivity imaging: data collection and processing, and application to data from Corinna, Maine. In: *An Administrative Report for EPA Region 1*, pp. 20–21. URL: https://clu-in.org/programs/21m2/projects/EPA_admin_report_02Dec2008_final.pdf.

Dentith, M. and S. T. Mudge (2014). *Geophysics for the Mineral Exploration Geoscientist*. Cambridge University Press. DOI: 10.1017/CBO9781139024358.

Dey, A. and H. F. Morrison (1979). Resistivity modelling for arbitrarily shaped two-dimensional structures. In: *Geophysical Prospecting* 27.1, pp. 106–136. DOI: https://doi.org/10.1111/j.1365-2478.1979.tb00961.x.

Everett, M.E. (2013). In: *Near-Surface Applied Geophysics*. Cambridge University Press, p. 400.

Francke, J. and G. Parkinson (2000). The new role of geophysics in nickel laterite exploitation and development. In: *Mining Millennium/PDAC 2000 Conference Proceedings, Toronto*.

Frank, W. (1987). Evolution of the Austroalpine elements in the Cretaceous. In: *Geodynamics of the Eastern Alps. Vienna: Franz Deuticke*. Ed. by H. W. Flügel and P. Faupl, pp. 379–406.

Frisch, W. and F. Neubauer (1989). Pre-Alpine terrane and tectonic zoning in the eastern Alps. In: *Geol. Soc. Amer. Spec. Pap.* 230, pp. 91–100.

Kerr, T. L. et al. (1994). Geophysics and Iron Ore Exploration: Examples from the Jimblebar and Shay Gap-Yarrie Regions, Western Australia. In: *Exploration Geophysics* 25.3, pp. 169–170. DOI: 10.1071/EG994169b.

Loke, M. H. (2001). *Tutorial: 2-D and 3-D Electrical Imaging Surveys*.

Loke, M. H. and R.D. Barker (1996). Rapid Least-Squares Inversion of Apparent Resistivity Pseudosections Using a Quasi-Newton Method. In: *Geophysical Prospecting* 44, pp. 131 –152. DOI: 10.1111/j.1365-2478.1996.tb00142.x.

Magnetic data observatory plots (n.d.). https://www.intermagnet.org/data-donnee/dataplot-eng.php?type=xyz. Accessed: 2022-07-09.

Matz, K. B. (1940). Die Toneisensteinlagerstätte am Lichtensteinerberg bei St. Stefan - Kraubath. In: *Berg- und Hüttenm. Mh.* 88, pp. 103–106.

Maxwell, J. C. (1865). A Dynamical Theory of the Electromagnetic Field. In: *Philosophical Transactions of the Royal Society of London* 155, pp. 459–512.

Melcher, F. and T. Meisel (2004). A Metamorphosed Early Cambrian Crust–Mantle Transition in the Eastern Alps, Austria. In: *Journal of Petrology* 45.8, pp. 1689–1723. DOI: 10.1093/petrology/egh030.

Moon, C., M. K. G. Whateley, and A. M. Evans (2006). *Introduction to Mineral Exploration (2nd Edition)*. ISBN: 1-4051-1317-0.

Neubauer, F. (1988). Bau und Entwicklungsgeschichte des Rennfeld-Mugel- und des Gleinalm-Kristallins (Ostalpen). In: *Abhandlungen der Geologischen Bundesanstalt* 42, pp. 1–137. URL: https://www.zobodat.at/pdf/AbhGeolBA_42_0001-0137.pdf.

Neyamadpour, A. et al. (2010). Comparison of Wenner and dipole–dipole arrays in the study of an underground three-dimensional cavity. In: *Journal of Geophysics and Engineering* 7.1, pp. 30–40. DOI: 10.1088/1742-2132/7/1/003.

Oldenburg, D.W. and Y. Li (2005). Inversion for Applied Geophysics: A Tutorial. In: *Near-Surface Geophysics*. Ed. by D.K. Butler. Society of Exploration Geophysicists. Chap. 5, pp. 89–148. DOI: 10.1190/1.9781560801719.ch3.

Othniel, K. L. (2014). Exploring and Using the Magnetic Methods. In: *Advanced Geoscience Remote Sensing*. Ed. by M. Marghany. Rijeka: IntechOpen. Chap. 7. DOI: 0.5772/57163.

Palka, R. et al. (2009). The forward and inverse problems in magnetic induction tomography of low conductivity structures. In: *Engineering Computations* 26, pp. 843–856. DOI: 10.1108/02644400910985206.

Petric, M. (1981). Exploration of Burundi Nickeliferous laterites by electrical methods. In: *Geophysical Prospecting* 29.2, pp. 274–287. DOI: https://doi.org/10.1111/j.1365-2478.1981.tb00405.x.

Revil, A. and A. Jardani (2013). *The Self-Potential Method: Theory and Applications in Environmental Geosciences*. Cambridge University Press. DOI: 10.1017/CBO9781139094252.

Ruiqing, D. and Y. Jin (2012). Application of ordinary Kriging method in data processing of magnetic survey. In: *2012 7th International Conference on Computer Science & Education (ICCSE)*, pp. 771–774. DOI: 10.1109/ICCSE.2012.6295186.

Schaa, R. and P. Fullagar (2010). Rapid, approximate 3D inversion of transient electromagnetic (TEM) data. In: *SEG Technical Program Expanded Abstracts*, pp. 650–654. DOI: 10.1190/1.3513866.

Shao, P. et al. (2021). Integration of ERT, IP and SP Methods in Hard Rock Engineering. In: *Applied Sciences* 11, p. 10752. DOI: 10.3390/app112210752.

Sharma, P. V. (1997). *Environmental and Engineering Geophysics*. Cambridge University Press. DOI: 10.1017/CBO9781139171168.

Silvester, P. P. and R. L. Ferrari (1996). *Finite Elements for Electrical Engineers*. 3rd ed. Cambridge University Press. DOI: 10.1017/CBO9781139170611.

Snieder, Roel K and Jeannot Trampert (n.d.). Inverse problems in Geophysics Roel Snieder and Jeannot Trampert. In: URL: https://api.semanticscholar.org/CorpusID:17276678.

Sowards, K. et al. (2018). A conceptual model for the rapid weathering of tropical ocean islands: A synthesis of geochemistry and geophysics, Kohala Peninsula, Hawaii, USA. In: *Geosphere* 14. DOI: 10.1130/GES01642.1.

Söhle, U. (1901). Geologischer Bericht über das Eisenstein-Vorkommen am Lichtensteinerberg bei Kraubath in Obersteiermark. In: *Carinthia II* 91, pp. 159–162. URL: https://www.zobodat.at/pdf/CAR_91_0159-0162.pdf.

Telford, W. M., L. P. Geldart, and R. E. Sheriff (1990). *Applied Geophysics*. 2nd ed. Cambridge University Press. DOI: 10.1017/CBO9781139167932.

Thalhammer, O. A. R. and M. Heinrich (2015). The Kraubath ultramafic massif excursion guide. In: *ÖMG conference Leoben 2015, Austria*. URL: https://www.uibk.ac.at/mineralogie/oemg/bd_161/bd_162_min_pet_exk.pdf.

Vauhkonen, M., T. Tarvainen, and T. Lahivaara (2016). Inverse Problems. In: *Mathematical Modelling*. Ed. by S. Pohjolainen. Cham: Springer International Publishing, pp. 207–227. DOI: 10.1007/978-3-319-27836-0_12.

Ye, Nan, Farbod Roosta-Khorasani, and Tiangang Cui (2019). Optimization Methods for Inverse Problems. In: *2017 MATRIX Annals*. Ed. by Jan de Gier, Cheryl E. Praeger, and Terence Tao. Cham: Springer International Publishing, pp. 121–140. DOI: 10.1007/978-3-030-04161-8_9.

Yuval, D. and W. Oldenburg (1996). DC resistivity and IP methods in acid mine drainage problems: results from the Copper Cliff mine tailings impoundments. In: *Journal of Applied Geophysics* 34.3, pp. 187–198. DOI: https://doi.org/10.1016/0926-9851(95)00020-8.

Zhao, J., Y. Xu, and F. Dong (2014). An L q –L p optimization framework for image reconstruction of electrical resistance tomography. In: *Measurement Science and Technology* 25. DOI: 10.1088/0957-0233/25/12/125402.

A The observed and calculated apparent resistivity pseudosections

FIGURE A.1: The observed and calculated apparent resistivity pseudosection of Manghube profile 1 together with the section obtained by inversion process using RES2DINV program.

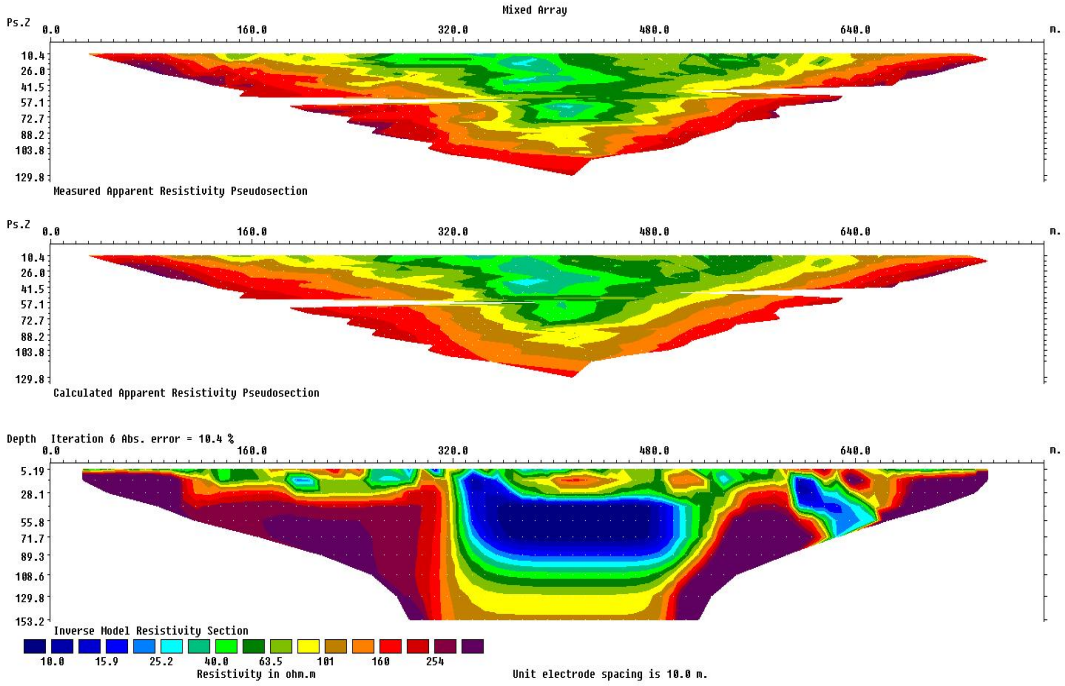

FIGURE A.2: The observed and calculated apparent resistivity pseudosection of Rablstollen profile 2.1 together with the section obtained by inversion process using RES2DINV program.

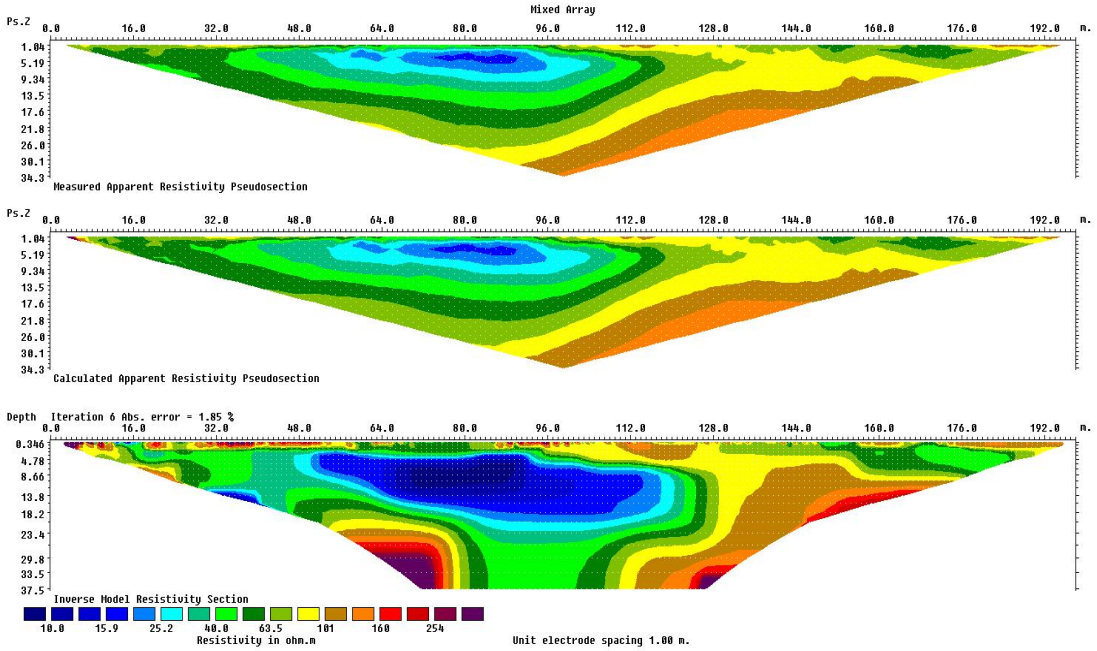

FIGURE A.3: The observed and calculated apparent resistivity pseudosection of Rablstollen profile 2.2 together with the section obtained by inversion process using RES2DINV program.

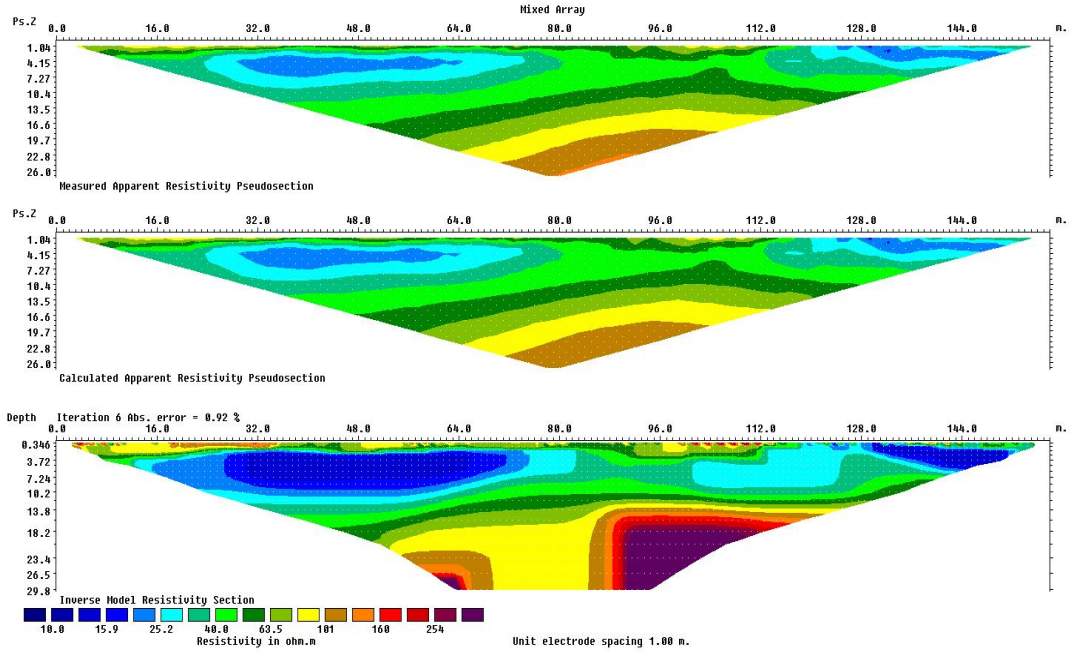

FIGURE A.4: The observed and calculated apparent resistivity pseudosection of Rablstollen profile 2.3 together with the section obtained by inversion process using RES2DINV program.

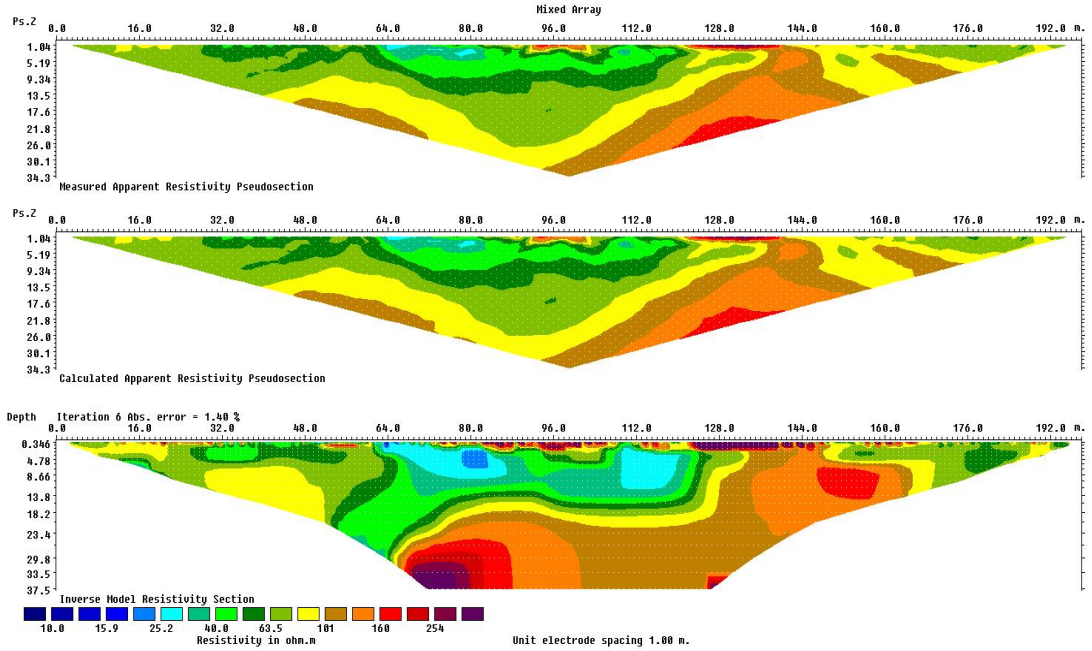

FIGURE A.5: The observed and calculated apparent resistivity pseudosection of Rablstollen profile 2.4 together with the section obtained by inversion process using RES2DINV program.

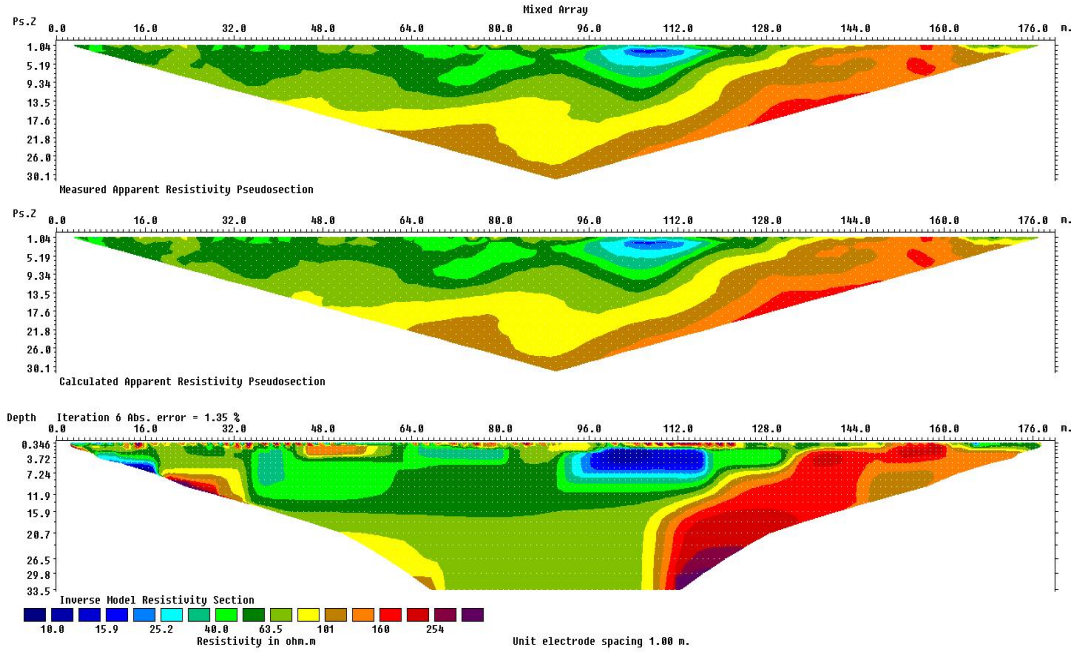

FIGURE A.6: The observed and calculated apparent resistivity pseudosection of Ederstollen profile 3.1 together with the section obtained by inversion process using RES2DINV program.

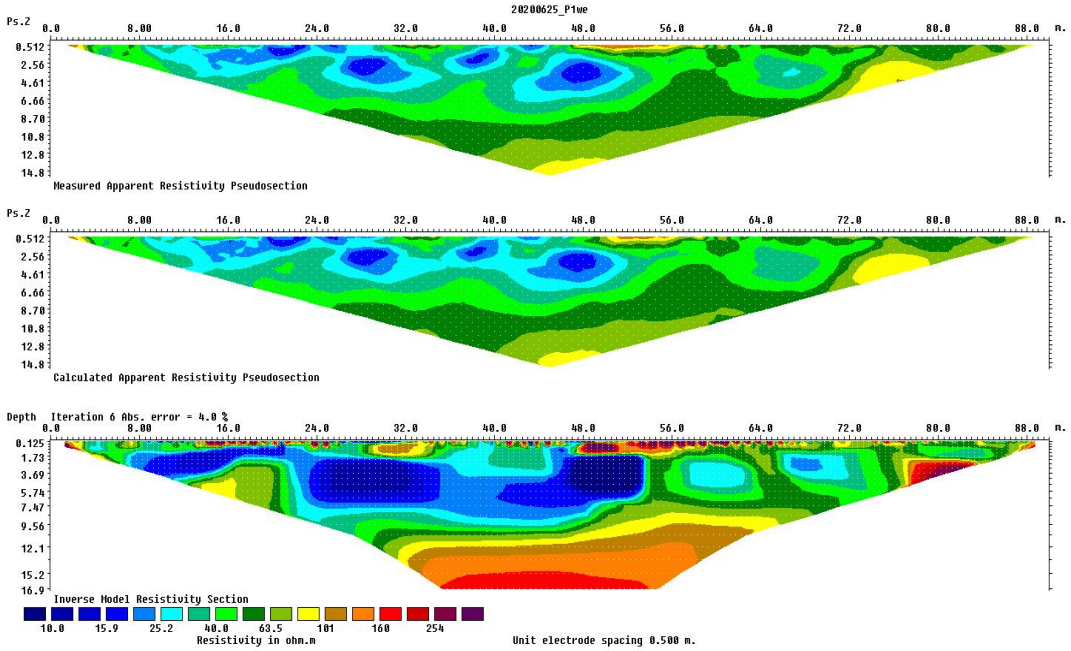

FIGURE A.7: The observed and calculated apparent resistivity pseudosection of Ederstollen profile 3.2 together with the section obtained by inversion process using RES2DINV program.

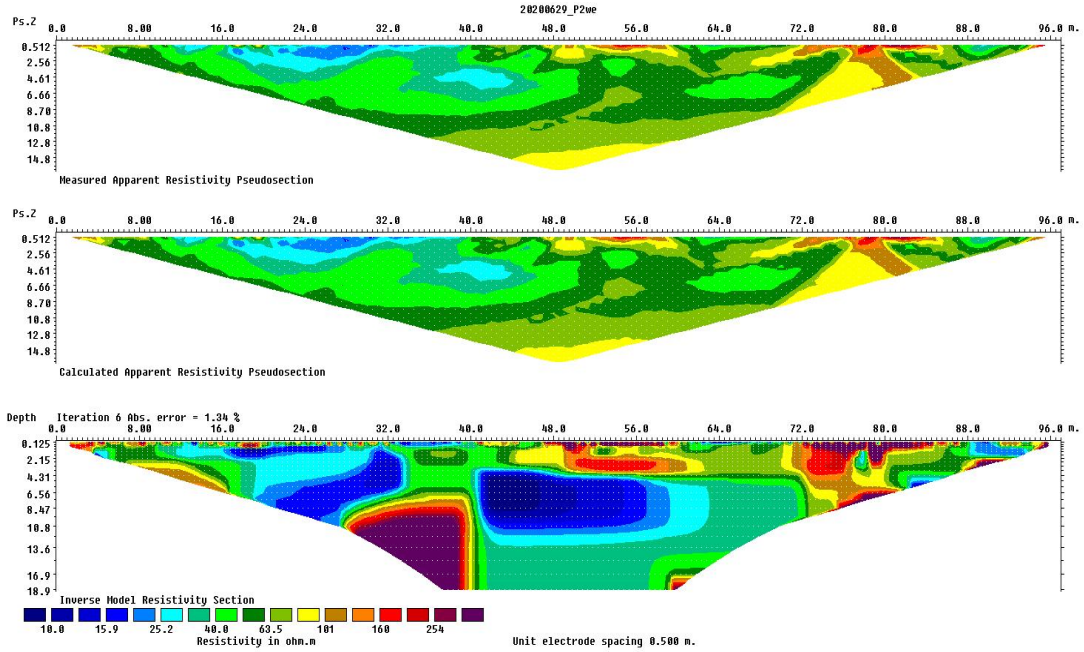

FIGURE A.8: The observed and calculated apparent resistivity pseudosection of Ederstollen profile 3.3 together with the section obtained by inversion process using RES2DINV program.

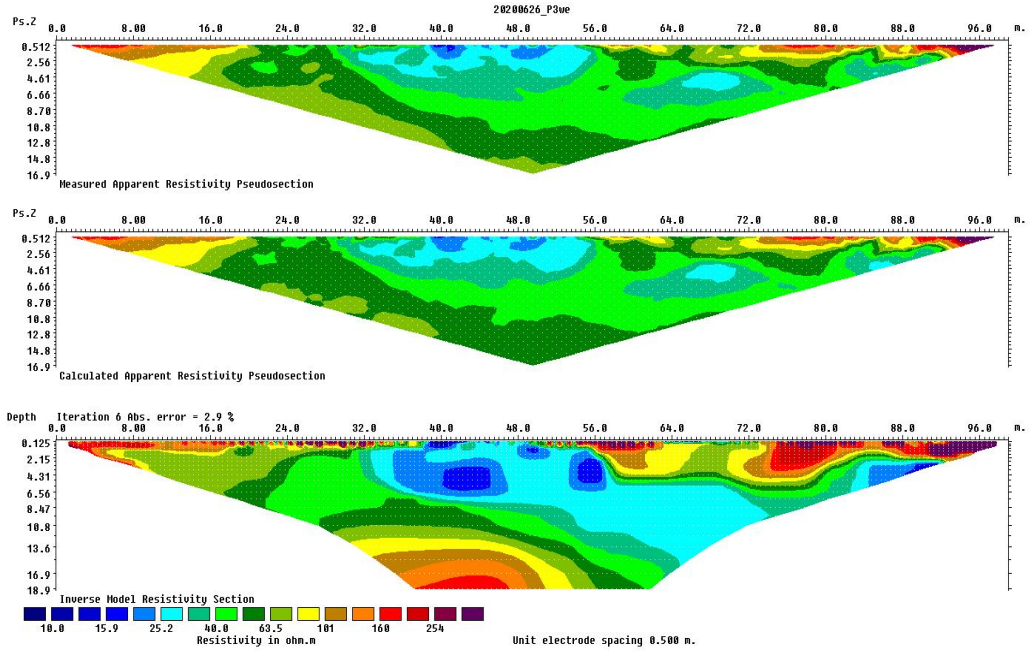

FIGURE A.9: The observed and calculated apparent resistivity pseudosection of Ederstollen profile 3.4 together with the section obtained by inversion process using RES2DINV program.

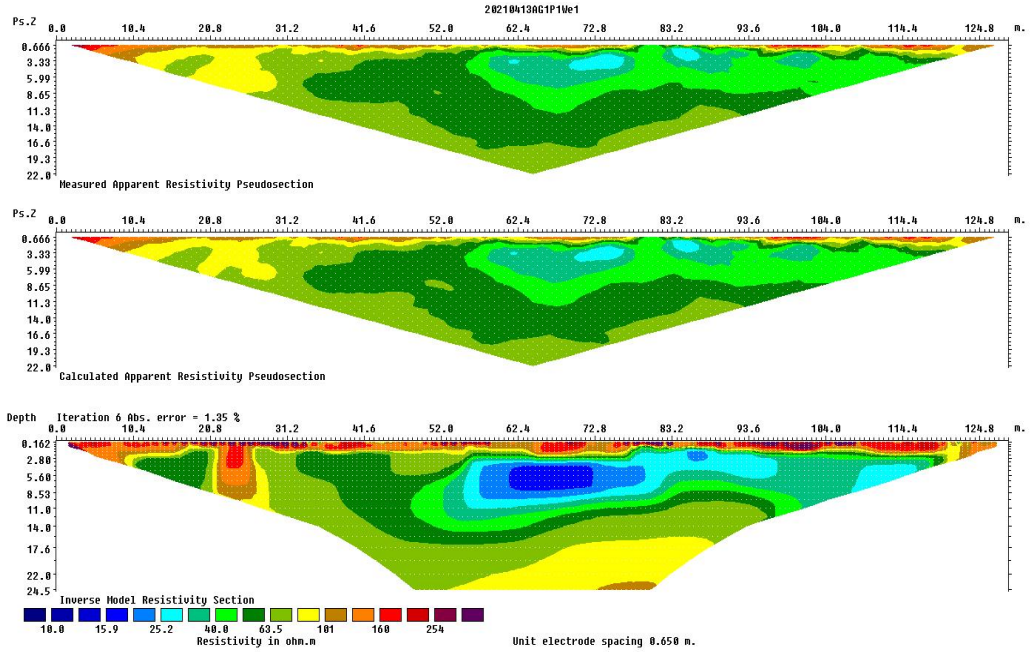

FIGURE A.10: The observed and calculated apparent resistivity pseudosection of Ederstollen profile 3.5 together with the section obtained by inversion process using RES2DINV program.

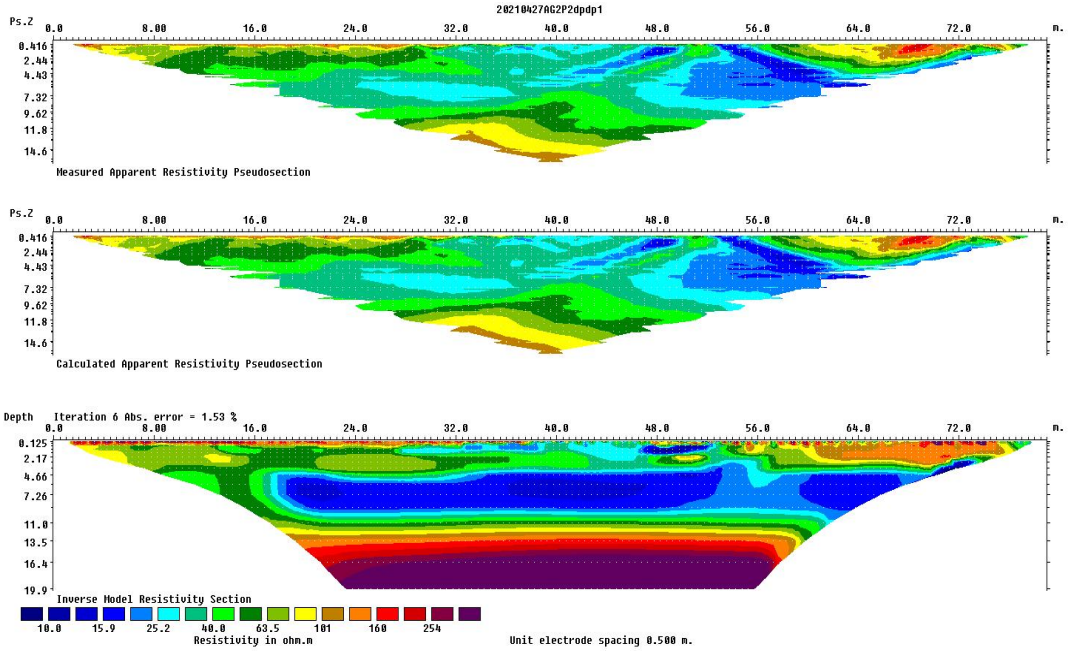

FIGURE A.11: The observed and calculated apparent resistivity pseudosection of Ederstollen profile 3.6 together with the section obtained by inversion process using RES2DINV program.

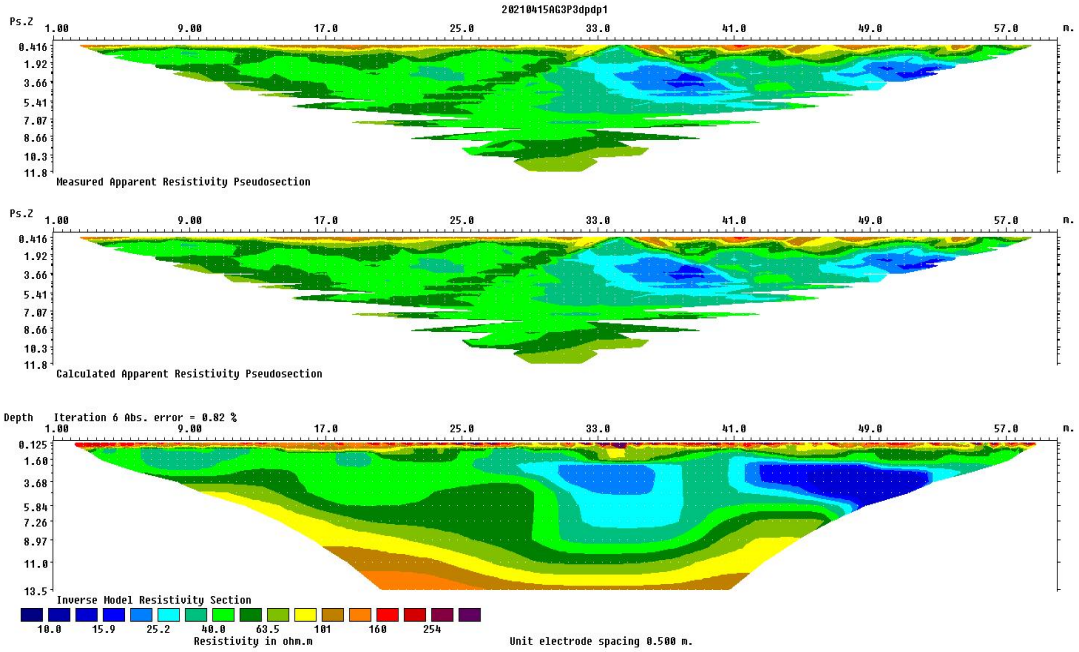

B Observed magnetic field (XYZ) plots from Conrad observatory

FIGURE B.1: Observed magnetic field (XYZ) plot on 15.03.2016 provided by Conrad observatory.

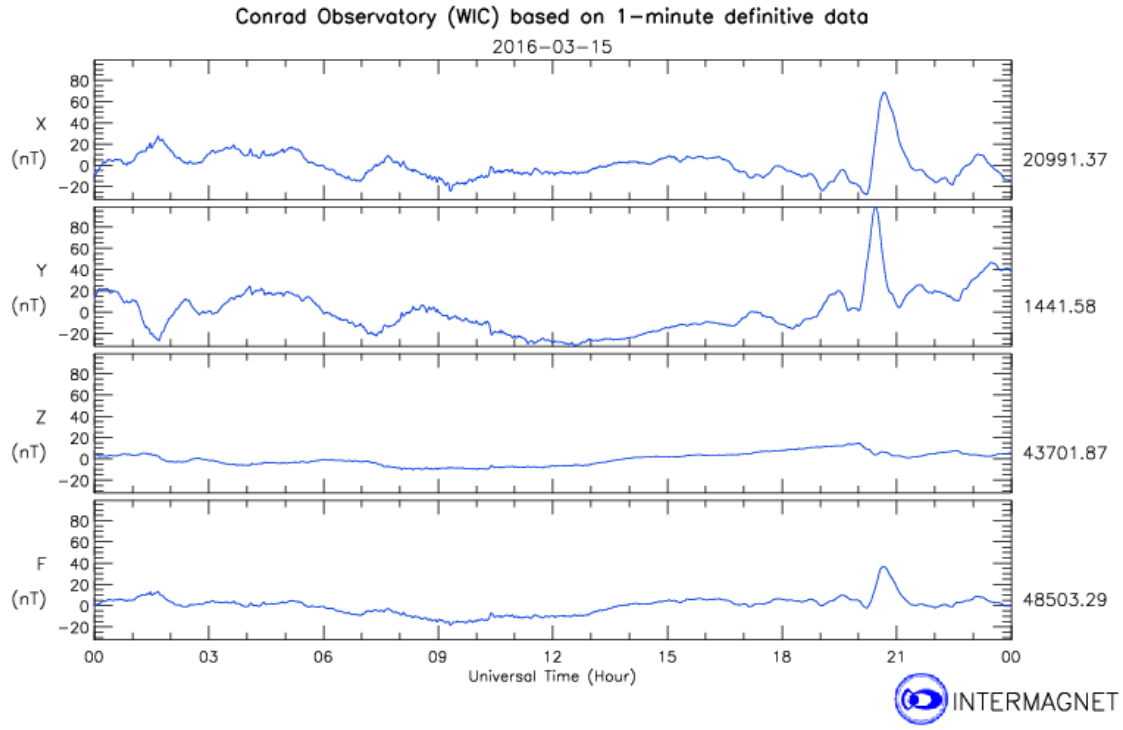

FIGURE B.2: Observed magnetic field (XYZ) plot on 24.03.2017 provided by Conrad observatory.

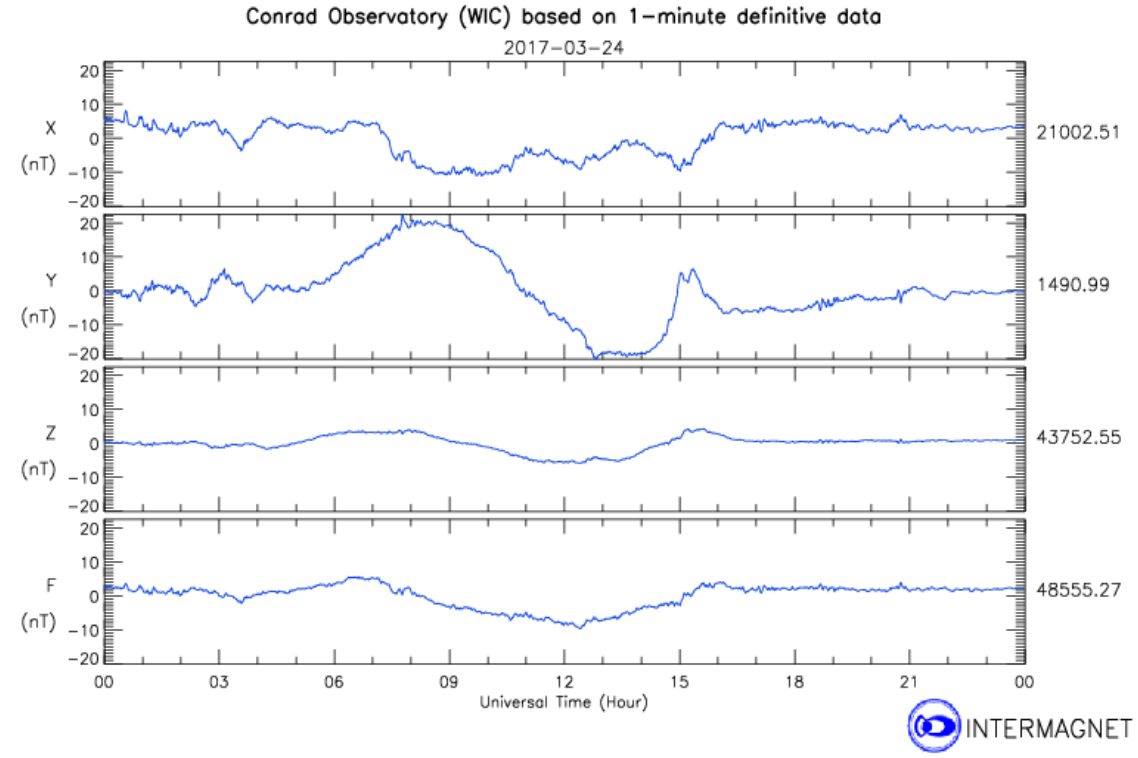

FIGURE B.3: Observed magnetic field (XYZ) plot on 04.03.2017 provided by Conrad observatory.

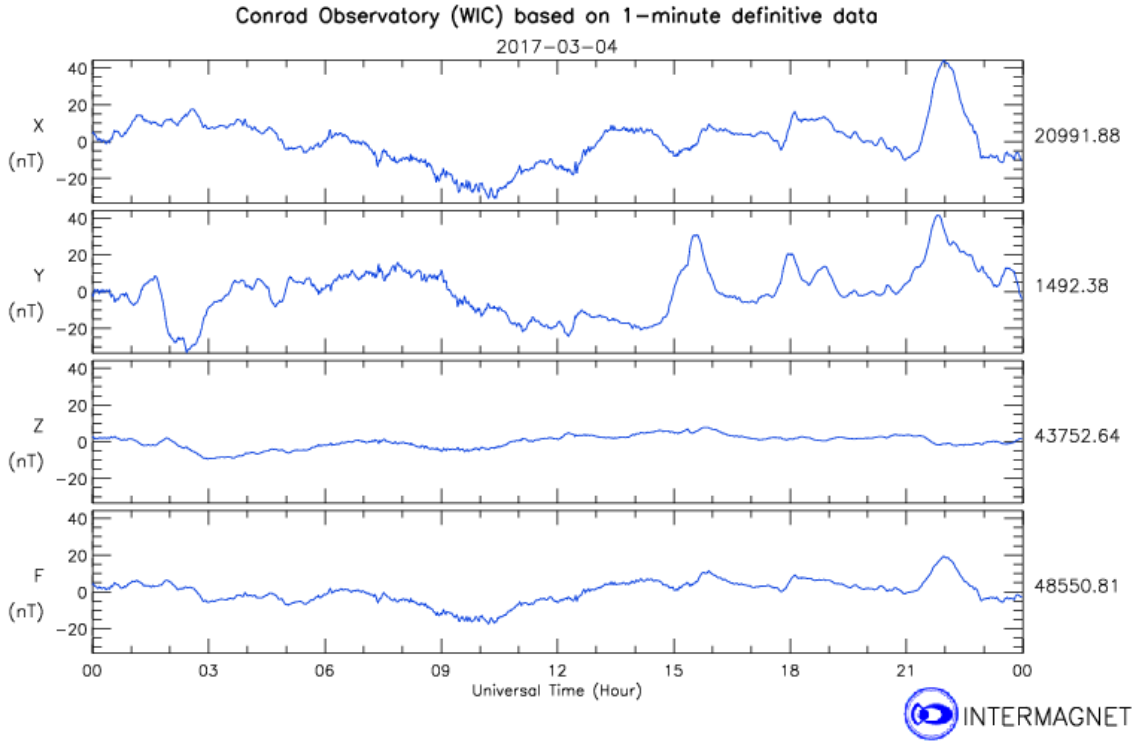

FIGURE B.4: Observed magnetic field (XYZ) plot on 15.04.2021 provided by Conrad observatory.

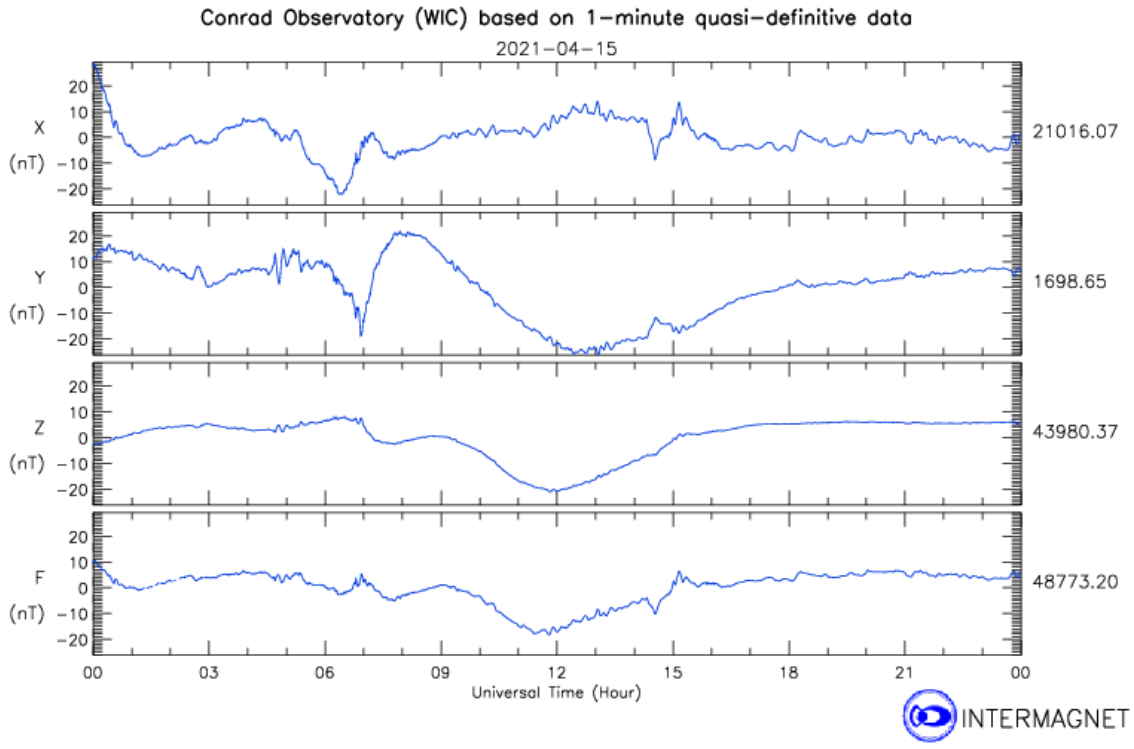

FIGURE B.5: Observed magnetic field (XYZ) plot on 27.04.2021 provided by Conrad observatory.